A Numerical Study of Flow and Heat Transfer in Compact Heat Exchangers

L. W. Zhang and S. Balachandar

ACRC TR-103 August 1996

For additional information:

Air Conditioning and Refrigeration Center
University of Illinois
Mechanical & Industrial Engineering Dept.
1206 West Green Street
Urbana, IL 61801

(217) 333-3115

Prepared as part of ACRC Project 38
An Experimental and Numerical Study of Flow and Heat Transfer in Louvered-Fin Heat Exchangers
S. Balachandar and A. M. Jacobi, Principal Investigators

The Air Conditioning and Refrigeration Center was founded in 1988 with a grant from the estate of Richard W. Kritzer, the founder of Peerless of America Inc. A State of Illinois Technology Challenge Grant helped build the laboratory facilities. The ACRC receives continuing support from the Richard W. Kritzer Endowment and the National Science Foundation. The following organizations have also become sponsors of the Center.

Amana Refrigeration, Inc.
Brazeway, Inc.
Carrier Corporation
Caterpillar, Inc.
Dayton Thermal Products
Delphi Harrison Thermal Systems
Eaton Corporation
Ford Motor Company
Frigidaire Company
General Electric Company
Lennox International, Inc.
Modine Manufacturing Co.
Peerless of America, Inc.
Redwood Microsystems, Inc.
U. S. Army CERL
U. S. Environmental Protection Agency
Whirlpool Corporation

For additional information:

Air Conditioning & Refrigeration Center
Mechanical & Industrial Engineering Dept.
University of Illinois
1206 West Green Street
Urbana IL 61801

217 333 3115

ABSTRACT

An accurate computational method for the calculations of flow and heat transfer in compact heat exchangers is developed in collaboration with the National Center for Supercomputing Applications. In this method, the unsteady Navier-Stokes and energy equations are solved. In the simulations of flow and heat transfer over relatively simple heat exchanger fin geometries, a linearly scalable performance of the code is achieved on the massively parallel CM5, demonstrating the capability of this method to solve large scale heat transfer problems. Using this code, the heat transfer enhancement mechanisms and performance of parallel-plate fin heat exchangers are studied extensively. Geometry effects such as finite fin thickness and different fin arrangements (inline and staggered) have been investigated. The time-dependent flow behavior due to vortex shedding has been taken into consideration by solving the unsteady Navier-Stokes and energy equations. In the unsteady regime, in addition to the time-dependent calculations, companion steady symmetrized flow calculations have also been performed to clearly identify the effect of vortex shedding on heat transfer and frictional loss. Additional comparisons have been made to the theoretical results for fully developed flow between uninterrupted continuous parallel plates and those of restarted boundary layers with negligible fin thickness, in order to quantify the role of boundary layer restart mechanism as well as the geometry effects of finite fin thickness and fin arrangement.

It is shown in the current study that at higher Reynolds numbers, the additional effect introduced by intrinsic three-dimensionality of the flow also plays an important role in determining the overall heat exchanger performance. At sufficiently high Reynolds numbers, when the actual flow is three-dimensional, corresponding two-dimensional models overpredict overall heat transfer efficiency by as much as *25%*, while the overprediction of frictional loss is much less. More importantly, the overprediction of rms fluctuations in heat transfer and frictional loss in two-dimensional models is much larger, where the amplitude of fluctuations from two-dimensional models can be as much as *2* and *5* times of those from corresponding three-dimensional models for the heat transfer efficiency (Colburn j factor) and frictional loss (friction factor), respectively. These differences are attributed to

the strong coherence of spanwise vortices in two-dimensional simulations and the weakening of spanwise vortices in the corresponding three-dimensional simulations due to the presence of streamwise vortices. In two-dimensional simulations, the coherent spanwise vortices enhance mixing and result in higher heat transfer efficiency. These spanwise vortices at the same time lowers skin friction on the fin surface. On the other hand, it has been well established that two-dimensional simulations overpredict form drag due to higher Reynolds stresses in the wake. In current two-dimensional simulations of flow over parallel-plate fins, the overprediction of form drag is nearly counter-balanced by the underprediction of skin friction. Such mechanisms also shed light on enhancing heat transfer while avoiding the normally associated increased pumping power penalty.

In the simulations of flow and heat transfer in more complex louvered fin geometries, current numerical results clearly show the different flow regimes as the Reynolds number is increased, which are generally in agreement with those observed in experimental flow visualizations. However, at low Reynolds numbers, current interpretation of the flow characteristics is somewhat different. At higher Reynolds numbers, the effect of flow unsteadiness is to increase overall heat transfer and associated frictional loss.

TABLE OF CONTENTS

LIST OF TABLES

LIST OF FIGURES

NOMENCLATURE

A_m	minimum flow cross-section area
b	fin thickness
C	transverse adjacent fin spacing
C_D	drag coefficient
C_F	skin friction coefficient
C_f	local skin friction factor
D	computational domain
D_h	hydraulic diameter
$\boldsymbol{E}$	shear tensor
$\hat{e}_x$	unit vector in streamwise, x, direction
f	friction factor
F	primary shedding frequency
H	half channel height in inline arrangement
j	modified Colburn factor
k	thermal conductivity of the fluid
L	fin length
L_x	computational domain length in x–dir.
L_y	computational domain length in y–dir.
L_z	computational domain length in z–dir.
$\hat{\boldsymbol{n}}$	outward normal unit vector on fin surface
Nu	Nusselt number
$<Nu>$	global Nusselt number
ΔP	mean pressure difference
P	total pressure
p	modified perturbation pressure
s	length along the fin periphery
S	streamwise adjacent fin spacing
St	Strouhal number
t	time
T	total temperature
u,v,w	velocity in x-, y- and z- directions
u_τ	friction velocity
V	mean flow velocity at A_m

Greek Symbols

α	fluid thermal diffusivity
β	mean pressure gradient
γ	mean temperature gradient
λ	eigenvalue of velocity gradient tensor
θ	modified perturbation temperature
$\mathcal{P}$	perimeters of fins within a basic unit
μ	fluid viscosity
∇	gradient of
ν	fluid kinematic viscosity
Ω_f	fin surface area
∂	boundary surface

Superscript

*	dimensional quantities

Pr	Prandtl number	Subscripts	
Q	mean flow rate per unit spanwise width	f	based on fin
q''	constant dimensional heat flux	ref	based on reference
$\boldsymbol{R}$	rotation tensor	x,y,z	based on x, y, z Cartesian coordinates
Re	Reynolds number based on D_h	τ	based on friction velocity

CHAPTER 1. INTRODUCTION

1.1 Motivation

Increasing demand for compactness of heat exchangers in the automotive industry as well as many refrigeration and air-conditioning applications has driven heat exchanger design towards achieving increased surface density and smaller flow channels. Unfortunately, this miniaturization based on conventional heat transfer surface design has resulted in a tendency towards laminar flow and subsequently lower air-side heat transfer coefficients. During the past several decades, various innovative interrupted surfaces have been used to augment heat transfer in the above applications. The simplest geometries among these interrupted surfaces are inline and staggered parallel-plate fins, while the more complicated geometries are louvered fins.

Surface interruption prevents the continuous growth of the thermal boundary layer by periodically interrupting it. Thus the thicker thermal boundary layer in continuous plate fins, which offers higher thermal resistance to heat transfer, is maintained thin and its resistance to heat transfer is reduced by surface interruption. Previous experimental and numerical studies have shown that heat transfer enhancement occurs even at low Reynolds numbers when the flow is steady and laminar [Sparrow and Liu (1979), Patankar and Prakash (1981)]. At higher Reynolds numbers, above criticality, surface interruption offers an additional mechanism of heat transfer enhancement by inducing self-sustained oscillations in the flow in the form of shed vortices. These vortices enhance local heat transfer by continuously bringing fresh fluid towards the heat transfer surface [Jacobi and Shah (1995), Valencia et al. (1996)]. In addition to heat transfer enhancement, the surface interruption also increases the pressure drop and thus requires higher pumping power. This is partly due to the higher skin friction associated with the hydrodynamic boundary layer restarting, and also due to the Stokes layer dissipation [Amon and Mikic (1991)] and higher Reynolds stresses [Mittal and Balachandar (1995)] in the unsteady flow regime. Thus, the boundary layer restart and the self-sustained oscillatory mechanisms simultaneously influence both the overall heat transfer and pumping power requirement. Therefore, design optimization must take into account the impact of design parameters

on the relative importance of the different heat transfer enhancement mechanisms and their attendant effect on pumping cost. Furthermore, from the fluid dynamics viewpoint, the flow in these interrupted surfaces provides a rich kaleidoscope of flow phenomena. Depending on the Reynolds number and the fin geometry, flow within these interrupted surfaces can be laminar with or without flow separation, transitional or turbulent [Yang (1983)].

The traditional approaches to improve compact heat exchanger design with these interrupted surfaces are: acquisition of overall heat exchanger performance data through experiments, correlation of empirical data and experimental observation of the convection process. Acquisition of overall performance data has been successful for each particular geometry tested but still remains expensive due to the large number of parameters involved and is of limited use in understanding heat transfer enhancement mechanisms. Experimental observation of the convection process using flow visualization has been successful in exploring the heat transfer enhancement mechanisms, but is only of qualitative value.

Computational modeling of these flows has been used in the past and is becoming increasingly popular, because it can provide detailed information about the heat transfer enhancement mechanisms if the model is correct. However, most previous numerical studies have made crucial assumptions in solving the Navier-Stokes and energy equations, namely the flow and thermal fields have been assumed to be steady and two-dimensional. For example, Sparrow and Liu (1979) studied heat transfer on a series of parallel infinitesimally thin flat plates placed in inline and staggered arrangements. By using an approximate parabolic form of the steady Navier-Stokes and energy equations, they included the entrance and exit effects. Patankar and Prakash (1981) solved the Navier-Stokes and energy equations under the steady state assumption to study the heat transfer from a series of finite thickness plates in a staggered arrangement. This and their earlier study [Patankar et al. (1977)] have provided an analytical/computational framework within which the thermal behavior of a large array of fins can be modeled by assuming the flow to be periodic along the streamwise direction.

The assumption of steady flow and thermal fields precludes much of the flow physics, particularly in flow regimes where the flow is dominated by large scale time-dependent variations. With the

advent of high performance supercomputers, large-scale numerical simulations are becoming more realistic. It is now possible to obtain accurate time-dependent solutions with far fewer assumptions about the problems and to explore the full range of rich physics. For example, recent simulations of flows in grooved and communicating channels by Ghaddar et al. (1986) and by Amon and Mikic (1991) included time-dependence. Their studies showed that the flow physics associated with flow separation at higher Reynolds numbers is too complex to be accounted for with steady state computations. Furthermore, even in the case of nominally two-dimensional fins, at sufficiently high Reynolds numbers, due to intrinsic instabilities, the flow becomes three-dimensional and the effect of three-dimensionality on heat transfer and friction loss can be significant as observed in the study of flow over circular cylinders [Williamson (1988), Mittal and Balachandar (1995)] and flow over a blunt plate [Tafti and Vanka (1991)].

In spite of these recent efforts, the details of the boundary layer restart and self-sustained oscillatory enhancement mechanisms have not been isolated and investigated in detail. In particular, in the context of parallel-plate fin heat exchangers, a clear understanding of the individual roles of boundary layer restart and vortex shedding mechanisms on heat transfer and friction factor is lacking. Flow visualizations have shown that vortices roll up near the leading edge of the fins and subsequently travel downstream along the fin surface [Joshi and Webb (1987)]. Von Karman vortices are also observed to form at the trailing edge of the fins and travel downstream in the wake before encountering the next fin element. A number of important issues regarding how the vortices are generated and how they interact with the parallel-plate fins still remain to be explored. Vortical flows are considered to enhance overall heat transfer [Jacobi and Shah (1995), Valencia et al. (1996)], but their impact on local heat transfer and skin friction in a compact heat exchanger needs to be quantified. Similarly the effect of wake vortex shedding on form drag needs to be quantified. Furthermore, the rate at which the strength of the leading edge vortex decreases as it travels over the fin surface is unclear, but such it may have significant impact on design parameters such as fin length and fin thickness.

The primary objective of the present study is to isolate the individual mechanisms through controlled numerical simulations of flow and heat transfer in parallel-plate fins. Two different arrange-

ments of the parallel-plate geometry, inline and staggered, are investigated over a range of Reynolds numbers. At higher Reynolds numbers when the flow is naturally unsteady, along with the time-dependent simulations, corresponding steady state simulations are performed by enforcing symmetry about the wake centerline. A comparison of the unsteady and steady symmetrized simulation results is used in exploring the unsteady enhancement mechanism due to vortex shedding. These results are compared to the theoretical results for fully developed flow between uninterrupted continuous parallel plates and those of restarted boundary layers over fins of negligible thickness [Sparrow and Liu (1979)] in order to further separate the role of the boundary layer restart mechanism and the geometry effects arising from finite fin thickness and fin arrangement.

At high Reynolds numbers, the difference between two-dimensional and three-dimensional simulations has not been fully understood, especially its effect on heat transfer. The strength of spanwise vortices between two-dimensional and three-dimensional simulations has not been compared, and the effect of streamwise vortices in three-dimensional simulations on heat transfer and friction loss has not been identified in the current geometry. At sufficiently high Reynolds numbers, corresponding three-dimensional simulations have also been performed to identify the effect of intrinsic three-dimensionality.

These effects have been investigated over a range of Reynolds numbers, for parallel-plate fins, which are well within typical compact heat exchanger operating conditions. A finite-volume based numerical algorithm has been used to solve the incompressible Navier-Stokes and energy equations in two- or three-dimensions in a time-accurate manner. A computer program based on this methodology has been implemented on the massively parallel CM-5 in the Single Instruction Multiple Data (SIMD) or the data parallel programming paradigm [Tafti (1995), Zhang et al. (1996)].

In addition, in the study of flow over louvered fins, though three different flow regimes have been observed in flow visualizations, the pattern of the local Nusselt number distribution has not been related to the flow regime. Here, time-dependent simulations of flow and heat transfer in a simplified louvered fin geometry have been performed in two-dimensions over a range of Reynolds numbers. Different flow regimes have been identified within the simulated Reynolds number range and results have been compared with corresponding theoretical results. For this purpose, a computer

program based on general body fitted coordinates has been used on the SGI Power Challenge arrays [Tafti (1996)].

1.2 Literature Review

Over the past several decades, a large body of work has been done towards understanding heat transfer and pressure drop in compact heat exchangers using interrupted surfaces. Though various interrupted fin surfaces have been studied in the past, this review only considers geometries relevant to the current study and is organized in two sections: one deals with parallel-plate fins and the other deals with louvered fins.

1.2.1 Flow and Heat Transfer in Parallel-Plate Fin Heat Exchangers

There are two types of parallel-plate fins normally considered: inline and staggered fins. Inline fins can be obtained by cutting continuous parallel plates and placing the flat plate fins aligned with each other as shown in Figure 1.1. Staggered fins can be obtained by offsetting every other row or column of the inline fins. Staggered fins are also known as offset-strip fins and Figure 1.2 shows a typical offset-strip fin heat exchanger and the cross-section of the staggered fins.

Patankar et al. (1977) formulated a generalization of the concepts of fully developed flow and heat transfer in a periodic array of fin elements. The pressure and temperature were each broken into a streamwise linear part and a perturbation counterpart, and then periodic boundary conditions were applied for the perturbation. The modified Navier-Stokes and energy equations were solved through iterations. The flow was assumed to be fully developed, steady and laminar. Thus, a symmetry boundary condition was applied in the transverse direction on the computational domain boundaries. The fin thickness was also neglected.

Sparrow et al. (1977) analytically and numerically studied flow and heat transfer in infinitesimally thin and interrupted flat plate isothermal fins with a uniform entering flow. In their solution, the Navier-Stokes and energy equations had been simplified by the boundary layer approximation and by assuming a steady solution, the effects of flow unsteadiness and vortex shedding were neglected. Under conditions of equal pumping power and equal heat transfer surface area, they pre-

dicted a heat transfer enhancement for these interrupted surfaces of nearly *80%* over otherwise continuous plates. In addition, their calculated results demonstrated the existence of a new type of fully developed regime, one that is periodic. At a sufficiently large downstream distance, the velocity and temperature profiles repeat their values at successive axial fins and the average heat transfer coefficient for each fin takes on a constant value.

Cur and Sparrow (1978) experimentally studied the heat transfer and pressure drop of a pair of co-linear interrupted plates aligned with the flow direction in a channel. Although their study focused on the overall performance, they did point out two important mechanisms of heat transfer enhancement in interrupted surfaces: boundary layer restarting and oscillatory mixing.

Sparrow and Liu (1979) compared the heat transfer, pressure-drop and performance relationships for inline, staggered and continuous parallel-plate heat exchangers through a numerical study using the finite difference method. Steady Navier-Stokes and energy equations were solved in a domain of more than ten arrays of fins in the streamwise direction including the entrance region but with negligible fin thickness. Their study clearly showed that in the steady laminar flow regime, both inline and staggered geometries resulted in higher heat transfer and pressure drop than continuous parallel plate fins. Parametric effects were also studied for each geometry and it was observed that by increasing plate length, both the Nusselt number and the pressure drop decrease monotonically for all geometries studied. It was also found that the pressure drop and heat transfer for the inline fins are higher than that of the staggered fins.

Sparrow and Hajiloo (1980) conducted experimental measurements on heat transfer and pressure drop for an array of staggered plates aligned parallel to the flow, using the naphthalene sublimation technique. For a given operating condition, the per-plate heat transfer coefficient was found to be constant for the second the all subsequent rows. Thus, their experiments provided evidence for the hypothesis regarding the periodicity of flow and heat transfer characteristics in a large array of fins proposed by Patankar et al. (1977). The fully developed heat transfer coefficients increase with Reynolds number for all the plate thicknesses investigated, but in a different manner for the different thickness. Thicker plates give rise to higher heat transfer coefficients and also higher frictional loss.

Patankar and Prakash (1981) numerically studied the effect of plate thickness in staggered fins. A periodic velocity boundary condition was applied in the streamwise direction. However, the flow was assumed to be steady and laminar, and thus symmetry was applied in the transverse direction. Their calculations have shown that by varying fin thickness at fixed Reynolds numbers based on the hydraulic diameter, the flow pattern changes, resulting in significant differences in the overall heat transfer and frictional loss.

Yang (1983) noted that flow past interrupted surfaces should exhibit a periodic unsteady behavior at sufficiently high Reynolds numbers, and he applied stability analysis to identify the Reynolds number range for this unsteady flow. Yang also observed that a change in the slope of the Colburn j factor versus Reynolds number curve at a certain Reynolds number was due to the presence of flow unsteadiness. He defined the flow from the onset of self-sustained flow oscillations to the onset of laminar-turbulent transition as the "second laminar regime". He also stated that this "second laminar regime" enjoys the benefit of heat transfer enhancement without the perils of flow-induced vibration and noise.

Mullisen and Loehrke (1986) explored the flow structures in inline and staggered fins using Schlieren visualization techniques and identified the flow mechanisms responsible for heat transfer enhancement in interrupted-plate fin heat exchangers. Their experimental data and corresponding flow visualization showed that in addition to the augmentation induced by the boundary layer restarting effect, heat transfer augmentation can be expected over some range of operating conditions due to unsteady flow induced by the surface interruptions. Three distinctly different flow regimes were observed for inline and staggered plates, which are classified as steady, general unsteady and periodic unsteady flows.

Joshi and Webb (1987) presented analytical models to predict the heat transfer and friction loss of offset-strip fin heat exchangers. A critical Reynolds number based on the hydraulic diameter, Re^*, corresponding to the onset of oscillating unsteady flow was defined based on the Blasius flat plate solution. For Reynolds numbers lower than this critical Reynolds number, flow was defined as laminar and solutions were obtained by interpolating the numerical solutions of Sparrow and Liu (1979). In the turbulent flow regime, estimated to be $Re \geqslant Re^* + 1000$, different correlations were developed

for predicting overall heat transfer and frictional loss. Thus, their study did not predict any overall performance in the "second laminar regime" as defined by Yang (1983). Furthermore, they pointed out that form drag contributes significantly to the friction factor and they had incorporated this contribution in obtaining friction factor correlations. They also argued that since the heat transfer at the front and back fin surfaces account for less than *5%* of the total heat transfer, the effect of fin thickness on overall heat transfer can be neglected. Though their flow visualizations confirmed the existence of a self-sustained oscillatory flow, they did not explore the corresponding heat transfer enhancement mechanism in detail.

Xi et al. (1991) used flow visualization in studying flow and heat transfer over offset-strip fins and observed that as Reynolds number increases, the flow proceeds from laminar flow to unsteady flow in which the wake exhibits either sinusoidal motion or shed vortices. It is the wake flow instability that causes additional heat and momentum transfer, resulting in the deviation of the j factor and friction factor from that of continuous parallel plates as observed in previous experimental studies.

Manglik and Bergles (1995) correlated the overall performance data of offset-strip fin heat exchangers in the literature. They observed that three different flow regimes exist for these data, namely that laminar, transitional and turbulent. They also presented continuous correlation curves over the three flow regimes for the j factor and friction factor in terms of the Reynolds number and geometrical parameters. Furthermore, they observed that vortex shedding, affected by fin spacing, fin thickness and fin length, acts as freestream turbulence to increase heat and momentum transfer.

1.2.2 Flow and Heat Transfer in Louvered Fin Heat Exchangers

Although louvered fin surfaces have been in existence since the 1950's, it has been only within the past 20 years that serious attempts have been made to understand the flow phenomena and performance characteristics. Figure 1.3 shows the cross-section of a louvered fin array. This array includes an inlet deflection fin, a middle deflection fin, an outlet deflection fin and some inclined plate fins.

Beauvais (1965) was the first to conduct flow visualization experiments on the louvered fin arrays shown in Figure 1.3. A smoke flow visualization technique was used in his study and thus the

results were only of qualitative value. His experimental results showed that the mean flow was nearly parallel to the louvers for all the cases he tested.

Davenport (1983) performed flow visualization experiments identical to those of Beauvais and demonstrated that the flow structure within the louvered fin array was a function of the Reynolds number based on the louver pitch. The friction factor data show apparent agreement with the Blasius solution of flat plates. The slope of the friction factor curve is very close to the Blasius slope at low Reynolds numbers, but it flattens at higher Reynolds numbers. Thus, he concluded that the heat transfer enhancement mechanism in louvered fins is mainly laminar boundary layer restarting with additional effects arising from bluff edges and air-turning losses.

Achaichia and Cowell (1988a) experimentally studied flow and heat transfer in louvered fin geometries and plotted the Stanton number as a function of the Reynolds number based on the fin length . At high Reynolds numbers, the Stanton number curve is parallel to and lower than that of laminar boundary layer flow over a flat plate. At low Reynolds numbers, the Stanton number curve showed the same characteristics as that of a laminar duct flow. They also numerically modeled the flow through louvered fin arrays, assuming a fully developed, periodic steady laminar flow [Achaichia and Cowell (1988b)]. Their analysis showed that as the Reynolds number approaches large values, the mean flow angle approaches the louver angle to within a few degrees, which supports Davenport's hypothesis regarding the boundary layer development on louvered fins as the Reynolds number increases. However, at higher Reynolds numbers when eddies are shed from the louvers, the flow is no longer parallel to the louvered fins. Combining the experimental data with numerical analysis, they developed correlations for Stanton number and friction factor in terms of geometric parameters and Reynolds number based on fin length, ranging *120* to *8000*.

Aoki et al. (1989) measured the distribution of heat transfer coefficients in multilouvered fins. The locally averaged heat transfer coefficients for the individual louvers in the louvered fin array were obtained by measuring the electric power input for the film and the temperature difference between the fin element and air. They observed that the heat transfer coefficients of fins which were downstream from the middle deflection fin to be slightly less than those of upstream fins.

Suga et al. (1990) numerically studied flow and heat transfer characteristics of louvered fins using the finite difference method with overlaid grids. Their simulation assumed the flow to be two-dimensional, steady, laminar and periodic in the transverse direction, with finite fin thickness. They studied the geometry effect and concluded that the louvered fin design could be improved through controlling the size of the thermal wake.

Hiramatsu et al. (1990) employed an oblique grid fitting to the louvered fins, also using the finite difference method to simulate the flow in louvered fins with the same assumptions as those of Suga et al. (1990). They analyzed the flow over a range of Reynolds numbers (based on louver pitch) from *100* to *500* and louver angles from $0°$ to $50°$. They also performed flow visualization on louvered fins by injecting ink into the flow for a louver angle of $25°$. They concluded that the large fin pitch and low Reynolds numbers make it hard for the fluid to go through the louvers, and as a result, the heat transfer decreases.

Webb and Trauger (1991) performed flow visualization in louvered fins over a Reynolds number (based on louver pitch) range from *400* to *4000*, using a dye injection technique. Geometrical parameters such as louver pitch, louver angle, and fin pitch were varied to determine their effect on the flow structure. They defined a dimensionless quantity of flow efficiency in terms of the mean flow angle relative to the louver angle. Correlations were developed to predict the flow efficiency as a function of geometrical parameters and the Reynolds number. In addition, they found the flow to be laminar for Reynolds numbers less than approximately *500* to *600*, and that at higher Reynolds numbers reducing the fin pitch leads to wake instability and results in higher heat transfer.

Cowell et al. (1995) presented an overview of the operating mechanisms of louvered fin heat transfer surfaces. They derived a correlation for the Stanton number in terms of the Reynolds number and varying geometric parameters. Comparing louvered fins to offset-strip fins, they observed that for a fixed amount of heat transfer, louvered fins can have a larger hydraulic diameter, which implies less fin surface area or less weight and material. They concluded that the flow-directing property of the louvered fin arrays effectively increases the velocity of the working fluid relative to the elemental flat-plate surfaces. However, the reason why louvered fins should display better performance than the equivalent offset-strip fins is yet to be understood.

It is shown from the above that the flow structures and heat transfer characteristics in the multi-louvered fin geometry shown in Figure 1.3 are very complex, and optimizing the design of louvered fin heat exchangers is still a challenge. Most existing experimental studies emphasized overall performance measurements. Realistic analytical and numerical modeling of these complex flows without much simplifications is virtually impossible. Thus, during the last decade, researchers have started developing an understanding of the flow characteristics and heat transfer enhancement mechanisms in a related but simpler louvered fin geometry, where there are no deflection fins and all the fins arranged with the same angle of attack.

Lee (1986) applied the naphthalene sublimation technique to analyze flow and heat transfer in the simplified louvered fins, with angles of attack of *20°, 25°, 30°* and *35°* for Reynolds numbers based on the hydraulic diameter ranging from *350* to *5000.* Eight rows of fins in the streamwise direction and three columns of fins in the transverse direction were used. It was found that the heat transfer coefficients of individual plates were identical except that the first plate had a slightly higher coefficient. Therefore, most mass transfer measurements were conducted only on the middle column and the other two columns were used to simulate a fully developed flow field. The heat transfer coefficients of the forward and backward sides of the plates were separately determined and it was observed that the heat transfer coefficients on the forward side are higher than those on the back side within the tested Reynolds number range.

Zhang and Lang (1989) performed a study of the effect of plate angle and length on heat transfer and pressure drop in a simplified louvered fin array similar to that of Lee. They also employed the naphthalene sublimation technique. They investigated different plate lengths and angles of attack ranging from *10°* to *35°* for Reynolds numbers based on the interrupted plate length from *380* to *2300.* Their experimental data indicated that the Sherwood number, which corresponds to the Nusselt number through the heat and mass transfer analogy, becomes a constant after the first four rows in the streamwise direction and, thus, the fully developed region of heat transfer is achieved.

Pang et al. (1990) numerically studied the fully developed steady laminar flow and heat transfer for arrays of interrupted plates positioned convergently and divergently along the flow direction using a finite-volume method. The steady Navier-Stokes and energy equations were

solved with negligible fin thickness. Periodic boundary conditions along the streamwise direction and symmetry boundary conditions along the transverse direction were applied. Their calculations showed that the heat transfer rate of the forward fin surface was much higher than that of the backward fin surface. For all the cases studied, they have found that the average Nusselt number and friction factor as well as the size of recirculating zone increase with the louver angle and the Reynolds number.

Huang and Tao (1993) used the naphthalene sublimation technique to study the heat transfer and pressure drop characteristics for arrays of nonuniform plate lengths, aligned with an angle of *25°* to the flow direction. Length ratio of successive plates was *1.5* to *2.5* and Reynolds numbers based on the shorter plate length was varied from *198* to *1660*. They discovered that the flow became fully developed from the fifth unit, where each unit includes one long plate and one short plate. In addition, they compared the performance of nonuniform plate lengths with that of uniform plate lengths under two constraints: fixed pumping power and fixed pressure drop, and found that the thermal performance of the array with nonuniform plate lengths is better than that of the array with a uniform plate length.

Figure 1.1 Schematic of the inline fin geometry.

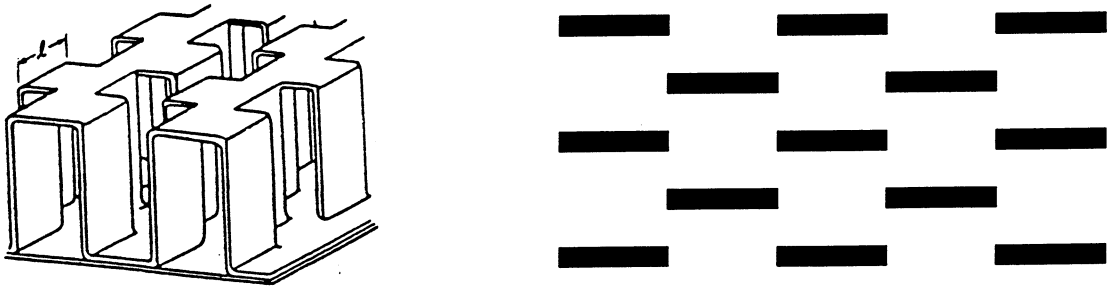

Figure 1.2 (a) Geometry of the offset strip-fin heat exchanger; (b) Cross-section of the offset strip-fin heat exchanger, also named as staggered geometry.

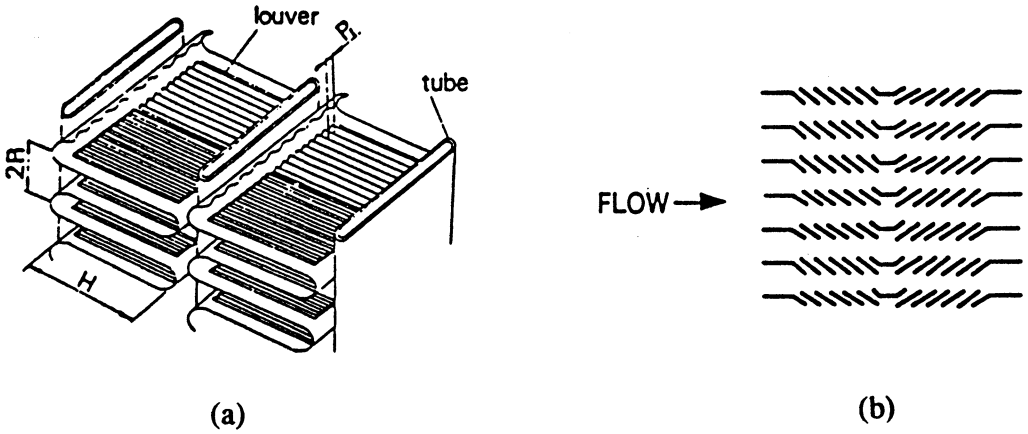

Figure 1.3 (a) Geometry of a flat-sided tube and louvered fin heat exchanger; (b) Cross-section of the louvered fin heat exchanger.

CHAPTER 2. SIMULATION METHODOLOGY

2.1 Governing Equations

For computational purposes, a large array of fins can be approximated by a simpler system consisting of periodic repetition of a basic unit and the computational domain can be limited to this basic unit. Implicit in this treatment is the assumption that the flow is fully developed, both hydrodynamically and thermally, in the fin array entrance or exit effects are excluded. Such fully developed flow regime is observed to be attained by the second row in the streamwise direction in the experiments of parallel-plate fins by Sparrow and Hajiloo (1980), and by the fifth row in the streamwise direction in the experiments of louvered fins by Zhang and Lang (1989). In the parallel-plate fins we consider both inline and staggered parallel-plate arrangements which are shown in Figure 2.1. In the inline arrangement fins of dimensional thickness, b^*, and length, L^*, form a periodic pattern with pitches L_x^* along the flow direction, x, and $L_y^* = 2H^*$ along the transverse direction, y. Thus the basic unit, indicated by the dashed line, contains a single fin. Here we consider a large array of this basic unit periodically repeated along the streamwise and transverse directions and Figure 2.1(a) shows only six basic units of this large array. Figure 2.1(b) shows the staggered arrangement obtained by shifting the alternate rows of fins in the flow direction by half a wavelength in the x direction, $L_x^*/2$. This arrangement is of primary interest to the study of heat transfer enhancement mechanisms because it serves as a simplified model for offset-strip fins. Figure 2(c) shows another kind of staggered fin arrangement, staggered_II, obtained from the inline arrangement by shifting the alternate columns of fins in the transverse direction by a half wavelength in the y direction, $L_y^*/2$. For both staggered arrangements, the basic unit now contains two fin elements, again marked by the dashed line, and the basic unit is periodically repeated along the streamwise and transverse directions. Different cases have been studied in the inline and staggered arrangements which will be discussed in detail in Chapter 3 and corresponding parameters are listed in Table 3.1 and Table 3.2, respectively, for the inline and staggered arrangements. Figure 2.2 shows currently simulated louvered fin geometry

and within the dash line is the computational domain with computational lengths of $L_x^* = 7.2H^*$ and $L_y^* = 8H^*$, a fin thickness of $0.75H^*$ and a louver angle of $\theta = -25°$

The time-dependent, incompressible continuity, momentum and energy equations are of the following *nondimensional* forms:

$$\frac{\partial u_i}{\partial x_i} = 0 \tag{2.1}$$

$$\frac{\partial u_i}{\partial t} + \frac{\partial (u_i u_j)}{\partial x_j} = -\frac{\partial P}{\partial x_i} + \frac{1}{Re_\tau}\frac{\partial^2 u_i}{\partial x_j^2} \tag{2.2}$$

$$\frac{\partial T}{\partial t} + \frac{\partial (u_j T)}{\partial x_j} = \frac{1}{Re_\tau Pr}\frac{\partial^2 T}{\partial x_j^2} \tag{2.3}$$

where $i = 1, 2, 3$ correspond to $x(u)$, $y(v)$, $z(w)$ coordinates (velocities) in the three Cartesian directions, respectively. Here constant material properties along with negligible viscous dissipation and body forces have been assumed. Equations (2.1), (2.2) and (2.3) are nondimensionalized by the half distance between adjacent fin rows along the transverse direction (H^*) as the length scale, the friction velocity ($u_\tau^* = (\Delta P^*/\rho)^{1/2}$) as the velocity scale, the applied dimensional pressure difference (ΔP^*) over a length of H^* along the streamwise direction as the pressure scale, H^*/u_τ^* as the time scale and $q"^*H^*/k$ as the temperature scale. Here q^* is the specified dimensional constant heat flux on the fin surfaces and k is the thermal conductivity of the fluid. The above nondimensionalization results in two dimensionless parameters: Reynolds number based on friction velocity, $Re_\tau = u_\tau^* H^*/\nu$, and Prandtl number $Pr = \nu/\alpha$, where ν and α are the kinematic viscosity and thermal diffusivity of the fluid, respectively. In all the computations to be presented here the Prandtl number is set to 0.7, corresponding to that of air. Here nondimensional quantities will primarily be considered. Any use of dimensional quantities will be explicitly stated and denoted by a superscript (*) except for the constant material properties.

2.2 Treatment of Periodic Boundary Conditions

The periodic nature of the geometry along the streamwise and transverse directions allows for the possibility of periodic solutions to the above governing equations, but application of periodic

boundary conditions for pressure and temperature fields along the streamwise direction is not straight forward. While pressure decreases along the flow direction, temperature either increases or decreases along the flow direction depending on the heat transfer between the fluid and the fin surface. It has been well established in the past [Patankar et al. (1977), Patankar and Prakash (1981), Ghaddar et al. (1986), Amon and Mikic (1991)] that these variations in the mean pressure and temperature along the flow direction can be subtracted to define a modified pressure and temperature, which can admit periodic solutions along both the streamwise and transverse directions. This necessitates reformulation of the governing equations (2.1) - (2.3) in terms of the modified variables.

The nondimensional total pressure P will be separated into a linear component and a modified nondimensional pressure p as follows:

$$P(x,y,z,t) = P_{in} - \beta x + p(x,y,z,t) \tag{2.4}$$

where P_{in} is the arbitrary nondimensional pressure at the inlet of the computational domain, and β is the linear component of the nondimensional pressure gradient in the flow direction. Therefore by choosing β to be a constant (in this case unity), the linear pressure variation can be made to completely account for the mean pressure drop across the computational domain and the modified nondimensional pressure p can then be assumed to be periodic along both the streamwise and transverse directions. Thus the resulting mean pressure difference across the computational domain balances the friction loss within the computational domain. By substituting Equation (2.4) for the total pressure into the momentum equation, Equation (2.2), the following equation for the modified nondimensional pressure can be obtained

$$\frac{\partial u_i}{\partial t} + \frac{\partial (u_i u_j)}{\partial x_j} = \delta_{i1} - \frac{\partial p}{\partial x_i} + \frac{1}{Re_\tau}\frac{\partial^2 u_i}{\partial x_j^2} \tag{2.5}$$

where δ_{i1} is the Kronecker delta, and the index $i = 1$ denotes the streamwise or flow direction.

Therefore in the present computations the streamwise nondimensional pressure gradient is held fixed and the computed flow rate adjusts itself over time in order for the friction loss to instantaneously balance the applied pressure force. It must be pointed out that the linear pressure variation accurately accounts for the mean pressure variation only across the entire streamwise periodic boundaries. The actual mean nondimensional pressure variation along the streamwise direction will

significantly depart from the linear variation and therefore the mean streamwise gradient of the modified nondimensional pressure, defined as

$$\frac{\partial}{\partial x}\left[\frac{1}{L_y L_z}\int_{-L_y/2}^{L_y/2}\int_0^{L_z} p(x,y,z,t)dzdy\right]$$

will in general be nonzero. But the mean modified nondimensional pressure difference across the computational domain

$$\int_0^{L_x/2}\frac{\partial}{\partial x}\left[\frac{1}{L_y L_z}\int_{-L_y/2}^{L_y/2}\int_0^{L_z} p(x,y,z,t)dzdy\right]dx$$

will be identically zero.

Based on the above arguments periodic boundary conditions of the following general form can be applied for both the nondimensional velocity and modified nondimensional pressure

$$u_i(x + nL_x, y + mL_y, z, t) = u_i(x, y, z, t) \tag{2.6}$$

$$p(x + nL_x, y + mL_y, z, t) = p(x, y, z, t) \tag{2.7}$$

In the above it is assumed that the computational domain consists of n rows of fins in the x direction and m columns of fins in the y direction. Such general periodic boundary conditions as a model for flow over a periodically repeating geometry have been considered in the past by Patankar and coworkers in studying flow and heat transfer in inline and staggered parallel-plate fins [Patankar et al. (1977), Patankar and Prakash (1981)]. This approach has also been adopted by more recent investigators such as Ghaddar et al. (1986), Amon and Mikic (1991) in studying flow and heat transfer in grooved and communicating channels. Here results will be presented for the case of $m = 1$ and $n = 1$, thus, effects of subharmonics have been neglected.

On the fin surfaces, the no slip and no penetration boundary conditions are applied for the velocities while a Neumann boundary condition of the following type is applied for the modified nondimensional pressure [Gresho and Sani (1987), Williams and Baker (1996)].

$$\nabla p \cdot \hat{\boldsymbol{n}} = 0 \qquad \text{on } \partial D_{fin} \tag{2.8}$$

where $\hat{\boldsymbol{n}}$ is the outward unit vector normal to the fin surface denoted by ∂D_{fin}.

Similarly the nondimensional temperature, T, can be decomposed into a linear part and a modified nondimensional temperature, θ, as

$$T(x,y,z,t) = T_{in} + \gamma x + \theta(x,y,z,t) \tag{2.9}$$

where T_{in} is the arbitrary nondimensional inlet temperature and γx specifies the linear portion of the nondimensional temperature variation along the flow direction due to the constant heat flux boundary condition on the fin surface. This linear portion is so chosen that it fully accounts for the net temperature change from the inlet to the outlet of the computational domain. Performing a global energy balance gives a dimensional mean temperature change of $q"^{*}\Omega_f^{*}/(\rho C_p Q^{*} L^{*}_z)$ from the inlet to the outlet of the domain, where Ω_f^{*} is the fin surface area, C_p is the specific heat of the fluid, L^{*}_z is the spanwise width of the fin, and Q^{*} is the flow rate per unit width along the z direction. Hence, the nondimensional temperature gradient can be written in terms of the corresponding nondimensional variables as:

$$\gamma = \frac{\mathcal{P}}{Re_\tau Pr\, Q L_x} \tag{2.10}$$

where $\mathcal{P}$ is the sum of nondimensional perimeters of all the fins within a basic unit. By substituting the nondimensional temperature decomposition, Equation (2.9), into the energy equation, Equation (2.3), and ignoring any time dependence of γ, we obtain an equation for the modified nondimensional temperature as:

$$\frac{\partial \theta}{\partial t} + u\gamma + \frac{\partial (u_j \theta)}{\partial x_j} = \frac{1}{Re_\tau Pr} \frac{\partial^2 \theta}{\partial x_j^2} \tag{2.11}$$

where the modified nondimensional temperature θ can also be considered to be periodic along the streamwise and transverse directions and must satisfy the following general conditions:

$$\theta(x + nL_x, y + mL_y, z, t) = \theta(x,y,z,t) \tag{2.12}$$

Furthermore from Equation (2.8), the constant heat flux at the fin surface reduces to the following boundary condition for the modified temperature at the fin surface

$$(\nabla\theta)\cdot\hat{n} = 1 - \gamma \hat{e_x}\cdot\hat{n} \qquad on\ \ \partial D_{fin} \tag{2.13}$$

where $\hat{e}_x$ is the unit vector in the x direction.

From the above discussion it is clear that the definition of modified nondimensional temperature according to Equation (2.9) and the subsequent periodic boundary condition in the streamwise direction on computational boundaries were made possible by the constant heat flux boundary condition,

which provided a precise measure of the temperature difference between the inlet and outlet of the computational domain. With an isothermal boundary condition, since the fluid temperature continuously either increases or decreases downstream depending on the direction of heat transfer between the fin surface and the fluid, application of the periodic thermal boundary condition along the streamwise direction is not straightforward. Modified temperature and appropriate periodic boundary conditions based on a self-similar development of the thermal profile have been proposed by Patankar et al. (1977) in the steady flow regime. Formulation of the periodic self-similar development of the thermal field under the isothermal condition has not been performed in the unsteady flow regime.

In the three-dimensional computations the spanwise direction is considered to be periodic and periodic boundary conditions were applied for the velocity, pressure and temperature fields along the z direction. The present computations to be reported were performed with a nondimensional spanwise extent of $4b$. At Reynolds numbers just above the critical value for the onset of three-dimensionality as considered here, it has been observed that wake behind bluff bodies [Williamson (1988), Wu et al. (1994), Mansy et al. (1994) and Henderson (1994)] exhibits three-dimensionality in the form of periodic structures with spanwise wave lengths ranging from 0.8 to 4 times the height of the bluff body. But no such results exist for flow around a periodic array of flat plates of finite thickness and based on the bluff body results a spanwise extent of $4b$ is chosen to capture the essential three-dimensional physics and topological features of the flow, with adequate resolution along the spanwise direction. Although a larger computational domain along the spanwise direction may be desirable, the corresponding well resolved simulations can be prohibitively expensive.

2.3 Discretization of the Governing Equations

The numerical approach followed here is direct simulation where the governing equations are solved faithfully with all the relevant length and time scales adequately resolved and no turbulence models employed. Two different codes have been used in the present study. The first code is used in the simulation of flow and heat transfer in parallel-plate fins, and a second-order accurate finite difference formulation which is similar to the Harlow-Welch scheme [Harlow and Welch (1965)]

is employed [Tafti (1995), Zhang et al. (1996)]. Equations (2.1), (2.5) and (2.11) are solved on a staggered Cartesian grid in which the velocity nodes are staggered halfway from the scalar nodes in their respective coordinate directions. A two-dimensional equivalent of the staggered grid is shown in Figure 2.3. The second code is used in the study of flow and heat transfer in louvered fins. Due to the irregular geometry of the louvered fins, a general boundary-conforming transformation of type $\bar{x} = \bar{x}(\bar{\xi})$ is used in order to map the physical space, $\bar{x}$, to the logical/computational space, $\bar{\xi}$. The resulting equations are solved in computational space on a non-staggered grid with the Cartesian velocities as dependent variables [Tafti (1996b)]. Figure 2.4 shows a typical grid used in the current louvered fin simulations. The governing equations are discretized using a finite-volume formulation in which the volume integrals are reduced to surface fluxes on the cell faces for the convection and viscous terms. The convection and viscous terms are approximated by second-order central differences.

Time integration of the discretized momentum equations is performed by using the fractional-step method [Chorin (1968), Kim and Moin (1985)]. Briefly described here, first an intermediate velocity field is calculated by neglecting the contribution from the pressure gradient term to the momentum balance. The time advancement of this step is performed by using an explicit second-order accurate Adams-Bashforth approximation as shown below symbolically

$$\frac{u_i^* - u_i^n}{\Delta t} = \delta_{i1} + \frac{3}{2} I_i^n - \frac{1}{2} I_i^{n-1} \tag{2.14}$$

where $u_i{}^*$ denotes the intermediate velocity field and I_i is defined as

$$I_i = -\frac{\partial (u_i u_j)}{\partial x_j} + \frac{1}{Re_\tau} \frac{\partial^2 u_i}{\partial x_j^2} \tag{2.15}$$

The above step accounts for only the viscous and inertial effects. Next the intermediate velocity, u_i^*, is made divergence-free by solving the pressure Poisson equation for p^{n+1} and the correction to the intermediate velocity field to account for the pressure effect is given by

$$u_i^{n+1} = u_i^* - \Delta t \frac{\partial p^{n+1}}{\partial x_i} \tag{2.16}$$

where the pressure field, p^{n+1}, is obtained by satisfying the continuity equation at time $(n+1)$, resulting in the following pressure Poisson's equation

$$\frac{\partial}{\partial x_i}\left(\frac{\partial p^{n+1}}{\partial x_i}\right) = \frac{1}{\Delta t}\frac{\partial u_i^*}{\partial x_i} \tag{2.17}$$

The energy equation is advanced in time by using a fully explicit second-order Adams-Bashforth approximation as follows:

$$\frac{\theta^{n+1} - \theta^n}{\Delta t} = -\gamma u^{n+1} + \frac{3}{2}E^n - \frac{1}{2}E^{n-1} \tag{2.18}$$

where

$$E = -\frac{\partial(u_j\theta)}{\partial x_j} + \frac{1}{Re_\tau Pr}\frac{\partial^2\theta}{\partial x_j^2} \tag{2.19}$$

In a typical simulation, the hydrodynamic flow field is allowed to reach a fully developed state before the heat transfer calculations are initiated. The definition of the fully developed state depends on the flow regime. For flows at low Reynolds numbers, which do not exhibit any vortex shedding, the nondimensional flow rate Q will be truly time-independent in the fully developed state. In flow regimes with vortex shedding, Q will only exhibit constancy when averaged over some suitable ensemble. It is found that even at the highest Reynolds numbers considered here, the instantaneous Q varies less than 1% from its mean value, and correspondingly from Equation (2.10), the neglected time variation in the nondimensional temperature gradient, γ, is also negligible. Once the flow rate has reached a fully developed state, the heat transfer calculations are initiated with an arbitrary initial field of $\theta = 0$. Subsequently the time evolution of the average Nusselt number over the fin surface is monitored to determine the thermal fully developed state. Results provided here are obtained in the hydrodynamically and thermally fully developed state.

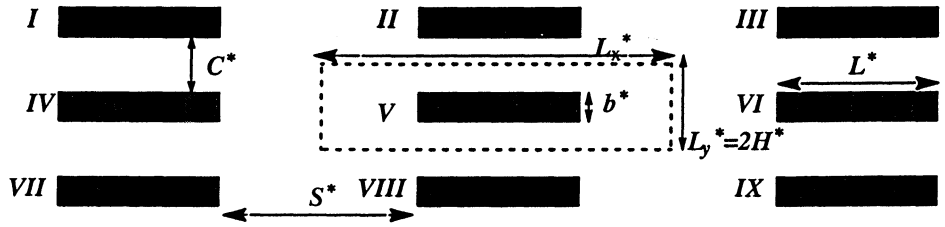

(a)

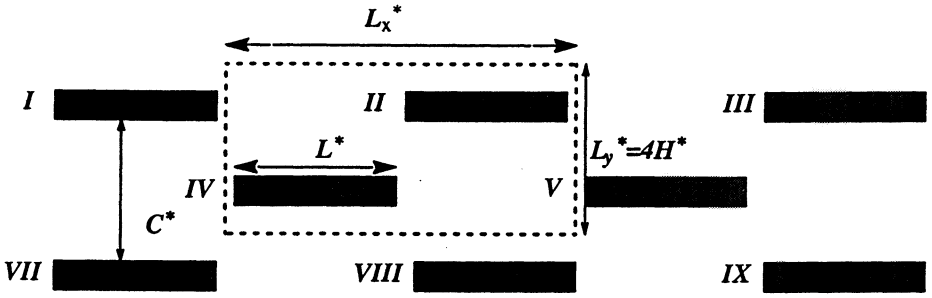

(b)

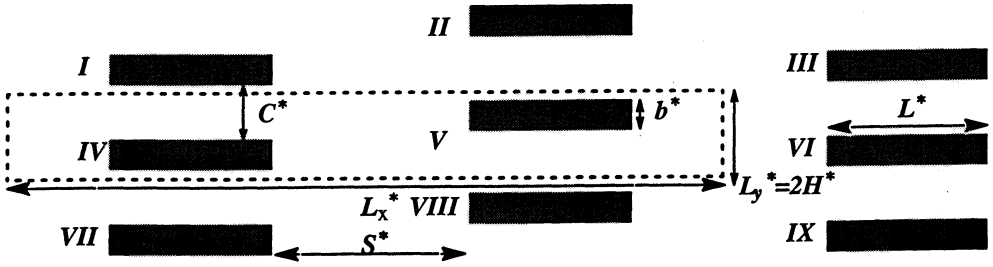

(c)

Figure 2.1 Schematic of parallel-plate fin arrangements studied along with computational domains: (a) inline; (b) staggered; (c) staggered-II.

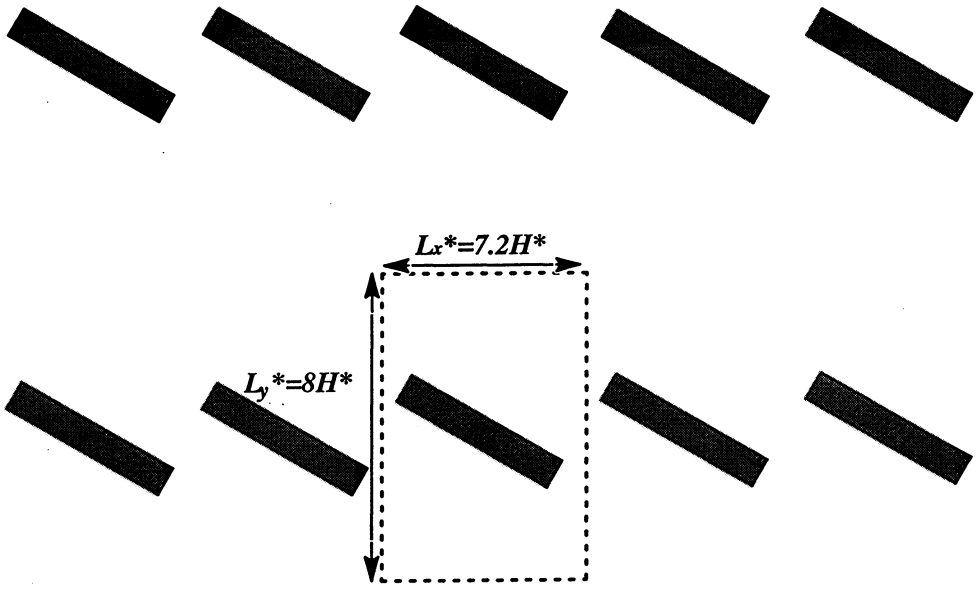

Figure 2.2 Schematic of louvered fin geometry currently simulated along with the computational domain.

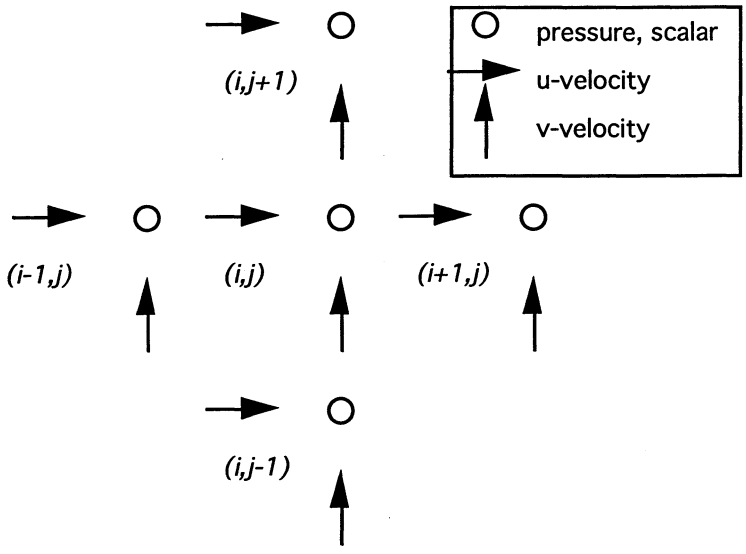

Figure 2.3 Schematic of staggered Cartesian grid used in parallel-plate fin simulations.

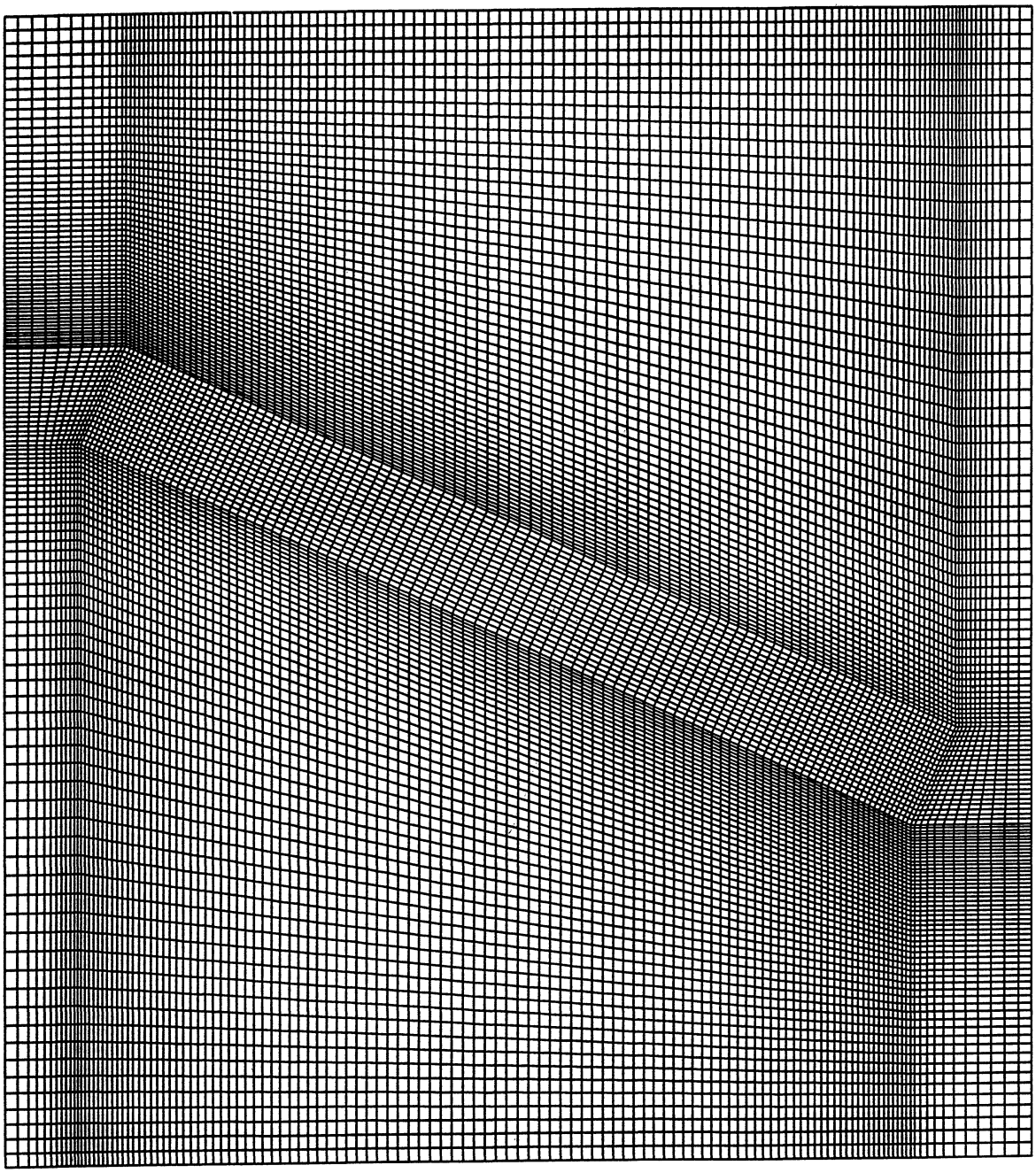

Figure 2.4 Schematic of non-staggered grid with body fitted coordinates, used in louvered fin simulations.

CHAPTER 3. CODE VALIDATION

In this chapter, some basic quantities will be defined first and then results of grid dependency studies will be shown along with a comparison to experimental data. Although the computations were performed with H^* and $(\Delta P^*/\varrho)^{1/2}$ as the length and velocity scales, in the results to be presented the Reynolds number, Re, is defined based on the hydraulic diameter $D_h^* = 4A_m^*/(\Omega_f^*/L_x^*)$, as $Re = V^*D_h^*/\nu$, where V^* is the dimensional mean velocity at minimum flow cross-section area A_m^*, and Ω_f^* is the heat transfer surface area. The Reynolds number defined here can be expressed in terms of nondimensional quantities as $Re = QL_zD_hRe_\tau/A_m$, where Q is the flow rate per unit spanwise width.

Instantaneous local heat transfer efficiency will be expressed in terms of the instantaneous local Nusselt number based on the hydraulic diameter, defined as

$$Nu(s^*,t^*) = \frac{[q''^*/(T_f^*(s^*,t^*) - T_{ref}^*(s^*,t^*))]D_h^*}{k} \tag{3.1}$$

where T_f^* and T_{ref}^* are the dimensional fin surface and local reference temperatures, respectively, and s^* measures the length along the periphery of the fin. The above equation can be rewritten in terms of nondimensional quantities as

$$Nu(s,t) = \frac{D_h}{\theta_f(s,t)-\theta_{ref}(s,t)} \tag{3.2}$$

where θ_f is the local nondimensional fin surface temperature and θ_{ref} is the reference nondimensional temperature defined as

$$\theta_{ref}(s,t) = \frac{\int_{-L_y/2}^{L_y/2}\int_0^{L_z}\theta|u|dzdy}{\int_{-L_y/2}^{L_y/2}\int_0^{L_z}|u|dzdy} \tag{3.3}$$

Here the absolute value of streamwise velocity is used so that regions with reverse flow are also properly represented [Patankar and Prakash (1981)]. Following Equation (3.1), the instantaneous global Nusselt number based on hydraulic diameter, $<Nu>$, is defined as the ratio of instantaneous total

flow rate from the fin surface through convection to that through conduction, and can be simplified in terms of nondimensional quantities as

$$< Nu > = \frac{\Omega_f D_h}{\int\int_{\partial D_{fin}} \left(\theta_f - \theta_{ref}\right) dS} \tag{3.4}$$

The overall Nusselt number, denoted by $\overline{<Nu>}$, is then defined as the average of the above over time. The time averaged local Nusselt number, $\overline{Nu}(s)$, is defined based on time averaged flow and thermal fields quantities such as $\overline{u}$ and $\overline{\theta}$ in Equations (3.2) and (3.3). In order to evaluate the overall performance of the system, a modified Colburn j factor is defined as

$$j = \frac{\overline{< Nu >}}{Re\, Pr^{0.4}} \tag{3.5}$$

where $n=0.4$ for developed flow [Sparrow and Hajiloo (1980)]. Friction factor, f, which measures the dimensionless pressure drop, is also defined here as

$$f = \frac{\Delta P_x^*}{\frac{1}{2}\rho V^{*2}} \left(\frac{D_h^*}{4L_x^*}\right) \tag{3.6}$$

where ΔP_x^* is the applied streamwise dimensional pressure drop across the computational domain. The above defined friction factor f can be expressed in terms of the nondimensional quantities as

$$f = \frac{D_h}{2} \frac{1}{(QW/A_m)^2} \tag{3.7}$$

Table 3.1 lists the geometrical parameters for all the cases studied for the inline arrangement and Table 3.2 lists that of the staggered arrangement. Case IL1 was considered to validate our calculation procedure with the experiments of Mullisen and Loehrke (1986). The geometries represented by Case IL2 and Case IL3 are of primary interest to the study of heat transfer enhancement mechanisms which will be discussed in great detail in Chapter 4. Case IL3 has the same geometric parameters as that of Case IL2, however, in this case the simulation is performed over only half the computational domain in the transverse direction and symmetry boundary conditions are applied along the fin and wake centerline. These simulations will be termed steady symmetrized simulations. Two kinds of staggered geometries are also studied which have exactly the same hydraulic diameter as that of Case IL2 and Case IL3, except that the fins have been placed in staggered patterns. Case SG1 and

Case SG2 (staggered-symmetrized) are obtained from the inline arrangement, IL2 and IL3 (inline-symmetrized), by shifting the alternate row of fins by half a wavelength, $L_x*/2$, in the x direction. The last case in staggered arrangement is Case SG3 which is obtained from the inline arrangement by shifting the alternate column of fins by a half wavelength, $L_y*/2$, in the transverse direction. The comparison of calculated flows between SG1 and SG3 shows the effect of fin arrangement. All calculations were performed by integrating the time-dependent Navier-Stokes and energy equations.

3.1 Parallel Performance

All computations of parallel-plate fin geometry are performed on the Connection Machine 5 (CM-5). The CM-5 at the National Center for Supercomputing Applications (NCSA) is a massively parallel computer architecture containing *512* processing nodes (each processor has four vector units) with *32* MBytes of memory for each node and a collective memory of *16* GBytes. This work was developed based on a general purpose computer program on the CM-5 in the data parallel paradigm [Tafti (1995a)] for the direct and large eddy simulations of turbulence. The computer program has several features ranging from second-order to high-order accurate finite-volume approximations, explicit/semi-implicit time advancement algorithms and an ability to handle a mix of boundary conditions with different solution techniques for the pressure equation. These features, benchmark solutions and validations of the flow solvers can be found in Tafti (1994, 1996a).

For flows with two homogeneous directions (e.g. turbulent channel flow calculations) the pressure Poisson equation is solved with 2-D FFT's in the homogeneous directions with a direct line solver in the inhomogeneous direction. Using this approach with a semi-implicit treatment of the momentum equations, execution speeds up to *8.8* GFlops per second have been obtained on *512* processing nodes with *24* million nodes in the calculation domain [Tafti (1996a)]. In the present study, the flow is inhomogeneous in both directions, and the method of Conjugate Gradients (CG) [Hestenes and Stiefel (1952)] is used to solve the pressure Poisson equation. The parallel implementation and performance of preconditioned CG and other Krylov subspace-based methods can be found in Tafti (1995b). In this chapter, the execution speeds for the grid sizes used in the present

parallel-plate fin geometry study will be shown along with the scalability of the computer program for large grid sizes, which would arise in large two- and three-dimensional calculations.

Figure 3.1 shows the typical performance for the two-dimensional grids used in the current work on a *32*-node partition of the CM-5. The MFlop/s rates are obtained by estimating the floating point operations in each module of the computer program. Typically, *97%* of the computational time is spent in solving the pressure equation, while the other *3%* is subsequently spent in solving the momentum and energy equations. It is found that the performance is a modest *100* MFlops/s at a resolution of *128x32*, but increases rapidly to *450* MFlops/s as the grid resolution increases to *512x256*. This is a result of increased vector lengths as the problem size increases with a fixed processor number and the resulting lower communication costs per floating point operation. Furthermore, Figure 3.2 shows the scalability of the computer program. As the grid size is varied from *512x256* on *32*-node partition to *1024x1024* on a *256*-node partition, a near perfect scalability is observed. Extrapolating this result to a *2048x1024* grid on a *512*-node CM-5 partition gives a performance of *7.0* GFlops per second, which clearly indicates the capability of the computer program to solve large scale heat transfer problems.

A typical unsteady simulation with a grid size of *128x32* cells requires about *0.3 ~ 0.4* second per time step on a *32*-node CM-5 partition, depending on the Reynolds number simulated. A typical computation in the time-dependent flow regime requires about *0.8 ~ 1.4* nondimensional time units for a shedding cycle. The typical nondimensional time step used in the present computations is of the order of *0.002*, corresponding to a CFL number of *0.3 ~ 0.5*. Thus about *2 ~ 5* minutes on a *32*-node partition are needed for a shedding cycle. The simulations are usually performed for more than *50* shedding cycles to ensure a stationary state be reached.

3.2 Grid Dependency Study

Grid dependency studies were performed for Case IL1 and Case IL2 at high Reynolds numbers to check the accuracy of the computer program and the resolution used in parallel-plate fin simulations. For Case IL1, the grid resolution was increased from *128*x*32* to *256*x*64* at $Re_\tau = 100$ ($Re \approx 2450$). It is found that by doubling the resolution in both directions, the j factor and friction factor

are reduced by *4%* and *5%*, respectively (see Table 3.3). Furthermore, for Case IL2 a similar resolution study at $Re_\tau = 70$ *(Re ≈ 2000)* also performed by increasing the number of grid points from *128*x*32* to *256*x*64* and *512*x*128* (see Table 3.4). By doubling the grid size in each direction to *256*x*64*, the friction factor *f* is reduced by about *9%* while the *j* factor is reduced by *6%*. Further doubling the grid to *512*x*128* cells resulted in a nominal reduction of *1%* and *2%* for the *f* factor and friction factor, respectively. In view of these results, it is expected that deviations occur between *5* to *10%* in the friction factor *f* and *j* factor reported on the *128x32* grid for $Re \geq 2000$ for the two-dimensional calculations in the simulation of flow and heat transfer in parallel-plate fins.

In the louvered fin simulations, at the Reynolds number of $Re_\tau = 10$ *(Re ≈ 1000)*, the grid size was increased from *128*x*64* to *128*x*128* to check the grid dependency of the solutions. It is observed that doubling the grid in the *y* direction resulting in a reduction of *j* factor by *6.5%* and an increase of friction factor by *2.3%* as shown in Table 3.5.

3.3 Comparison To Experimental Results

Table 3.6 summarizes the calculations performed for Reynolds numbers ranging from *165* to *3535* for Case IL1. The calculation domain was resolved with *128x32* finite difference cells in the *x* and *y* directions, respectively. In reporting their experimental results, Mullisen and Loehrke (1986) defined their hydraulic diameter based on the heat transfer length of the fins (*L* in Figure 2.1.) and the heat transfer area as based on only the top and bottom surface of the fin (*2L*xL_z in Figure 2.1.). Based on our definition of D_h and *f* (Equation (3.5)), we obtain the following scaling factors for D_h:

$$D_h = 1.846\, D_{h(ML)} \tag{3.8}$$

and for friction factor *f*:

$$f = 0.983\, f_{(ML)} \tag{3.9}$$

Here no scaling is needed for the Colburn *j* factor. Figure 3.3 compares the current computed *j* factor and friction factor to the experimental results of Mullisen and Loehrke (1986). Further, the results of Sparrow and Liu (1979) for an array of inline plates of infinitesimal thickness ($b = 0$), calculated for the current geometry are plotted. In their calculations, Sparrow and Liu (1979) assumed steady symmetric flow and solved the parabolic boundary layer equations. Because of these assumptions,

their j and friction factors do not include the effects of vortex shedding. In Figure 3.3, it is observed that the results of Sparrow and Liu (1979) agree well with the experiments and current calculations for $Re < 380$. However, there are substantial differences for $Re > 380$, due partly to the difference in geometry (finite fin thickness versus zero fin thickness), but more importantly due to the absence of vortex shedding in their simulations. On the other hand, it is found that the present time-dependent calculations show very good agreement with the experimental results up to $Re = 1300$, after which the present calculations overpredict the j factor and friction factor. The difference in the j factor appears larger than that of the friction factor f.

Here it should be cautioned that while our simulations employ a constant heat flux boundary condition on fin surfaces, Mullisen and Loehrke's experiments employed a constant temperature boundary condition. Furthermore, Mullisen and Loehrke directly measured only the inlet and outlet fluid temperature from which the j factor was computed iteratively by solving a one-dimensional energy equation for both the fin and the fluid. Additionally, while periodic boundary conditions are employed along the x and y directions in the present computations, Mullisen and Loehrke's experiments consisted of four fins along the streamwise direction and 26 fins along the transverse direction. Although 4 fins along the streamwise direction may appear not to be fully sufficient for establishing a fully developed flow, there is experimental evidence that the flow and thermal fields approach a fully developed state by the second fin along the streamwise direction [Sparrow and Hajiloo (1980)]. Thus, while the favorable comparison between the present simulations and the experimental results of Mullisen and Loehrke yields support for the present computational approach, the near perfect agreement at moderate Reynolds numbers maybe considered somewhat fortuitous. At high Reynolds numbers, $Re > 1300$, the difference between the present simulation results and those of Mullisen and Loehrke's experiments increases. This is mainly due to the effect of intrinsic three-dimensionality of the flow and will be discussed in detail in Chapter 5.

Comparison of results from the staggered arrangement (Case SG1) with experiments of DeJong and Jacobi (1996) and other correlations [Joshi and Webb (1987), Manglik and Bergles (1990)] are shown in Figure 3.4. In plotting the results from the correlations, the smallest aspect ratio, C/L_z, from

their original experimental data has been chosen in order to better approximate two-dimensionality. Reasonable comparison can be seen in both the heat transfer and frictional loss results.

Finally, Figure 3.5 compares current louvered fin results with the experimental data of DeJong (1996) and those of Zhang and Lang (1989). Here in order to facilitate comparison, all the quantities have been redefined based on the fin length instead of the hydraulic diameter as discussed in Chapter 6. The geometrical parameters of DeJong (1996) are approximately the same as those employed in the current calculations after proper nondimensionalization. Eight rows of fins are employed in the streamwise (x) direction while six columns of fins are employed in the transverse (y) direction in the test section of DeJong (1996), as shown in Figure 3.6. It is observed that the favorable comparison is achieved between current predictions and the data of DeJong (1996). The test arrays in the experiments of Zhang and Lang (1989) consist of five column plates in the transverse direction and the plate length of the two columns adjacent to the upper and lower walls is half of that of the three inner columns as shown in Figure 3.7. The heat transfer measurement is conducted only in the middle column. The j factor curve of Zhang and Lang (1989) in Figure 3.5(a) is obtained from their correlations for fully developed flow by substituting the currently simulated geometrical parameters, $L/L_p = 0.8$ and $\theta = 25°$, where L_p is the fin pitch which is equivalent to L_y in current simulations. It must be pointed out that while the constant heat flux boundary condition on fin surfaces is employed in the current simulations, the isothermal fin surface boundary condition is used in the experiments. In plotting the friction factor, since no correlation is available for the experiments of Zhang and Lang (1989), the closest geometrical parameters to that of current study have been chosen with $L/L_p = 0.75$ and $\theta = 25°$. Since the pressure drop measurement in Zhang and Lang (1989) is separate from the heat/mass transfer measurement, their measured pressure drop included wall friction and additional form drag from the fins embedded in the walls, which is suspected to have significantly contributed to the difference between the current calculated friction factor and the data of Zhang and Lang (1989).

Table 3.1: A list of inline geometry parameters.

Case	*b/L*	*S/L*	*C/L*	Flow
IL1	*0.09*	*1.0*	*0.11*	steady/unsteady
IL2	*0.12*	*1.25*	*0.20*	steady/unsteady
IL3	*0.12*	*1.25*	*0.20*	steady symmetrized

Table 3.2: A list of staggered geometry parameters.

Case	*b/L*	*S/L*	*C/L*	Flow
SG1	*0.12*	*0.25*	*0.51*	steady/unsteady
SG2	*0.12*	*0.25*	*0.51*	steady symmetrized
SG3	*0.12*	*1.25*	*0.20*	steady/unsteady

Table 3.3: Dependence of j and f on grid resolution for Case IL1 at $Re_\tau = 100$.

Grid Resolution	*j*	*f*
128x32	*0.0196*	*0.0614*
256x64	*0.0188*	*0.0587*

Table 3.4: Dependence of j and f on grid resolution for Case IL2 at $Re_\tau = 70$.

Grid Resolution	*j*	*f*
128x32	*0.0242*	*0.0841*
256x64	*0.0229*	*0.0764*
512x128	*0.0224*	*0.0755*

Table 3.5: Dependence of j and f on grid resolution for louvered fin simulation at $Re_\tau = 10$.

Grid Resolution	j	f
128x64	*0.0418*	*0.1417*
128x128	*0.0391*	*0.1450*

Table 3.6: Summary of calculations performed for inline Case IL1 (*128x32*).

Re_τ	Re_b	Re	j	f
15	*35*	*165*	*0.1076*	*0.2919*
20	*58*	*275*	*0.0664*	*0.1873*
25	*84*	*397*	*0.0482*	*0.1406*
30	*112*	*531*	*0.0379*	*0.1131*
40	*171*	*811*	*0.0283*	*0.0862*
50	*285*	*1086*	*0.0244*	*0.0750*
60	*338*	*1347*	*0.0226*	*0.0702*
80	*393*	*1859*	*0.0211*	*0.0655*
100	*507*	*2392*	*0.0196*	*0.0614*
100[1]	*519*	*2455*	*0.0188*	*0.0587*
100[2]	*518*	*2449*	*0.0161*	*0.0590*
140	*735*	*3474*	*0.0179*	*0.0575*
140[3]	*748*	*3535*	*0.0143*	*0.0555*

[1]two-dimensional simulation, grid size *256x64*

[2]three-dimensional simulation, grid size *256x64x64*

[3]three–dimensional simulation, grid size *128x32x64*

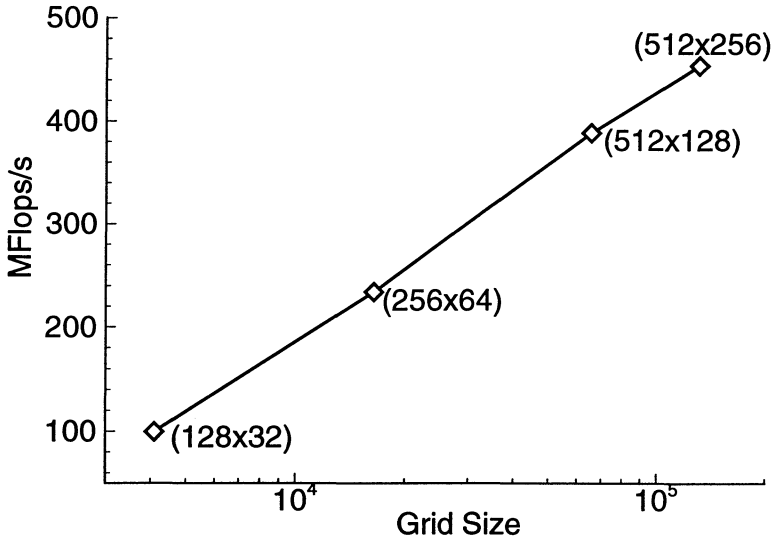

Figure 3.1 Parallel performance on a 32-node CM-5 partition with different grid sizes.

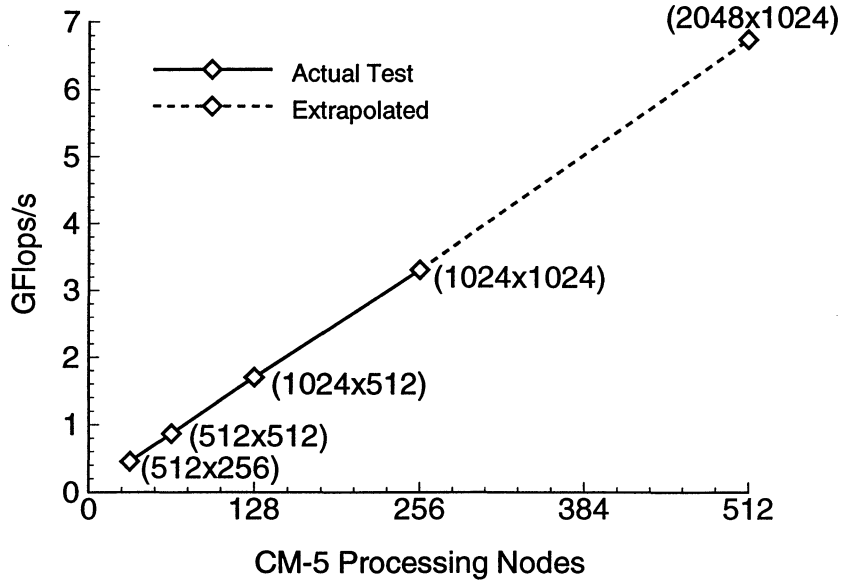

Figure 3.2 Scaled parallel performance on different CM-5 processing nodes.

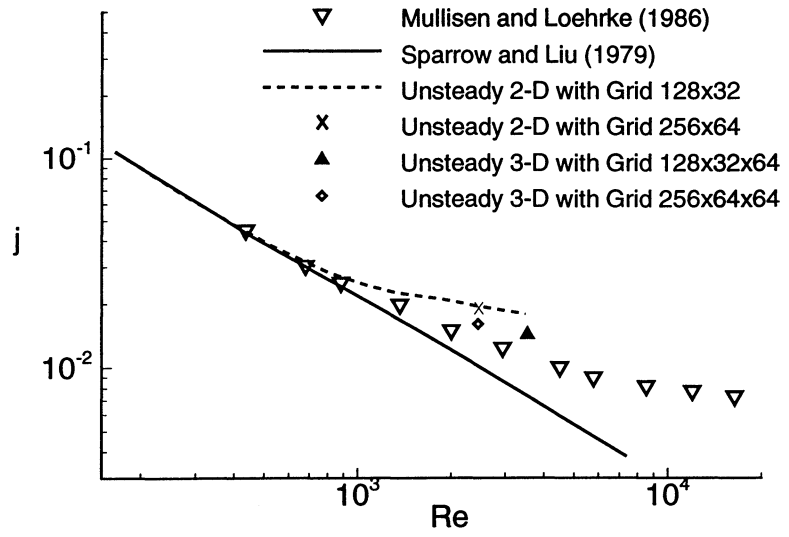

(a)

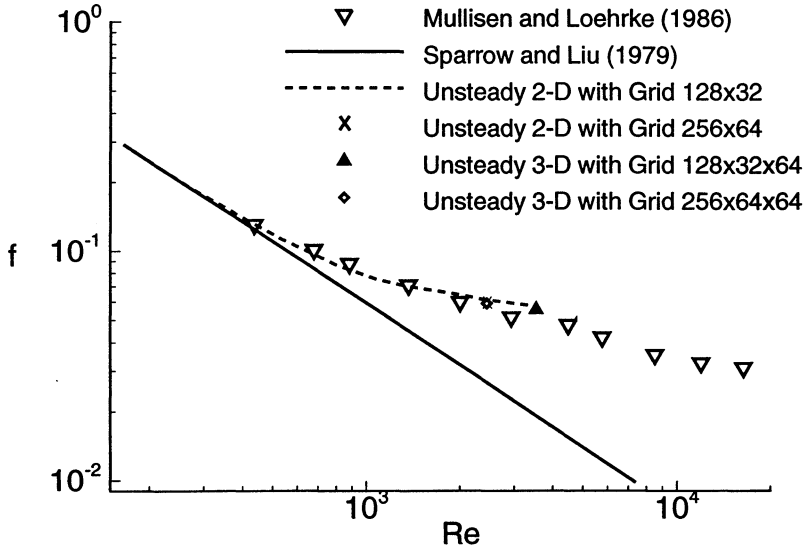

(b)

Figure 3.3 Comparison of current calculated inline overall performance data with existing experimental and numerical data: (a) *j* factor; (b) friction factor.

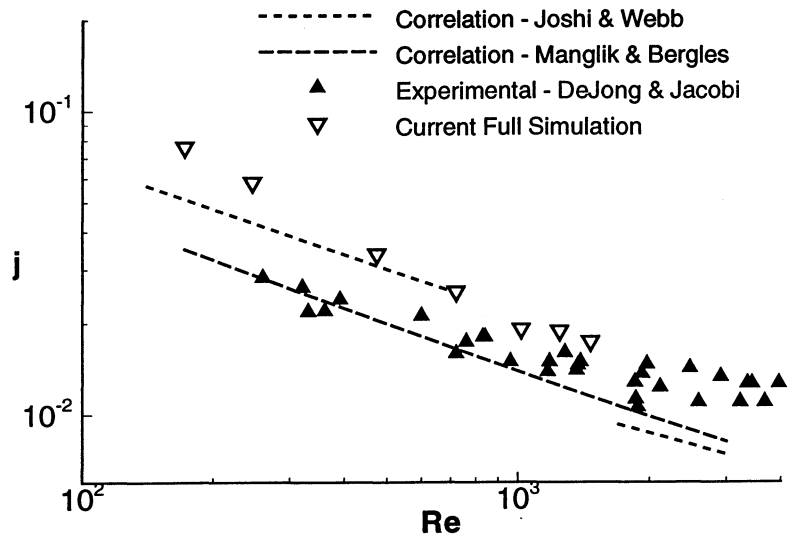

(a)

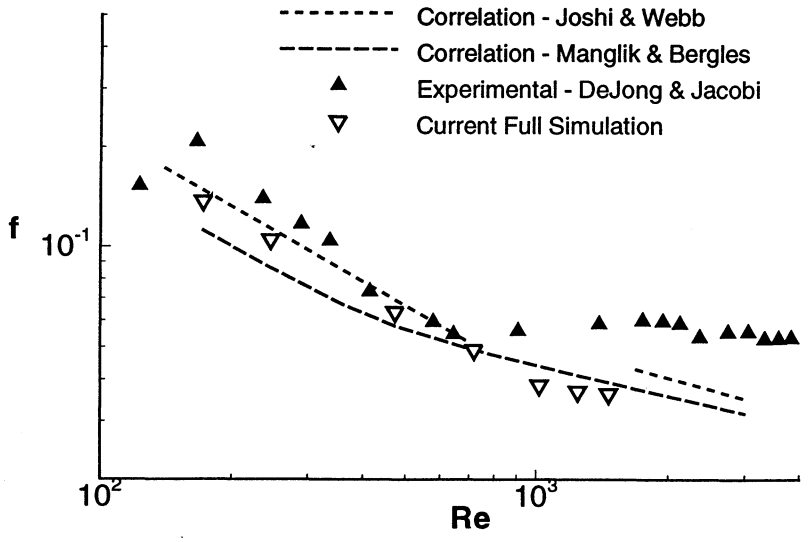

(b)

Figure 3.4 Comparison of current calculated staggered overall performance data with existing data: (a) *j* factor; (b) friction factor.

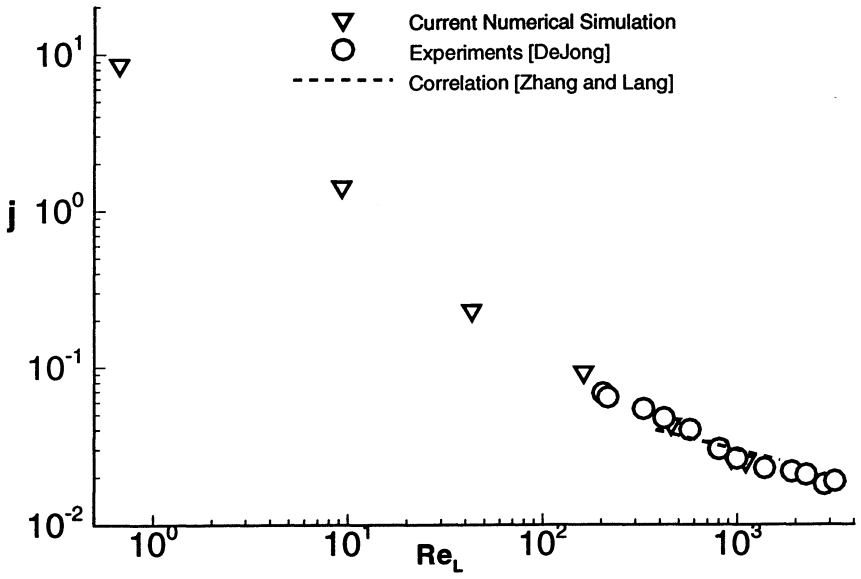

(a)

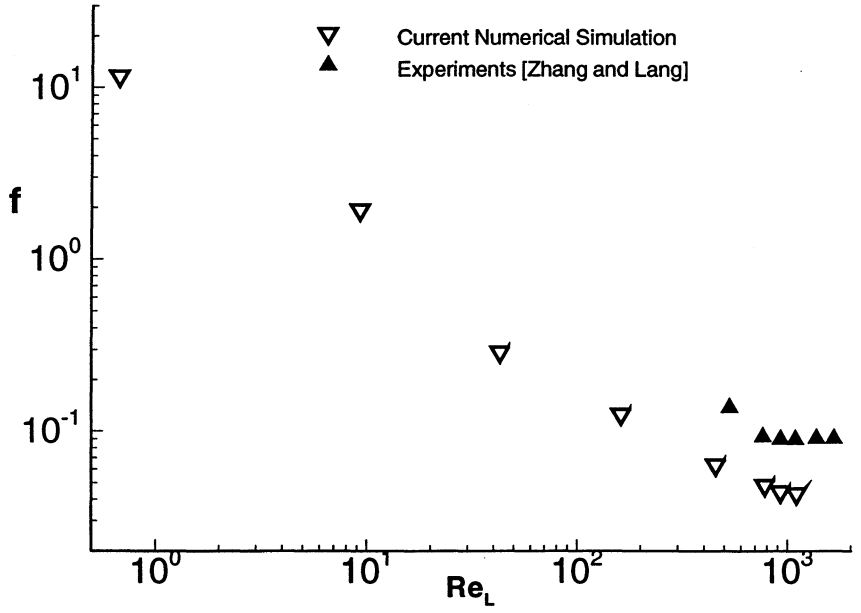

(b)

Figure 3.5 Comparison of current calculated louvered fin overall performance data with existing data: (a) *j* factor; (b) friction factor.

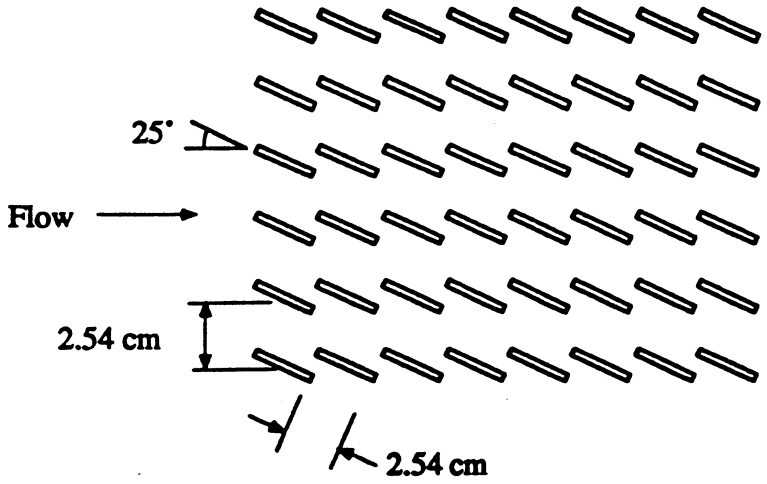

Figure 3.6 Schematic of the test array of louvered fin geometry of DeJong (1996)

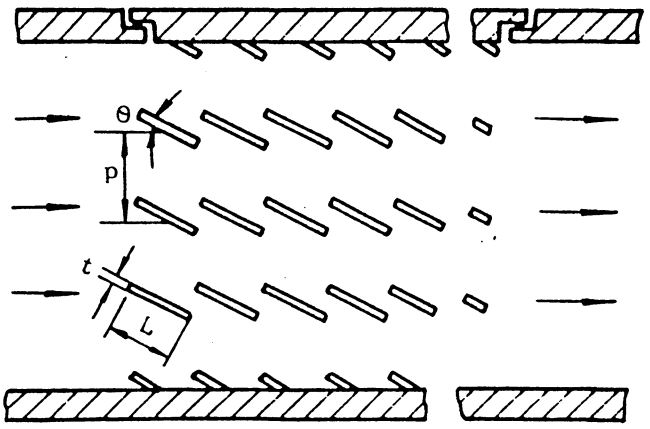

Figure 3.7 Schematic of the test array of louvered fin geometry Zhang and Lang (1989)

CHAPTER 4. HEAT TRANSFER ENHANCEMENT MECHANISMS IN PARALLEL-PLATE FIN HEAT EXCHANGERS

In this chapter, the heat transfer enhancement mechanisms and the performance of parallel-plate fin heat exchangers are studied. Geometry effects such as finite fin thickness and fin arrangements are also investigated. The time-dependent flow behavior due to vortex shedding has been taken into consideration by solving the unsteady Navier-Stokes and energy equations. In the unsteady flow regime, in addition to the full time-dependent calculations, companion steady symmetrized flow calculations have also been performed to clearly identify the effect of vortex shedding on heat transfer and friction loss. Additional comparisons have been made to theoretical results for fully developed flow between uninterrupted continuous parallel plates and those of restarted boundary layers with negligible fin thickness, in order to quantify the role of the boundary layer restart mechanism as well as the effect of finite fin thickness and fin arrangement. One inline arrangement (Case IL2 and Case IL3 as shown in Figure 2.1(a)) and a corresponding staggered arrangement (Case SG1 and Case SG2 as shown in Figure 2.1(b)) are considered in detail. The heat transfer surface area per unit volume is maintained the same for the two geometries. In the inline arrangement shown in Figure 2.1(a) the minimum flow cross-sectional area is chosen to be $(2H^*-b^*)L_z^*$ and the heat transfer surface area is $2(b^*+L^*)L_z^*$, while in the staggered arrangement shown in Figure 2.1(b) the minimum flow cross-sectional area is chosen to be $(4H^*-2b^*)L_z^*$ and the heat transfer surface area is $4(b^*+L^*)L_z^*$, where L_z^* is the width of the fin in the spanwise, z, direction, taken to be unity in the present two-dimensional simulations. Thus for both the inline and staggered geometries used in the present computations the hydraulic diameter is given by $5.026H^*$. In order to facilitate comparison, Case IL1 is referred to as unsteady inline, Case IL2 is referred to as symmetrized inline, Case SG1 is referred to as unsteady staggered and Case SG2 is referred to as symmetrized staggered. Any reference to other cases will be explicitly stated.

The various transitions undergone by the flow as the Reynolds number is increased are shown first. Figures 4.1, 4.2, 4.3 and 4.4 show the flow pattern and the corresponding time variation of the instantaneous global Nusselt number for the staggered geometry (Case SG1) at four different

Reynolds numbers: $Re = 246, 720, 1245$ and 1465, respectively. The constancy of $<Nu>$ shown in Figure 4.1 indicates that the flow is steady laminar at $Re = 246$. The recirculating bubble seen in the wake is observed to grow in size with increasing Reynolds number in the steady flow regime. The flow becomes unsteady at a critical Reynolds number somewhere between 474 and 720, which is consistent with the theoretical prediction of $Re_{crit} = 688$ for this geometry by Joshi and Webb (1987). Above this critical Reynolds number a time periodic state is obtained as can be inferred from the asymmetric state of the wake bubble and the small amplitude waviness of the wake at $Re = 720$ as shown in Figure 4.2. At this Reynolds number the time trace of the instantaneous global Nusselt number shows that the flow oscillates at a single frequency, with a Strouhal number $St = 0.15$, where $St = F^*b^*/V^*$ and F^* is the primary dimensional frequency of oscillation. As Reynolds number further increases, the flow undergoes another instability as can be seen from the appearance of a strong secondary low frequency in the time history of Nusselt number at $Re = 1245$ as shown in Figure 4.3. At this Reynolds number the Strouhal number of the primary frequency increases to 0.17 and the secondary low frequency is approximately one fifth of the primary shedding frequency. Also can be seen is the appearance of well defined vortices that roll on the top and bottom surfaces of the fin. With further increase in Reynolds number the flow soon becomes chaotic as shown by the flow field and the time history of Nusselt number at $Re = 1465$ in Figure 4.4.

The flow in the inline arrangement follows a similar qualitative pattern, although the transition Reynolds number for the appearance of the various flow regimes quantitatively differs from those of the staggered arrangement. In the unsteady inline simulations (Case IL2), the flow was found to be steady at $Re = 245$ with a recirculation bubble behind the trailing edge of the fin. At the next higher Reynolds number of $Re = 381$, periodic vortex shedding was observed to occur with a Strouhal number of 0.14. Above this, up to a Reynolds number of about 2000, the flow is observed to be unsteady with a single shedding frequency. The appearance of an additional frequency and subsequent transitions to a chaotic state are delayed to higher Reynolds numbers compared with that in staggered arrangement. Figure 4.5(a) and Figure 4.5(b) show the time history of the velocity v at $x = 0, y = 0$ for flow at a Reynolds number of 1407 after reaching a stationary state and the corresponding frequency spectrum, which clearly indicates a dominant nondimensional primary frequen-

cy F of *1.2* corresponding to a Strouhal number of *0.16*. Figure 4.5(c) and Figure 4.5(d) show the corresponding time history and frequency spectrum for the Nusselt number signal, and it is observed that the dominant frequency of *2.4* is exactly twice that of the velocity signal. Figures 4.6(a-d) show similar plots at Reynolds number of *2191*. At this higher Reynolds number the Strouhal number further increases to *0.17* and the frequency spectrum shows a lot more activity with the presence of low frequency oscillations in the Nusselt number signal.

The Strouhal numbers for the staggered and inline arrangements are listed in Tables 4.1 and 4.2, respectively. In both cases, the Strouhal number, *St*, can be seen to be nearly a constant over a range of Reynolds numbers and jumps to a higher value at higher Reynolds numbers. Okajima (1982) observed similar phenomena in his experiments on the vortex shedding frequencies of various rectangular cylinders placed in a uniform flow. For the relatively high ratio of $L^*/b^* = 4$ employed in his experiments, Strouhal number is almost independent of Reynolds numbers and has a value of *0.14*. Furthermore it is observed in the inline arrangement as shown in Table 4.2 that there is a jump in Strouhal number near the Reynolds number of *1400* and by analyzing the Fourier transform of the velocity field along the streamwise direction, it is confirmed that this jump is due to a discrete change in the number of waves observed along the streamwise direction. For the inline geometry, over the range of lower Reynolds numbers four waves were observed over a length of L_x and above a Reynolds number of *1400* five waves were observed. But the impact of the number of discretized waves on both global and local j factor and friction factor f at any given Reynolds number was not observed to be strong.

It must be pointed out that the flow and thermal fields in the unsteady flow regime are qualitatively similar in both the inline and staggered arrangements. For example, Figure 4.7(a) shows the instantaneous temperature contours for the staggered arrangement at $Re = 1465$ and the corresponding velocity vector field can be seen in Figure 4.4. Figures 4.7(b-c) show the flow and thermal fields for the inline arrangement at a comparable Reynolds number of *1407*. From these figures it is clear that in both these arrangements there are vortices that roll on the top and bottom surfaces of the fin which significantly alter the local thermal field and thereby the local heat transfer. These vortices rotate clockwise on the top surface and rotate counter-clockwise on the bottom surface. They act

as large scale mixers and bring in fluid from the freestream on their downstream side towards the fin surface and eject the fluid on their upstream side away from the fin surface. This can be seen to result in the crowding of the temperature contours near the fin surface. The oscillatory nature of the flow manifests itself in the wake of the fin elements as wavy motion that propagates in the streamwise direction over time.

4.1 Global Results

In Figure 4.8 the Colburn j factor and the friction factor are plotted against the Reynolds number on a log-log scale for the arrangement. Here the objective is to compare these results with those of Sparrow and Liu (1979) and those for continuous parallel plates to isolate contributions to heat transfer and friction factor from the individual mechanisms. In order to make a fair comparison and proper estimation of the individual effects it is important to follow a uniform scaling of all the results. The theoretical results for the continuous flat plate, shown in Figure 4.8 as the solid line, are based on a fully developed laminar flow and thermal fields between two infinitely long parallel plates with separation $4H^*$. This separation was chosen in order to maintain the heat transfer surface area per unit volume to be the same as in the inline or staggered arrangement. From Figure 2.1(b), this corresponds to continuous parallel plates formed by offsetting every other column of fins and then connecting the fins, but with zero fin thickness.

The Nusselt number and the friction factor, based on the half channel height, for a fully developed flow between parallel plates with constant heat flux are $35/17$ and $1.5/Re$, respectively. In Equation (3.1), the Nusselt number for the inline and staggered arrangements has been defined as the ratio of actual heat transfer to corresponding conductive heat transfer with the hydraulic diameter as the length scale. Similarly in Equation (3.6) the friction factor represents the nondimensional friction loss over a streamwise length of D_h^*. For proper comparison, the j factor and friction factor along with the Reynolds number must be defined with a single common length scale. Here we choose $D_h^* = 5.026H^*$, the hydraulic diameter of the inline and staggered arrangements as the common length scale (Sparrow and Liu (1979) used the hydraulic diameter of the continuous parallel plates as the common length scale). This scaling results in a factor of $D_h/2$ and $D_h^2/4$ for the j factor

and friction factor for the continuous parallel plate results. One then obtains the following j factor and friction factor f relations:

$$j = 6.0\,\mathrm{Re}^{-1} \quad \text{and} \quad f = 9.4\,\mathrm{Re}^{-1} \quad \text{[Continuous Parallel Plates]} \tag{4.1}$$

where Re is the Reynolds number for the parallel plates based on the hydraulic diameter of $D_h^* = 5.026H^*$. In the limit of flow between the continuous parallel plates, boundary layer restart and vortex shedding mechanisms are absent. Furthermore, the geometry effects arising from the finite fin thickness and the placement of the fin elements are absent as well. These three effects together account for the substantial increase in the computed j factor and friction factor f for the parallel-plate fins over the continuous parallel plate results.

Also plotted as the dashed line in Figures 4.8(a-b) are the results obtained by Sparrow and Liu (1979) for the staggered arrangement. Once again, in order to maintain the heat transfer area the same, the dimensional transverse spacing between adjacent fins is maintained $C^* = 4H^*$ and the dimensional fin length is half the computational domain ($L_x{}^*/2$), similar to the staggered arrangement except with negligible fin thickness. In their model the above two are the only parameters needed since it was assumed that the fins are infinitesimally thin and the resulting flow is considered to be steady. Their results on the j factor and friction factor f are again converted with $D_h^* = 5.026H^*$ as the length scale and fit by a power law of the form:

$$j = 4.19\,\mathrm{Re}^{-0.80} \quad \text{and} \quad f = 6.83\,\mathrm{Re}^{-0.82} \quad \text{[Sparrow and Liu, Staggered]} \tag{4.2}$$

The difference between the continuous parallel plate and Sparrow and Liu's results accounts for only the effect of periodic restarting of the hydrodynamic and thermal boundary layers. It is clear that the effect of the boundary layer restart mechanism is to increase overall heat transfer but with the associated penalty of higher friction loss.

It is still difficult to fully assess the importance of self-sustained flow oscillations because the difference between the present simulation results and those of Sparrow and Liu (1979) also have contribution from the geometry effect, mainly arising from the finite thickness of the fin. In order to further isolate and separate these mechanisms, simulations were conducted in the same staggered arrangement shown in Figure 2.1(b), but with appropriate symmetry imposed about the wake centerline. This symmetrization of the flow removes all asymmetry in the wake associated with the vortex

shedding process and thus the flow is constrained to follow the steady solution. We shall call these symmetrized simulations as "steady symmetrized simulations". The computed results of the steady symmetrized simulation for the staggered arrangement are listed in Table 4.3. It can be seen that the steady symmetrized simulation also follows a power law behavior best fit by

$$j = 6.0\,\mathrm{Re}^{-0.84} \quad \text{and} \quad f = 6.2\,\mathrm{Re}^{-0.74} \quad \text{[Steady Symmetrized, Staggered]} \tag{4.3}$$

Differences in the j factor and friction factor of the steady symmetrized simulations and those of Sparrow and Liu (1979) account for the finite thickness of the fin elements and the resulting steady wake bubble.

The finite thickness of the fin does seem to affect the overall heat transfer behavior a little, primarily due to the fact that the finite fin thickness decreases the transverse spacing available for the flow, C^*, from $4H^*$ to $4H^*–b^*$. For the parameters listed in Table A.2, this corresponds to a change of *18.75%* in the transverse spacing, C^*. If this change in transverse spacing is accounted for, then the difference between the j factor of the steady symmetrized simulations and those of Sparrow and Liu (1979) is negligible. This suggests that the other effects of finite fin thickness, such as those due to the wake bubble, can be ignored in heat transfer considerations, at least over the Reynolds number range considered here. Similarly, the decrease in transverse spacing available for the flow in the case of finite fin thickness accounts for most of the increase in the friction factor f in the steady symmetrized simulations over the results of Sparrow and Liu (1979). Even with this change in transverse spacing accounted for, a noticeable increase in the friction factor can be observed. This increase can be attributed to the contribution to friction factor arising from the form drag, in the case of finite fin thickness.

The effect of flow unsteadiness can be illustrated by comparing the unsteady simulations and the steady symmetrized simulations in the inline arrangement. At low Reynolds numbers, the results from unsteady simulations are identical to those from steady symmetrized simulations in the steady flow regime and follow the power law behavior. But above the critical Reynolds number, once the flow becomes time-dependent, the unsteady simulation results show systematic deviation from the power law curve of the steady symmetrized simulations with significant increase in both the j factor and friction factor f as shown in Figure 4.8. These critical Reynolds numbers are estimated to be

approximately *350* for the inline arrangement and *650* for the staggered arrangement. Differences in the performance of the steady symmetrized and the unsteady simulations are solely due to the effect of flow unsteadiness. These differences are well evident when comparing the time-averaged mean streamlines and temperature contours. Figure 4.9(a) show the time-averaged streamlines obtained from the unsteady inline simulation at $Re = 797$, and Figure 4.9(b) shows that for the steady symmetrized simulation at approximately the same Reynolds number ($Re = 804$). The corresponding temperature contours are shown in Figure 4.10. Similar plots for the mean streamlines and temperature profiles at a higher Reynolds number of approximately *1400* are shown in Figure 4.11 and Figure 4.12, respectively. At lower Reynolds numbers when the actual flow is steady, the mean streamline pattern and temperature profiles from both full and steady symmetrized simulations are in perfect agreement. However, as the Reynolds number increases to the unsteady flow regime, there are large differences in the mean flow patterns. For the steady symmetrized cases, the recirculation zone behind the fin increases with the Reynolds number while the unsteady simulations show a decreasing and much smaller recirculation zone due to the increased mixing as the Reynolds number increases. Correspondingly, there are large differences in the mean temperature profiles. These differences introduce large errors in the prediction of j and f and thus, clearly illustrate the importance of accounting for flow unsteadiness at higher Reynolds numbers.

Figure 4.13 shows the global results for the inline fin arrangement. Here again a comparison of the j factor and friction factor from the continuous parallel plate theory, simulations of Sparrow and Liu (1979) for inline plates of infinitesimal thickness, steady symmetrized simulations and the full unsteady simulations help to separate the individual contributions from the boundary layer restart, finite geometry and self-sustained oscillatory effects. The results of Sparrow and Liu (1979) and steady symmetrized simulations (listed in Table 4.4) can be fit by the following power laws:

$$j = 6.06\,\mathrm{Re}^{-0.84} \quad \text{and} \quad f = 12.73\,\mathrm{Re}^{-0.89} \qquad \text{[Sparrow and Liu, Inline]} \tag{4.4}$$

$$j = 10.5\,\mathrm{Re}^{-0.88} \quad \text{and} \quad f = 22.5\,\mathrm{Re}^{-0.82} \qquad \text{[Steady Symmetrized, Inline]} \tag{4.5}$$

The general trend seems to fit the description provided for the staggered arrangement. But there are some differences. Mainly, the geometry effect given by the difference between the steady symmetrized simulations and the results of Sparrow and Liu (1979) appears larger than the staggered coun-

terpart. This is because, in the inline geometry the effect of finite fin thickness in decreasing the transverse gap available for the flow, C^*, from $2H^*$ to $2H^*-b^*$ accounts for a *37.5%* reduction in the flow cross-section. Whereas, in the staggered arrangement the reduction in flow cross-section is only *18.75%*. This decrease in the flow cross-section almost entirely accounts for the increase in the j factor, but the friction factor is further increased by the presence of form drag in the case of finite fin thickness. Furthermore, in both the inline and staggered arrangements, the fully developed boundary layer results can be seen to slowly diverge from the other two power laws with increasing Reynolds number. This effect is more visible in the friction factor f. This is possibly due to the fact that at lower Reynolds numbers the flow between the adjacent plates in the transverse direction rapidly develops into a fully developed flow, whereas as the Reynolds number increases the entrance length for flow and thermal development also increases, thus increasing the deviation from a fully developed flow. This hypothesis will be confirmed later with a careful look at the hydrodynamic and thermal boundary layers.

A comparison of the two arrangements for the same Reynolds number based on hydraulic diameter, shows that the inline arrangement results in a higher heat transfer accompanied by higher friction loss than the staggered arrangement as shown in Figure 4.14. The higher heat transfer enhancement in the inline arrangement is caused by the smaller transverse spacing, C^*, which results in thinner boundary layers than those in the staggered arrangement. The smaller boundary layers are also associated with higher skin friction resulting in a higher friction factor in the inline arrangement. Furthermore, it is observed that the inline geometry and the second staggered geometry, staggered-II (results listed in Table 4.5), have about the same performance, which suggests that each row of fins in the streamwise direction has little impact on the flow and heat transfer of the following row of fins, provided that they are separated by some sufficient length, S. This result seems to hold over the entire Reynolds number range investigated.

4.2 Local Nusselt Number Distribution

In the following, the role of vortices in enhancing the local heat transfer will be closely examined. Figure 4.15 shows the velocity vector field in the inline arrangement at $Re = 797$ at two

different time instances and their corresponding instantaneous local Nusselt number distribution along the fin periphery. These two instances are separated by *0.5* nondimensional time units, which corresponds to *0.45* shedding period. At the first time instance shown in Figure 4.15(a) a counter-clockwise vortex can be clearly seen to be located on the bottom left hand side of the fin. Over time this vortex travels down the fin surface and at the later time instance shown in Figure 4.15(b) it has significantly lost its strength and can be barely located at approximately $x = 7$ on the bottom surface. In the meantime a clockwise vortex has been shed off the front top leading edge of the fin and can be seen to be located at $x = 5$. In fact, the imprint of an earlier clockwise vortex can be seen in Figure 4.15(a) at $x = 8$ as the inrush of fluid toward the fin. Also marked in this figure are the fin surface locators starting from the top left corner (marked **A** in Figure 4.15(b)) going around the clockwise direction (marked **B, C, D** in Figure 4.15(b)) and back to the top left corner of the fin. These shed vortices act as large-scale mixers by entraining freestream fluid around their downstream periphery and ejecting it upstream similar to the phenomena observed in flow over a blunt flat plate by Tafti (1991a).

The local Nusselt number is significantly higher at the leading edge due to the stagnating nature of the flow, while it is significantly lower in the wake owing to the local recirculation. Enhancement of the local Nusselt number can be well correlated with the presence of the clockwise and counter-clockwise vortices pointed out earlier. For example, the counter-clockwise vortex seen in Figure 4.15(a) at $x = 5$ can be seen to generate a strong local peak in the Nusselt number at $s = 12.2$. At the later instance, this vortex has moved downstream to $s = 8.2$ and its impact on local Nusselt number has decreased. Similarly the clockwise vortex on the top surface of the fin can be also related to a local peak in the Nusselt number variation and it can be inferred that the vortices can increase the local Nusselt number by as much as *50%*. Also plotted in Figure 4.15(c) are the time-averaged local Nusselt number, $\overline{Nu}(s)$, for the unsteady simulation and the local Nusselt number obtained from the corresponding steady symmetrized simulation at approximately the same Reynolds number ($Re = 804$). In the case of the steady symmetrized solution, the monotonic decrease in the Nusselt number away from the front leading edge is solely due to the growth in the thermal boundary layer. In the case of time-dependent simulations, significant improvement in local heat transfer can be at-

tributed to the presence of vortices. The vortices can be seen to adversely affect the local Nusselt number on their upstream end where fluid is pushed away from the fin surface and result in a local decrease in the Nusselt number below the steady symmetrized simulation result. On the other hand, an increase in the local Nusselt number is realized at the downstream side of the vortex where fluid is brought to the fin surface, which more than compensates for the decrease at the other upstream end. The net effect is to increase heat transfer over the entire fin surface in the time-dependent flow regime. The rapid fall in the local Nusselt number in the unsteady simulations is both due to the growth of the thermal boundary layer and due to the decrease in the strength of the vortices.

Figure 4.16 shows the time-averaged Nusselt number distribution on the top (or bottom) surface of the fin for many different Reynolds numbers for both arrangements. For the inline arrangement, at lower Reynolds numbers below *700*, the Nusselt number distribution can be seen to decay to an asymptotic value of *16.56*. This asymptotic value is the theoretical Nusselt number corresponding to a hydrodynamically and thermally fully developed flow between parallel plates of separation $C^* = 2H^* - b^*$ (see Figure 2.1(a)) with isoflux boundary conditions, converted appropriately for the present hydraulic diameter of the inline arrangement. Thus, it can be seen that at the lowest Reynolds number considered ($Re = 120$) the thermal boundary layer grows to within *1%* of the fully developed thermal boundary layer profile within ($s < 2.1$) the first *33%* of the fin surface. As the Reynolds number increases, the Nusselt number at the leading edge grows and increasingly departs from the asymptotic value. Accordingly, the length of the thermal entrance region also increases and eventually grows beyond the length of the fin. Therefore, at higher Reynolds numbers the Nusselt number even at the trailing edge is appreciably greater than *16.56*. At higher Reynolds numbers in the time-dependent flow regime, the Nusselt number distribution does not exhibit a simple decay as it does at lower Reynolds numbers. A change in the Nusselt number distribution due to the strong influence of the leading edge vortices on the upstream portion of the fin surface can be clearly seen. Although the general behavior in the staggered arrangement can be inferred to be qualitatively the same as that of the inline arrangement, there are a number of differences which warrant further comment. At the lower Reynolds numbers when the flow is steady, the local Nusselt number can be seen to approach an asymptotic value of *6.37*, which corresponds to the theoretical Nusselt number for a hydrodynam-

ically and thermally fully developed flow between parallel plates of separation $C^* = 4H^* - b^*$ (see Figure 2.1(b)) with isoflux boundary conditions, converted appropriately for the present hydraulic diameter definition of the staggered arrangement. This asymptotic value of fully developed Nusselt number is only *38.5%* of that of the inline arrangement, since the transverse spacing between the fin elements in the inline arrangement is proportionately smaller than for the staggered arrangement. But unlike the inline arrangement, the approach to this asymptotic value is not complete by the trailing edge even at the lowest Reynolds number. This is due to the fact that the velocity and temperature profiles at the leading edge are quite distorted and strongly influenced by the upstream fin elements in the staggered arrangement (see Figure 4.17(b)). This effect can also be seen in the significantly higher local Nusselt number near the leading edge of the fin. As the Reynolds number increases, interestingly the local Nusselt number at the leading edge decreases due to the effect of the wake of the upstream fin elements. Whereas, away from the leading edge over most of the fin surface, the local Nusselt number increases with an increasing Reynolds number, owing to the action of unsteady vortices. Just as in the inline geometry, systematic deviations from a simple exponential decay can be observed at the higher Reynolds numbers due to contribution from strong vortices.

The time-averaged nondimensional temperature difference, $\overline{\theta} - \overline{\theta}_f$, profiles as a function of distance away from the fin surface, $\tilde{y}$, are plotted in Figure 4.17 at different Reynolds numbers for both arrangements. In the inline arrangement, results for the unsymmetrized full simulations *Re = 120, 797* and *2191* are plotted at three different locations on the fin surface: at the leading edge, middle of the top (or bottom) surface of the fin and at the trailing edge of the fin, so that the development of the profile can be clearly observed. Also plotted at a Reynolds number close to *797* are the corresponding temperature difference profiles for the steady symmetrized simulation at *Re = 804*. In the present simulations, since the heat flux at the fin surface is held fixed, the nondimensional temperature gradient at the fin boundary ($\tilde{y}$=*0*) always remains the same equal to unity (see Equation (2.13)). Therefore, from the Nusselt number definition given in Equation (3.1), it can be seen that the larger the deviation of the free stream temperature from the local fin surface temperature, the lower will the corresponding time-averaged local Nusselt number. The lower freestream temperature at *Re* =

120 indicates a corresponding lower *Nu*. At this lowest Reynolds number the temperature profile quickly develops into a fully developed thermal profile and very little difference exists between the thermal profiles at the middle point of the fin and at the trailing edge. At the intermediate Reynolds number, the time-averaged thermal profile slowly develops until the trailing edge of the fin. On the other hand, at $Re = 2191$ the time-averaged thermal profiles indicate a rapid decrease in the time-averaged local Nusselt number from the leading edge to the mid-point of the fin, but a small increase in $\overline{Nu}(s)$ towards the trailing edge. These results are consistent with the time-averaged local Nusselt number distributions shown in Figure 4.16(a).

Comparing the $\overline{\theta} - \overline{\theta}_f$ profiles at $Re = 797$ with those of the corresponding steady symmetrized simulation at $Re = 804$, the effect of vortices on increasing the time-averaged fluid temperature to approach the fin surface temperature can be seen over the entire fin length. This effect can be seen to somewhat decrease towards the trailing edge, possibly due to the weakening of the vortices as they travel downstream. Furthermore, the steady symmetrized solution suggests that even in the absence of vortex shedding, the thermal profile is not fully developed by the trailing edge at higher Reynolds numbers. This result is in full agreement with theoretical results that the entrance length increases with Reynolds number in the laminar regime [White (1974)].

Figure 4.17(b) shows similar plots for the staggered arrangement for three different Reynolds numbers, $Re = 172, 720$ and 1465. Also plotted at the highest Reynolds number are the corresponding temperature difference profiles for the steady symmetrized simulation at approximately the same Reynolds number ($Re = 1451$). All these profiles are plotted over only half the domain in the transverse, y, direction and the profile over the other half can be obtained by symmetry. It can be clearly seen that even at the lowest Reynolds number the temperature profile does not develop into a fully developed thermal profile by the trailing edge. At the leading edge, the influence of the wake of the upstream fin element appears as the significant temperature reversal away from the fin surface. This reversal is particularly strong at the lowest Reynolds number, since the size of the thermal wake is larger at lower Reynolds numbers, as can be observed from the trailing edge profiles. This results in a significantly reduced difference between the fin surface and mixed mean fluid temperature and explains the higher local Nusselt number near the leading edge at lower Reynolds numbers.

Comparing the $\overline{\theta} - \overline{\theta}_f$ profiles at $Re = 1465$ with those of the corresponding steady symmetrized simulation at $Re = 1451$, it can be observed that the effect of time-dependent vortices is to bring the fluid temperature closer to the fin surface temperature over the entire fin length.

4.3 Local Skin Friction Distribution

In this section the effect of vortex shedding on the friction factor will be investigated. In the case of fins with finite thickness, the friction factor derives contributions both from the skin friction on the top and bottom surfaces of the fin and from the form drag due to the pressure difference between the front and back surfaces of the fin. In Table 4.1 and Table 4.2, the total friction factor, percentile contribution to friction factor from skin friction and percentile contribution from form drag are listed for the inline and staggered arrangements, respectively. In both geometries the percentile contribution from skin friction steadily decreases with increasing Reynolds numbers, while the form drag becomes increasingly important. This result is in agreement with our common knowledge of bluff body wakes. Among the two arrangements, the form drag is relatively more important in the staggered arrangement than in the inline arrangement. This again is consistent with our expectation that the percentile contribution from form drag should be lower in the inline arrangement since geometrically each fin is sheltered by the wake of the upstream fin array. It is important to note that, while at lower Reynolds numbers there is near equal partition between the skin friction and form drag contributions, at higher Reynolds number the form drag contribution is a factor of four or more greater than the skin friction contribution.

Figure 4.18 investigates the effect of the vortices that roll on the top and bottom surfaces of the fin on the local skin friction factor. Here the local skin friction factor is defined as

$$C_f = \frac{\mu}{H^*}\left[\frac{\partial u^*}{\partial y^*}\right]_{wall} \frac{D_h^*}{2\,\rho\,V^{*2}} \tag{4.6}$$

consistent with the overall friction factor defined in Equation (3.6) which includes the contribution from form drag as well. The local skin friction factor on the top surface of the fin at $Re = 797$ for the inline arrangement is plotted in Figure 4.18 at two different time instances shown in Figures 4.15(a-b). The corresponding local Nusselt number results were presented earlier in Figure 4.15(c).

It can be clearly seen by comparing the C_f distribution with the vortex seen near the leading edge in Figure 4.15(b), that the effect of the vortex for the most part is to decrease the local skin friction. In fact, due to the local reversed flow induced by the vortex a negative skin friction, corresponding to a negative drag force, can be seen. The weaker local maximum and minimum around $s = 0.8$ and $s = 0.4$ suggest the presence of smaller counter-rotating eddies (which are not large enough to be fully visible in Figure 4.15(b)) at the heel of the larger clockwise-rotating vortex. Downstream of the vortex, the skin friction factor quickly becomes positive and approaches a near constant value of about *0.08*. The effect of the vortices can also be seen as the local minimum at $s = 3.1$ in the local skin friction factor distribution at the earlier time corresponding to Figure 4.15(a), but the drop in C_f is not as dramatic due to the rapid decay of the vortices as they travel downstream.

Also plotted in this figure are the time-averaged local skin friction factor, $\overline{C_f}(s)$, for the unsteady simulation and the local skin friction factor obtained from the corresponding steady symmetrized simulation at $Re = 804$. A comparison of the instantaneous distributions to the time averaged distribution clearly illustrates the strong effect of the vortices in decreasing local C_f by as much as *64%* near the leading edge. Of course, this effect significantly weakens downstream. The decrease in the local skin friction factor obtained in the time-dependent simulation over the corresponding steady state simulations can be attributed to the presence of vortices. Thus, the effect of the vortex on skin friction can be seen to be just the opposite of its effect on local Nusselt number. Although the above results are for the inline arrangement, an investigation of the staggered arrangement shows similar strong local reduction in the skin friction factor due to the vortices.

Figure 4.19 shows the time-averaged local skin friction for all the Reynolds numbers of both arrangements. For the inline arrangement, at the lowest Reynolds number of *120*, the skin friction factor can be seen to decay to an asymptotic value of about *0.505*. This asymptotic value is in full agreement with the theoretical friction factor of $60.63/Re$ corresponding to a fully developed parabolic flow between parallel plates of separation $C^* = 2H^* - b^*$, converted appropriately for the present hydraulic diameter definition. Thus it can be seen that the boundary layer grows very rapidly to the fully developed profile. At slightly higher Reynolds numbers, the effect of the finite fin thickness can be seen as the undershoot very close to the leading edge in the approach to the asymptotic

value. Furthermore, the approach to the asymptotic value appears very rapid and not strongly dependent on the Reynolds number. This appears to be in contradiction to the theoretical prediction that the entrance length for the development of the hydrodynamic boundary layer in a channel increases linearly with Reynolds number [White (1974)]. But it will soon be noted that the velocity profile even at the leading edge is close to a parabolic profile and significantly different from a plug flow assumed in the theory. The rapid increase in the friction factor close to the trailing edge is due to the sudden expansion of the flow downstream of the trailing edge.

Figure 4.19(b) shows the corresponding time-averaged $C_f(s)$ for the staggered arrangement. The behavior of the skin friction factor appears to be similar to that of the inline arrangement except for two noticeable differences. First, at lower Reynolds numbers the friction factor now decay to a lower asymptotic value given by *17.94/Re,* which corresponds to the theoretical value for a fully developed parabolic velocity profile between parallel plates of separation $C^*=4H^*-b^*$, converted appropriately for the present hydraulic diameter definition. Second, at Reynolds numbers greater than *720*, the time-averaged skin friction factor is negative near the leading edge indicating the presence of a separated flow region in the time-averaged mean flow. Such a reversed flow region was absent in the time-averaged mean flows of the inline arrangement. This indicates a stronger influence of the vortices in the staggered arrangement. The length on the mean reversed flow region can be seen to increase with *Re* and the increase is rapid at lower Reynolds number. The difference between these profiles is very small at higher Reynolds numbers, which suggests the possibility of a self similar time-averaged C_f distribution independent of Reynolds number. Such approach to self similarity can also be observed for the inline arrangement.

The time-averaged streamwise velocity profiles as a function of distance away from the fin surface, $\tilde{y}$, are plotted in Figure 4.20 for both arrangements at different Reynolds numbers, *Re = 120, 797* and *2191*. At each Reynolds number, the results for the unsymmetrized full simulations are plotted at three different locations on the fin surface: at the leading edge, middle of the top (or bottom) surface of the fin and at the trailing edge of the fin, so that the downstream development of the hydrodynamic boundary layer can be followed. Also plotted at a Reynolds number close to *797* (*Re = 804*) are the corresponding $\bar{u}$ profiles for the steady symmetrized simulation. As pointed out earli-

er, the approaching velocity profile at the leading edge is so close to the final fully developed parabolic velocity profile that the hydrodynamic entrance length is small. Comparison of the velocity profiles at $Re = 797$ with those of the corresponding steady symmetrized simulation at $Re = 804$ is not straightforward. Since the overall friction factor for the unsteady simulation is larger, the corresponding time-averaged flow rate is *8.5%* smaller than that of the steady symmetrized flow (note that in the present simulations the nondimensional pressure drop is held fixed equal to unity in all the simulations). Thus part of the decreased local skin friction factor in the unsymmetrized simulation over the steady symmetrized simulation observed in Figure 4.18 is due to this decreased time-averaged flow rate. This difference in flow rate is sufficient to account for the difference at the midpoint of the fin and further downstream, whereas the larger difference close to the leading edge is clearly due to the action of the vortices. While the unsteady flow phenomenon at higher Reynolds numbers is thus seen to decrease the skin friction contribution, its effect on form drag is just the opposite. The form drag increases with flow oscillation and more than compensates for the decrease in skin friction and thereby the overall friction factor is increased over the steady symmetrized simulation.

Similar plots for the staggered arrangement at three different Reynolds numbers: $Re = 172, 720$ and 1465 are shown in Figure 4.20(b). Also plotted are the corresponding streamwise velocity profiles for the steady symmetrized simulation at $Re = 1451$. All these profiles are plotted over only half the domain in the transverse, y, direction. At the leading edge, the wake of the upstream fin element appears to strongly influence the velocity profile. A sharp decrease in the streamwise velocity at $\tilde{y} = 1.625$ (midway between the adjacent fin elements) accounts for the significant departure from a parabolic profile. This decrease in the local velocity near the centerline somewhat increases the maximum velocity in order to conserve flow rate and, furthermore, the location of the maximum velocity moves closer to the fin surface ($\tilde{y} \approx 0.4$). This results in a significantly increased velocity gradient at the fin surface and explains the higher local skin friction coefficient near the leading edge. It can be clearly seen that even at the lowest Reynolds number, the velocity profile does not develop into a fully developed parabolic profile by the trailing edge. Comparing the velocity profiles at $Re = 1465$ with those of the corresponding steady symmetrized simulation at $Re = 1451$, it can be ob-

served that due to the increased overall friction factor the unsteady simulations result in a *15%* smaller time-averaged flow rate than the steady symmetrized simulations. The lower flow rate contributes to a lower skin friction coefficient in the case of the unsteady simulations, and more importantly the effect of the vortices in the unsteady regime is to further decrease the skin friction contribution. But, as seen in the inline arrangement, the effect of time-dependent flow oscillation is to significantly increase the form drag and more than compensate for the decrease in the skin friction contribution.

Table 4.1: A List of Shedding Frequency (*St*), *j* Factor, Friction Factor (*f*), Percentile Contribution to Friction Factor from Skin Friction and Form Drag at Different Reynolds Numbers for the Staggered Arrangement with fully unsteady simulation.

Re_τ	Re_b	*Re*	*St*	*j*	*f*	**Skin Friction Contribution**	**Form Drag Contribution**
8	*26*	*172*	Steady	*0.0761*	*0.1373*	*54.3%*	*45.7%*
10	*37*	*246*	Steady	*0.0582*	*0.1049*	*50.6%*	*49.4%*
15	*71*	*474*	Steady	*0.0338*	*0.0634*	*42.8%*	*57.2%*
20	*107*	*720*	*0.15*	*0.0253*	*0.0490*	*32.8%*	*67.2%*
25	*152*	*1018*	*0.16*	*0.0191*	*0.0383*	*24.5%*	*75.5%*
30	*186*	*1246*	*0.17*	*0.0188*	*0.0368*	*16.6%*	*83.4%*
35	*219*	*1465*	*0.17*	*0.0174*	*0.0362*	*13.2%*	*86.8%*

Table 4.2: A list of nondimensional shedding frequency (*St*), *j* factor, friction factor (*f*), percentile contribution to friction factor from skin friction and form drag at different Reynolds numbers for the inline arrangement with full unsteady simulation.

Re_τ	Re_b	*Re*	*St*	*j*	*f*	**Skin Friction Contribution**	**Form Drag Contribution**
10	*18*	*120*	Steady	*0.1655*	*0.4427*	*62.5%*	*37.5%*
15	*37*	*245*	Steady	*0.0843*	*0.2385*	*57.5%*	*42.5%*
20	*57*	*381*	*0.14*	*0.0577*	*0.1747*	*50.3%*	*49.7%*
25	*82*	*546*	*0.14*	*0.0436*	*0.1330*	*45.8%*	*54.2%*
30	*105*	*706*	*0.14*	*0.0363*	*0.1147*	*39.3%*	*60.7%*
32.5	*119*	*797*	*0.14*	*0.0332*	*0.1056*	*36.9%*	*63.1%*
35	*134*	*899*	*0.14*	*0.0305*	*0.0962*	*35.6%*	*64.4%*
40	*168*	*1128*	*0.14*	*0.0267*	*0.0799*	*34.4%*	*65.6%*
50	*210*	*1407*	*0.16*	*0.0260*	*0.0802*	*28.4%*	*71.6%*
60	*249*	*1669*	*0.16*	*0.0250*	*0.0820*	*23.1%*	*76.9%*
70	*287*	*1923*	*0.17*	*0.0242*	*0.0841*	*21.4%*	*78.6%*
80	*328*	*2191*	*0.17*	*0.0233*	*0.0846*	*19.0%*	*81.0%*

Table 4.3: Summary of calculations performed for staggered steady symmetrized (Case SG2, *256x32* grid cells).

Re_τ	Re_b	Re	j	f
8	*26*	*172*	*0.0752*	*0.1373*
10	*37*	*246*	*0.0575*	*0.1049*
15	*71*	*474*	*0.0334*	*0.0637*
20	*113*	*754*	*0.0221*	*0.0446*
25	*161*	*1080*	*0.0159*	*0.0340*
30	*217*	*1451*	*0.0120*	*0.0271*

Table 4.4: Summary of calculations performed for inline steady symmetized simulations (Case IL3, *128x16* grid cells)

Re_τ	Re_b	Re	j	f
10	*17*	*117*	*0.1692*	*0.4669*
15	*36*	*240*	*0.0856*	*0.2489*
20	*59*	*392*	*0.0549*	*0.1653*
25	*86*	*573*	*0.0394*	*0.1208*
30	*117*	*784*	*0.0300*	*0.0929*
30[1]	*120*	*804*	*0.0291*	*0.0884*
35	*153*	*1025*	*0.0238*	*0.0740*
40	*194*	*1298*	*0.0194*	*0.0603*
42[1]	*218*	*1458*	*0.0173*	*0.0527*
50	*289*	*1938*	*0.0137*	*0.0423*
60	*405*	*2710*	*0.0103*	*0.0311*

[1]grid size *128x64*

Table 4.5: Summary of calculations performed for staggered-II (Case SG3) with full unsteady simulation (*256x64* grid cells).

Re_τ	Re_b	Re	j	f
13	*28*	*189*	*0.1078*	*0.3005*
15	*36*	*239*	*0.0861*	*0.2495*
20	*56*	*374*	*0.0585*	*0.1819*
25	*83*	*553*	*0.0421*	*0.1297*
30	*110*	*734*	*0.0351*	*0.1060*
40	*152*	*1018*	*0.0299*	*0.0980*
50	*209*	*1398*	*0.0259*	*0.0812*

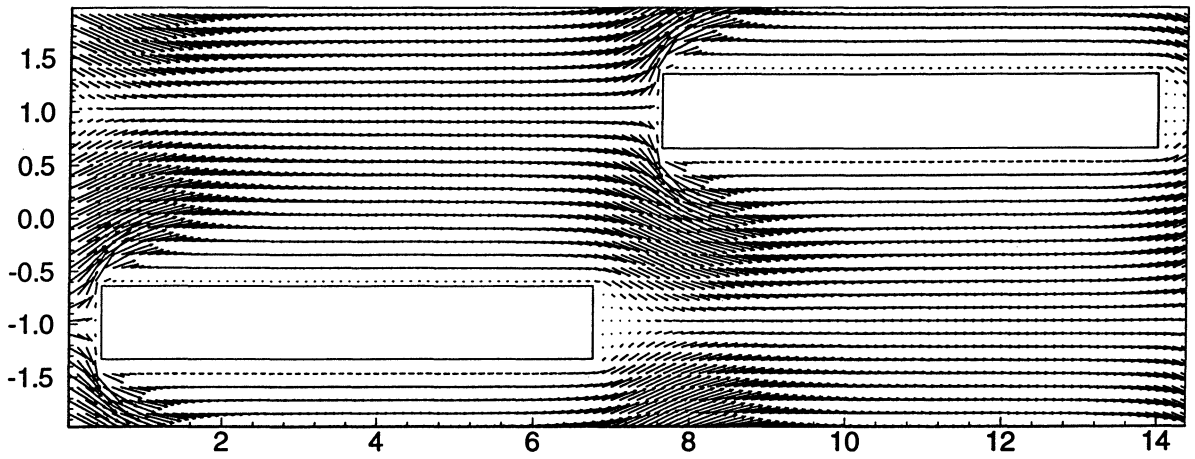

(a)

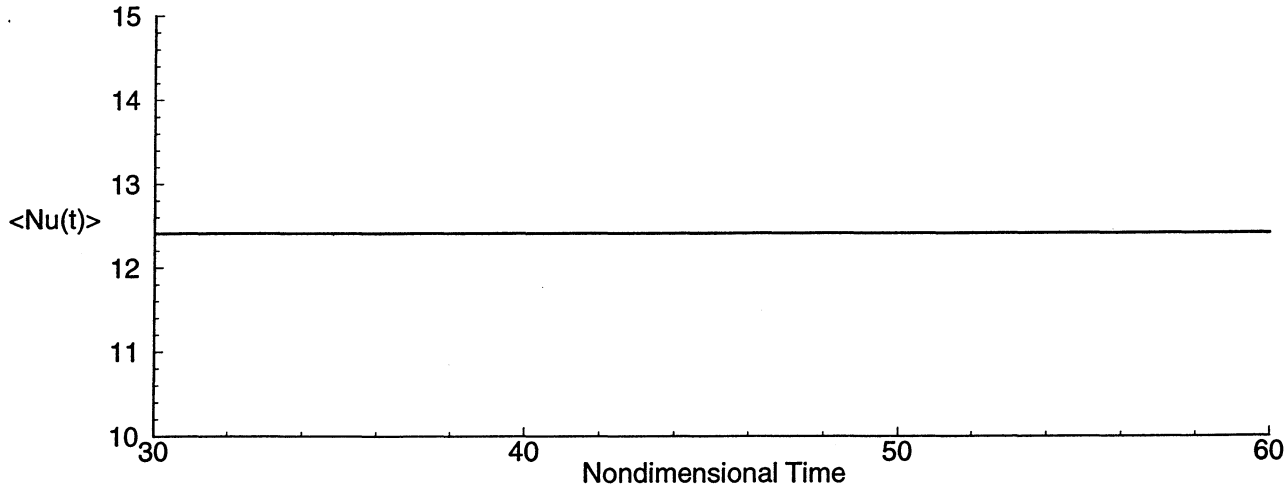

(b)

Figure 4.1 (a) Vector plot of velocity field; (b) time trace of instantaneous global Nusselt number for the staggered arrangement at *Re = 246*; the flow is steady.

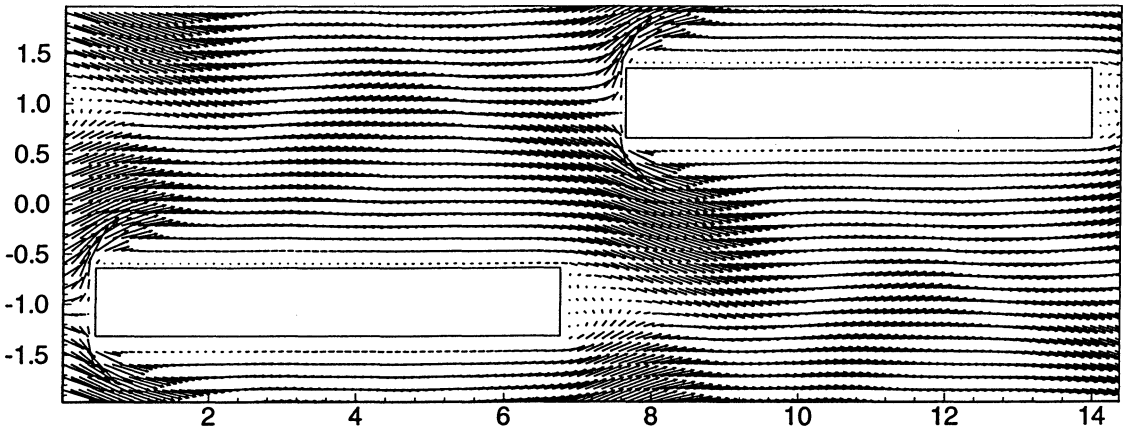

(a)

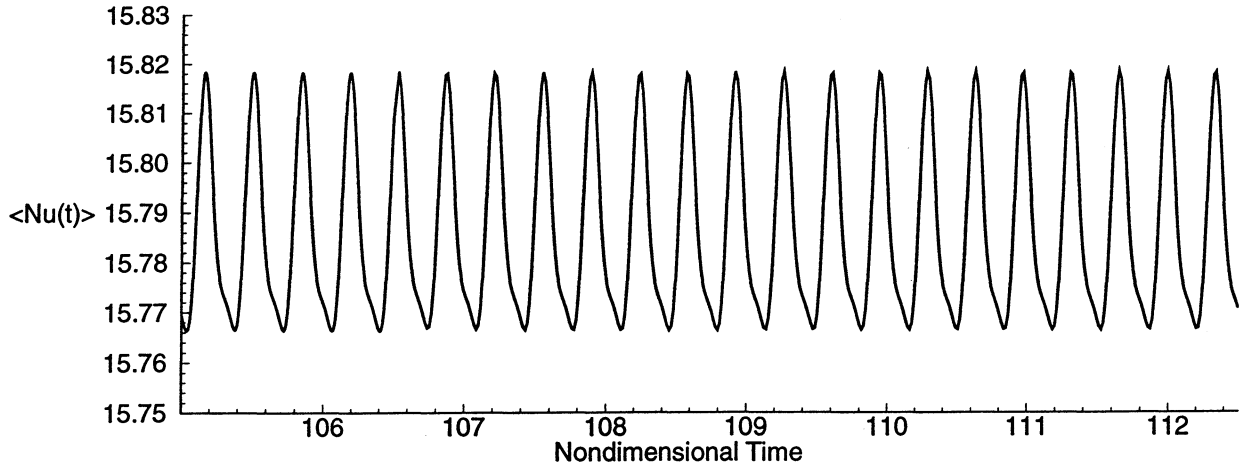

(b)

Figure 4.2 (a) Vector plot of velocity field; (b) time trace of instantaneous global Nusselt number for the staggered arrangement at $Re = 720$; the flow oscillates at a single frequency with a Strouhal number of 0.15.

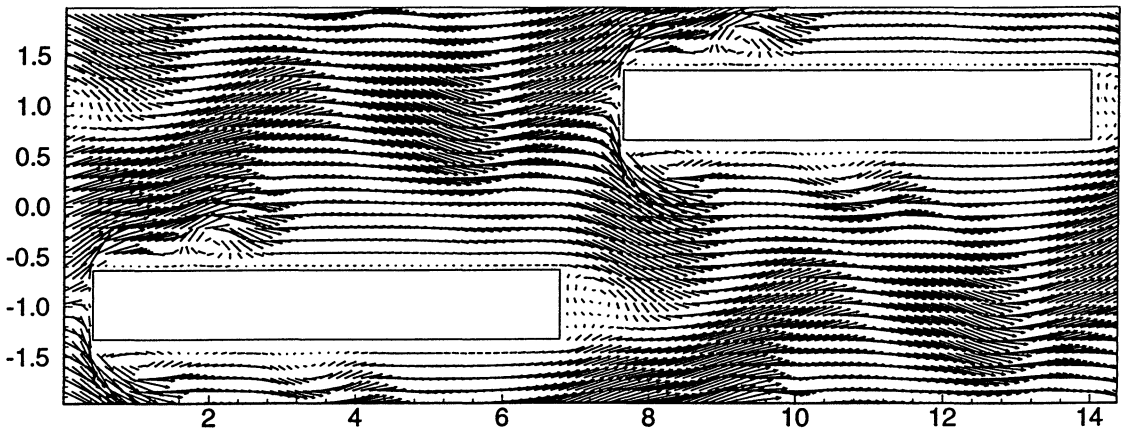

(a)

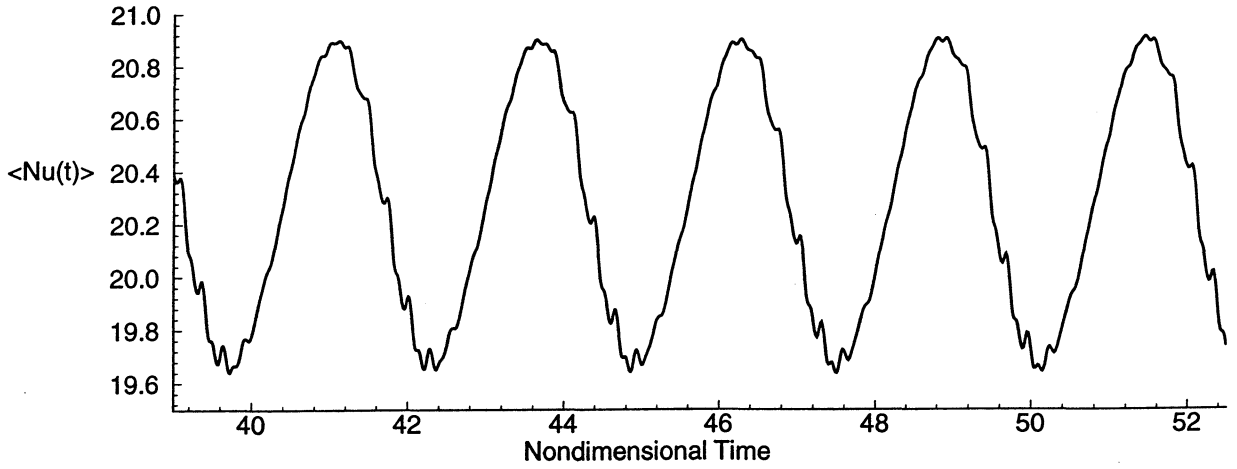

(b)

Figure 4.3 (a) Vector plot of velocity field; (b) time trace of instantaneous global Nusselt number for the staggered arrangement at *Re=1245*; the Strouhal number of the primary frequency is *0.17*, a secondary low frequency can also be observed.

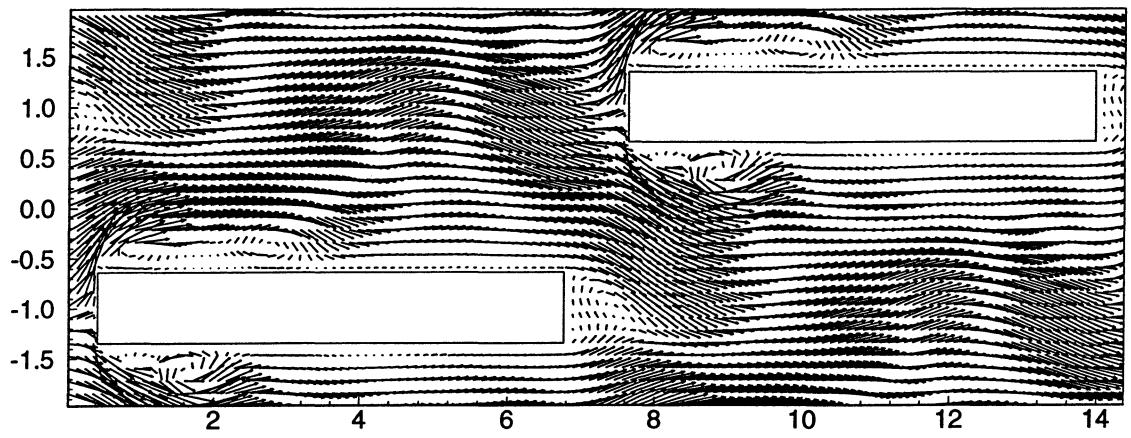

(a)

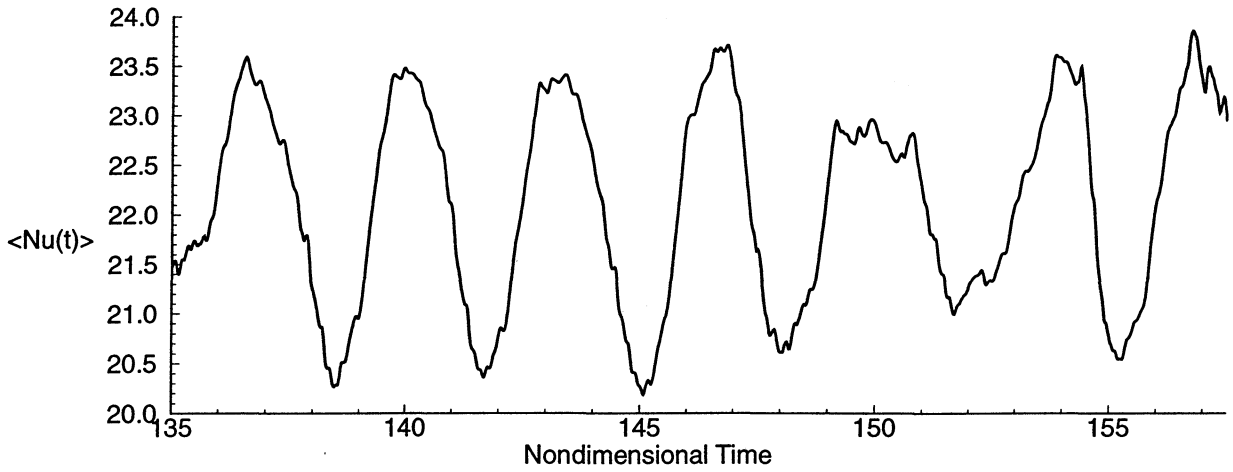

(b)

Figure 4.4 (a) Vector plot of velocity field; (b) time trace of instantaneous global Nusselt number for the staggered arrangement at *Re = 1465*; the flow is chaotic.

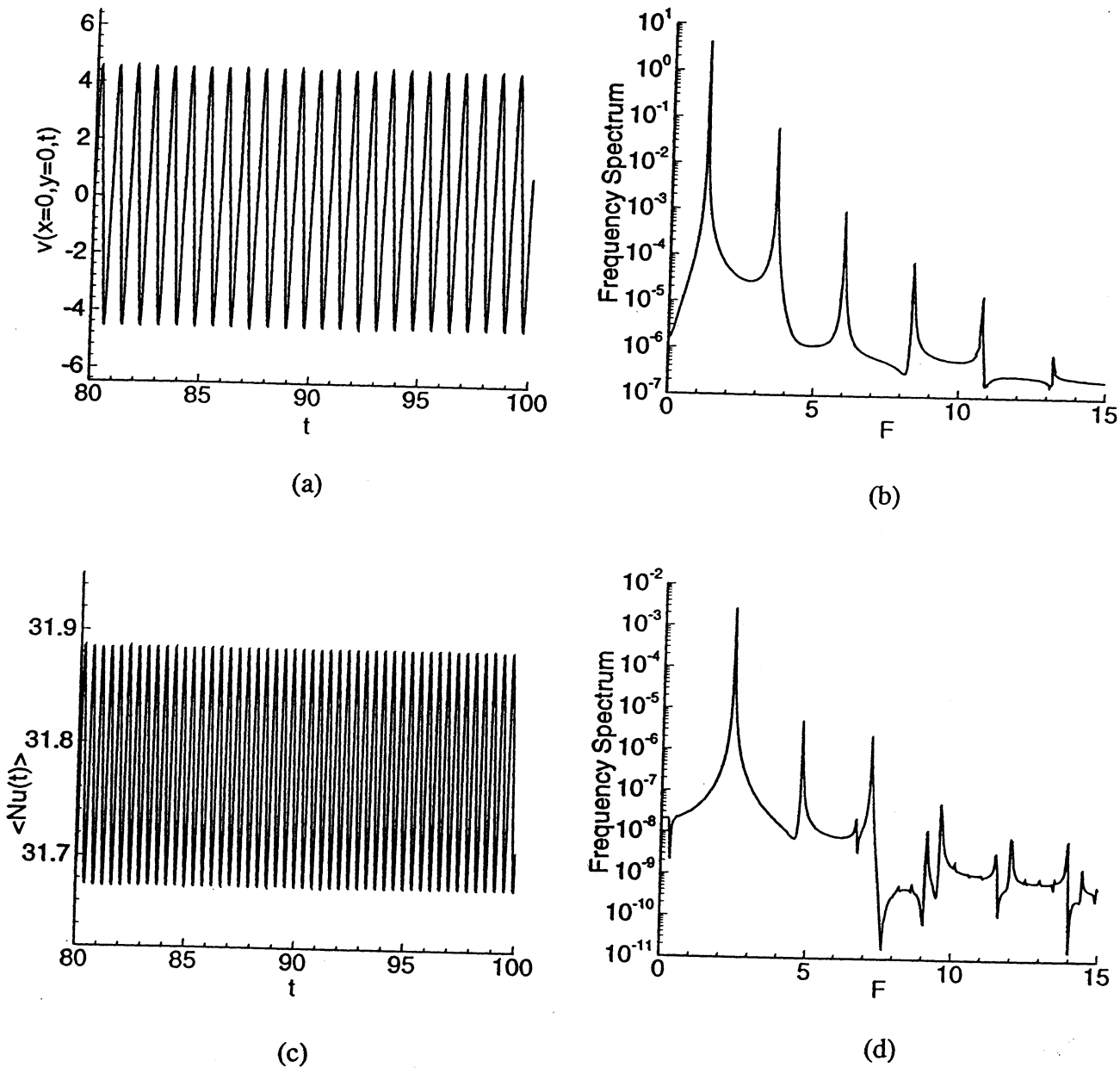

Figure 4.5 Frequency analysis of flow of unsteady inline at *Re = 1407*: (a) velocity υ (*x=0, y=0*) signal; (b) corresponding velocity frequency spectrum; (c) instantaneous global Nusselt number signal; (d) corresponding Nusselt number frequency spectrum.

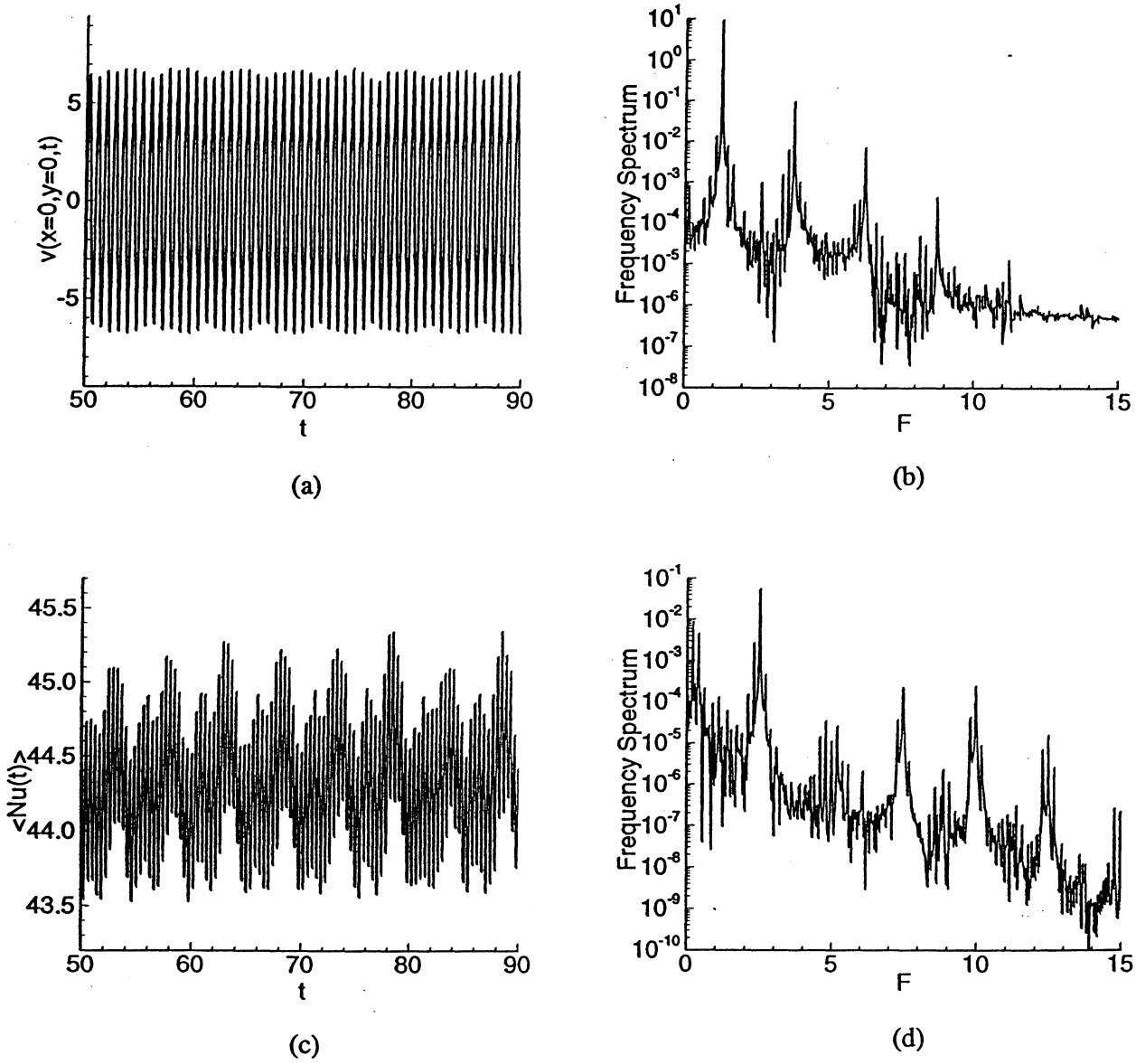

Figure 4.6 Frequency analysis of flow of unsteady inline at *Re = 2191*: (a) velocity υ (*x=0, y=0*) signal; (b) corresponding velocity frequency spectrum; (c) instantaneous global Nusselt number signal; (d) corresponding Nusselt number frequency spectrum.

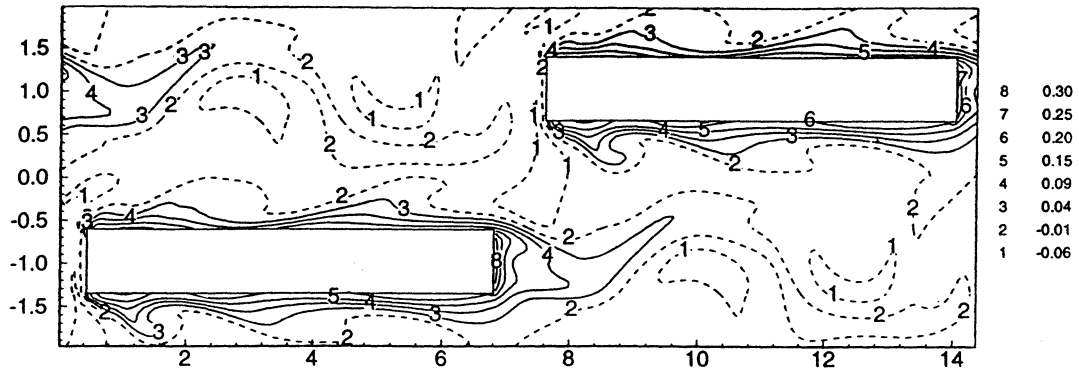

(a)

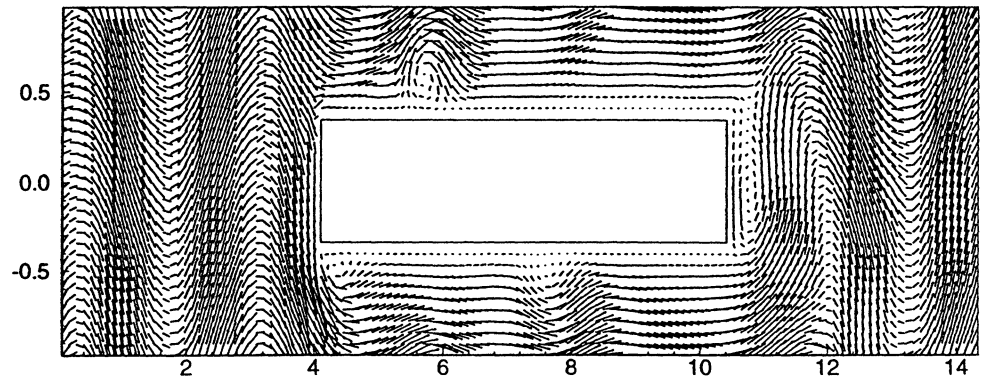

(b)

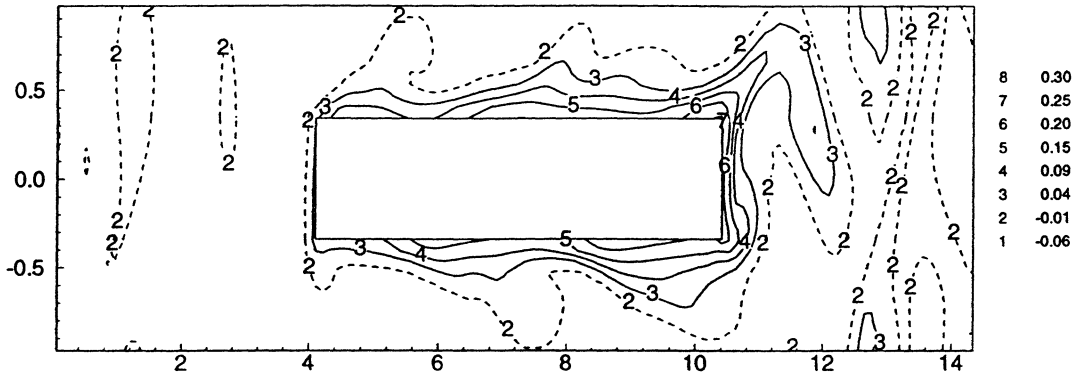

(c)

Figure 4.7 Comparison of flow and thermal fields of the two arrangements: (a) contour plot of perturbation temperature for the staggered arrangement at *Re = 1465* corresponding to the flow fields in Figure 4.4; (b) vector plot of velocity field, (b) contour plot of perturbation temperature for the inline arrangement at *Re = 1407.*

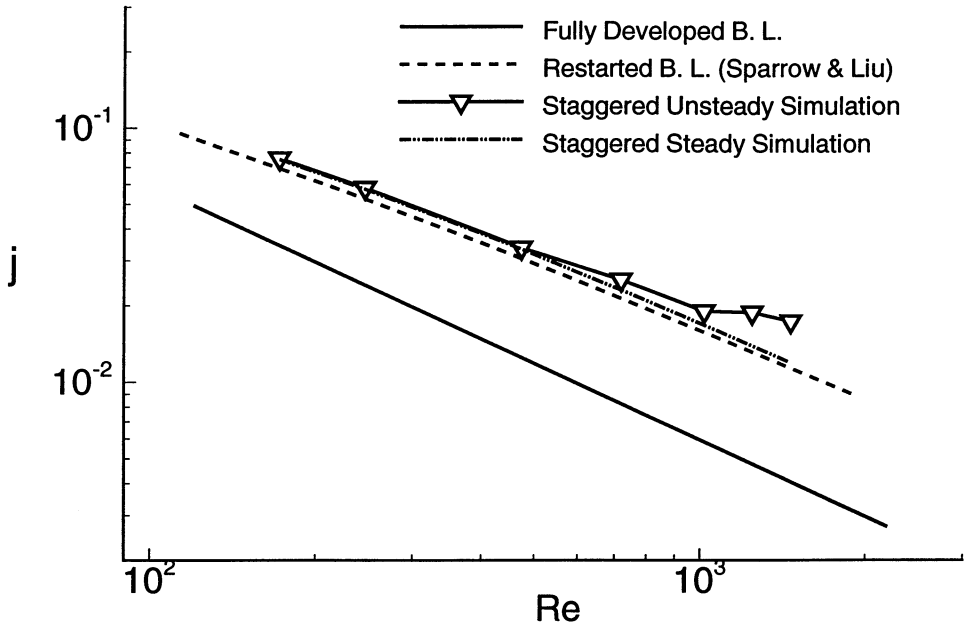

(a)

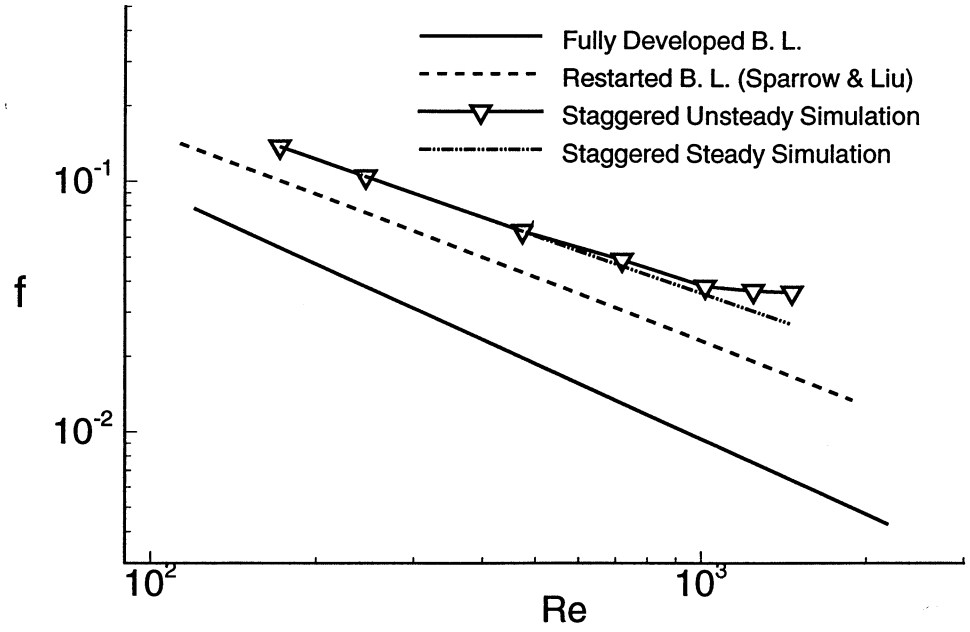

(b)

Figure 4.8 A comparison of individual heat transfer enhancement mechanisms and their effect on frictional losses in the staggered arrangement: (a) *j* factor, (b) friction factor.

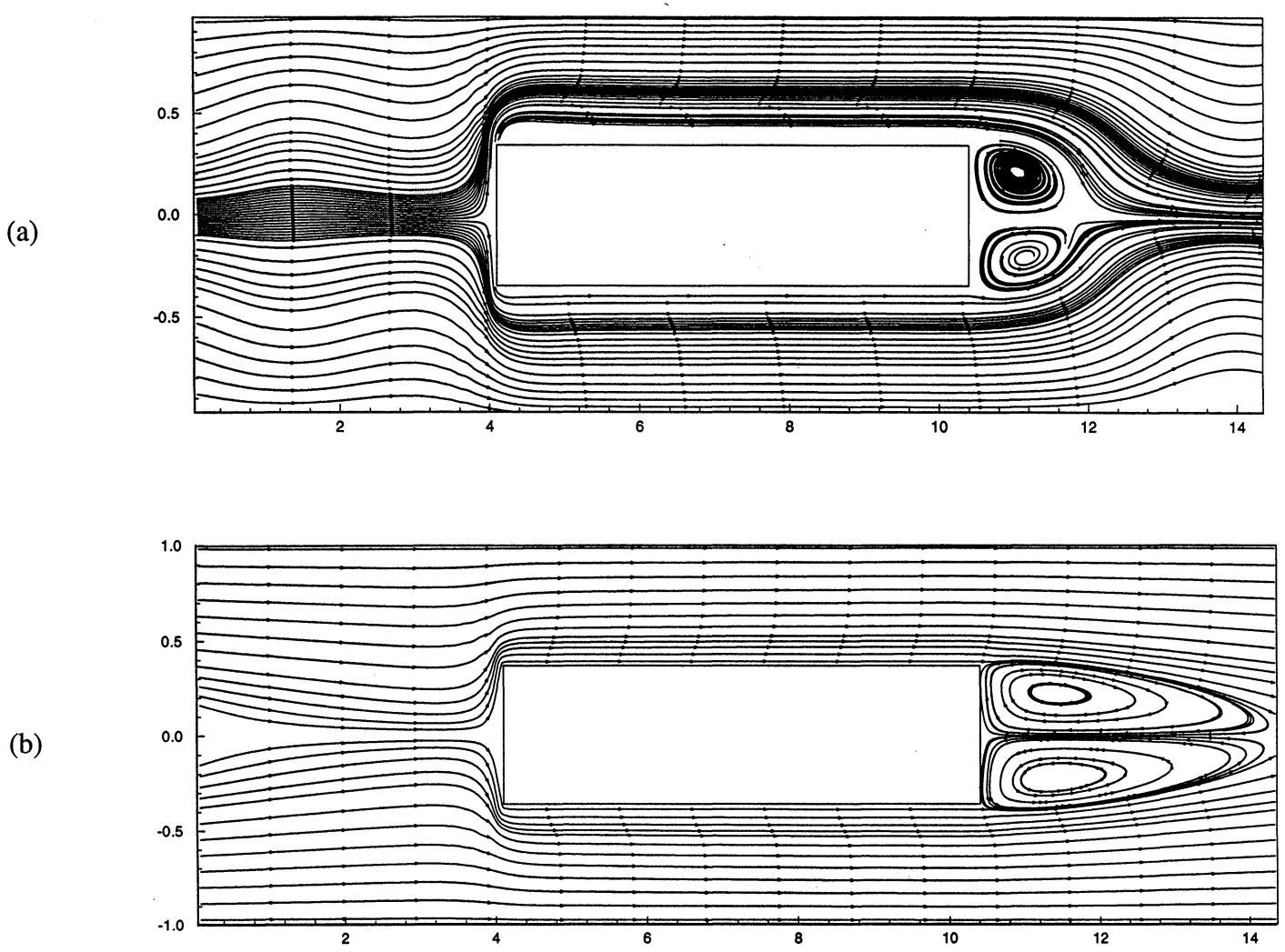

Figure 4.9 Streamlines at lower Reynolds numbers: (a) mean flow of unsteady inline simulation at *Re = 797*; (b) steady flow from symmetrized inline simulation at *Re = 804*.

(a)

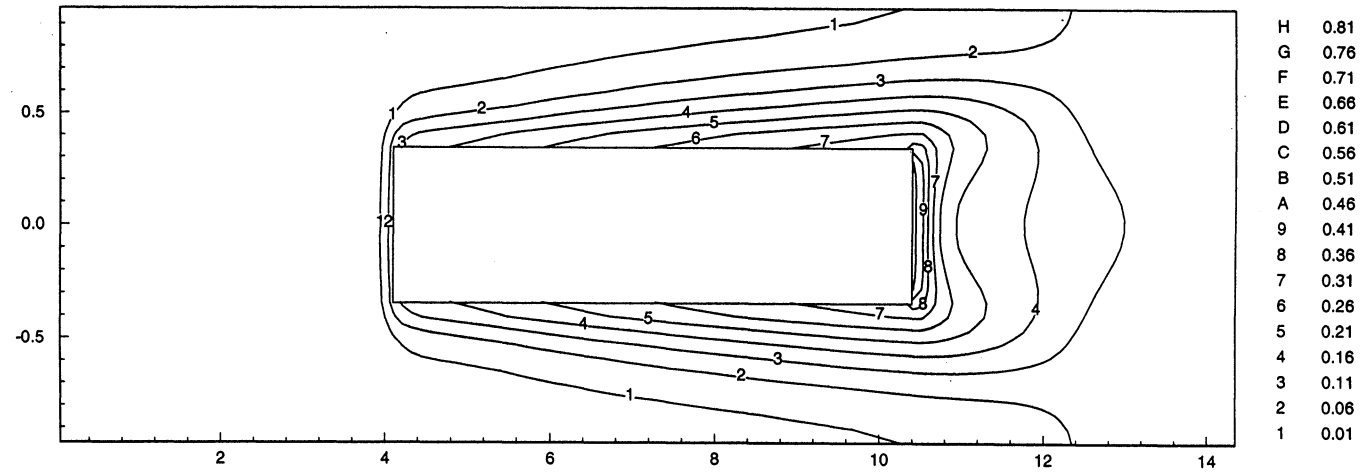

(b)

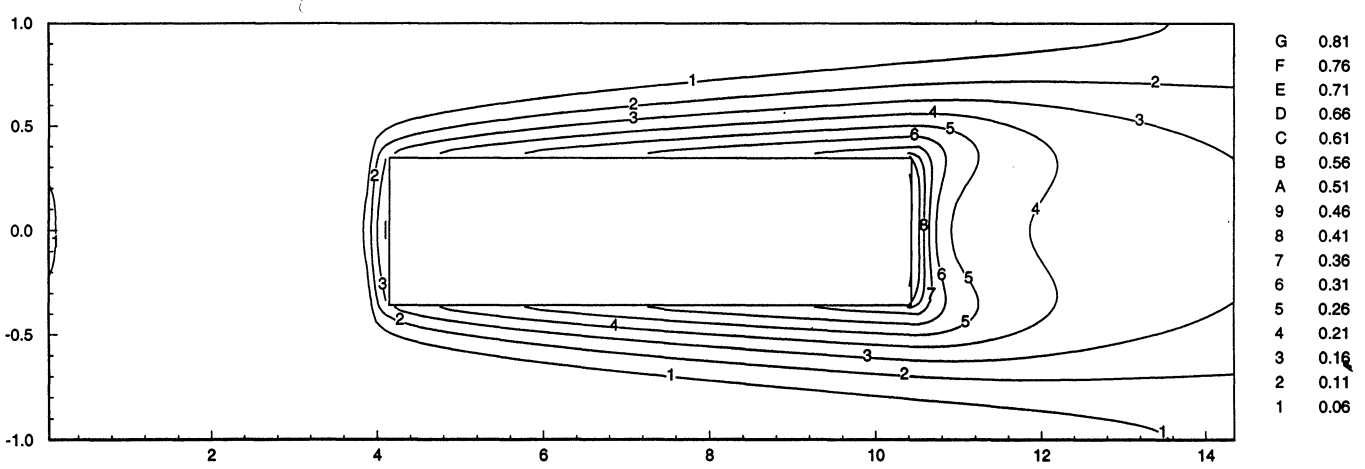

Figure 4.10 Temperature Contours at lower Reynolds numbers: (a) mean flow of unsteady inline simulation at *Re = 797*; (b) steady flow from symmetrized inline simulation at *Re = 804*.

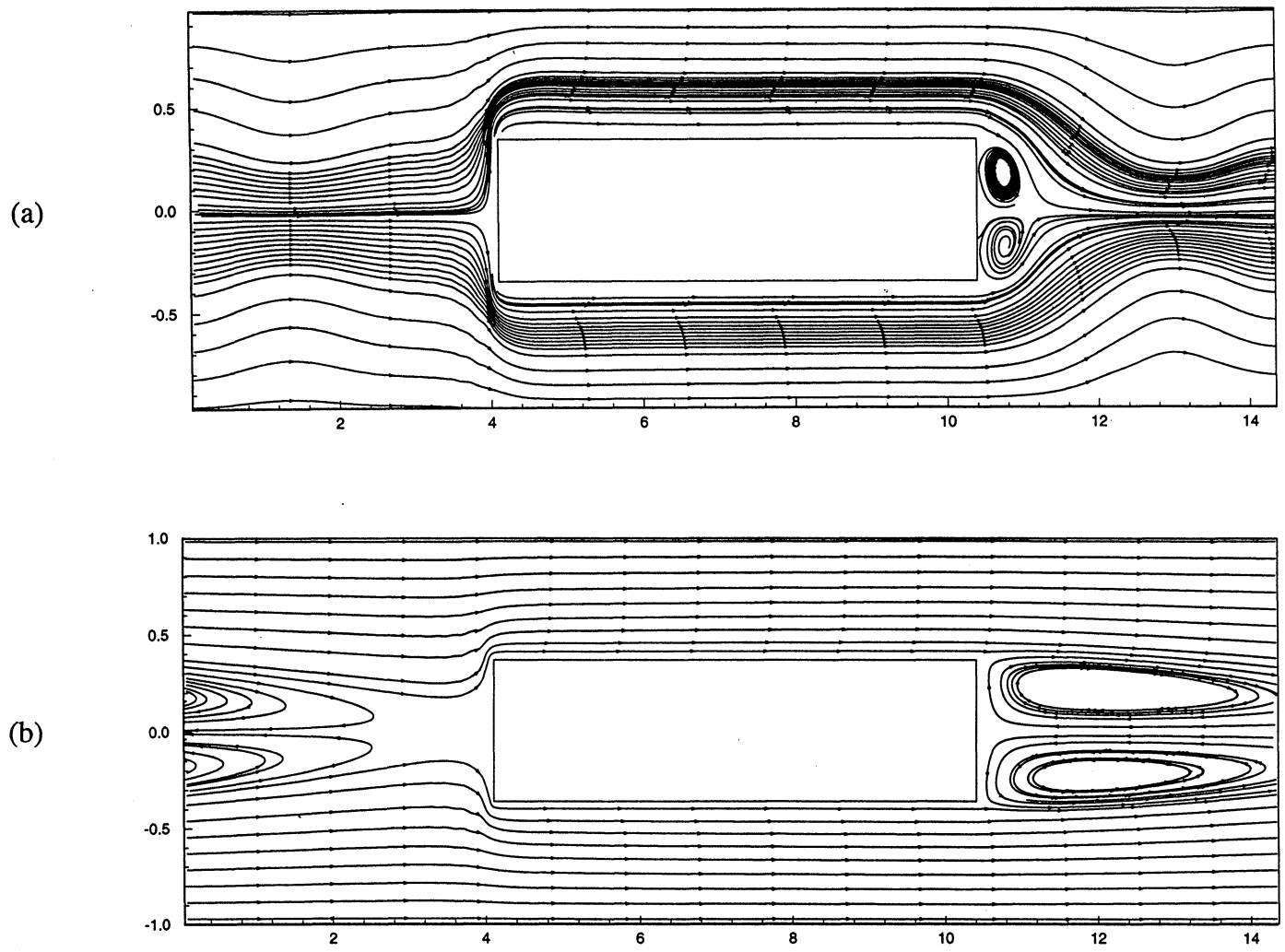

Figure 4.11 Streamlines at higher Reynolds numbers: (a) mean flow of unsteady inline simulation at *Re = 1407*; (b) steady flow from symmetrized inline simulation at *Re = 1458*.

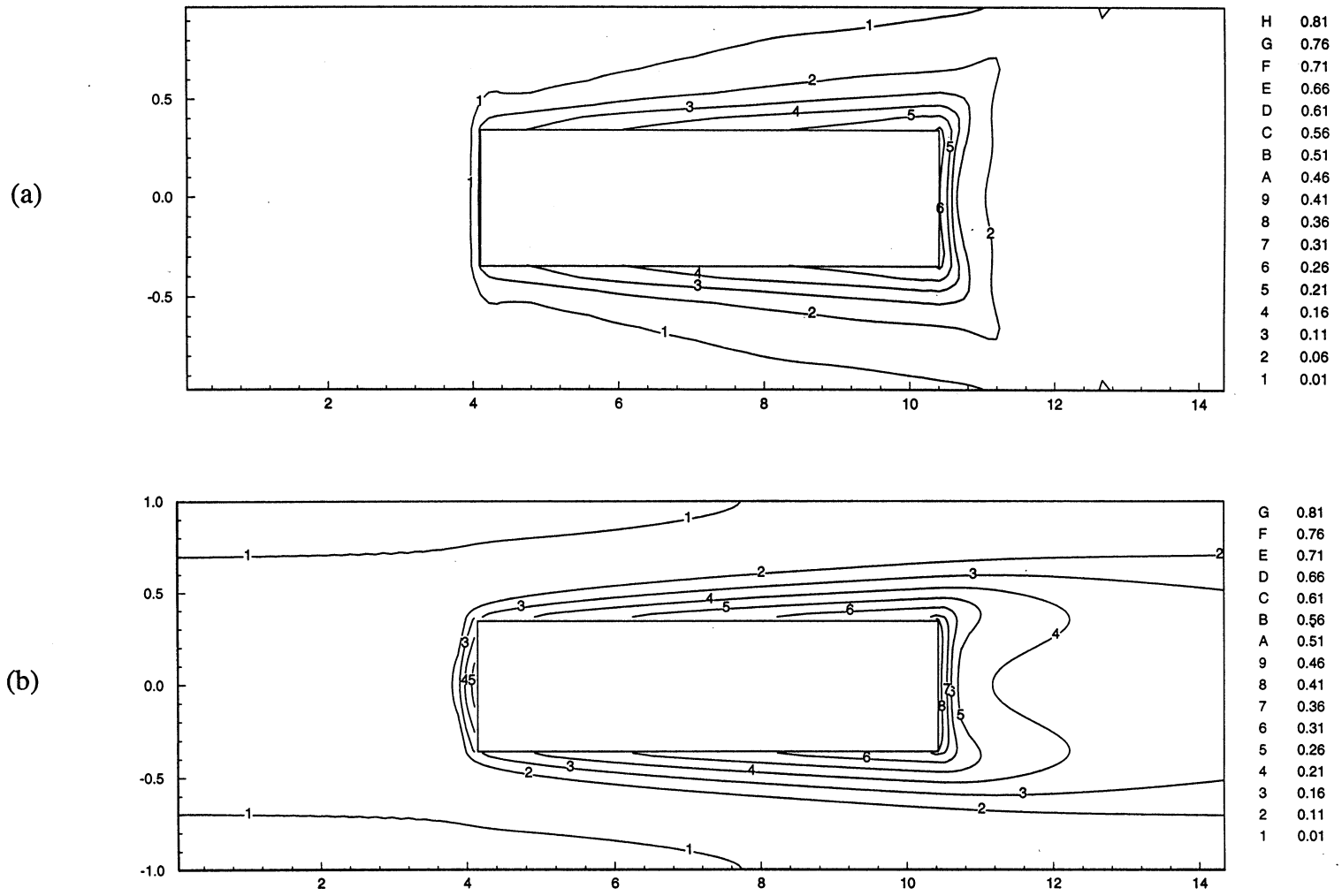

Figure 4.12 Temperature Contours at higher Reynolds numbers: (a) mean flow of unsteady inline simulation at *Re = 1407*; (b) steady flow from symmetrized inline simulation at *Re = 1458*.

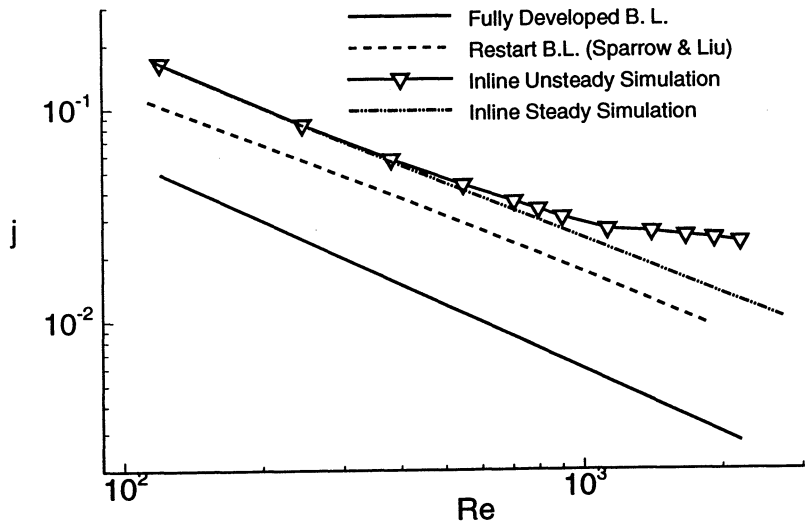

(a)

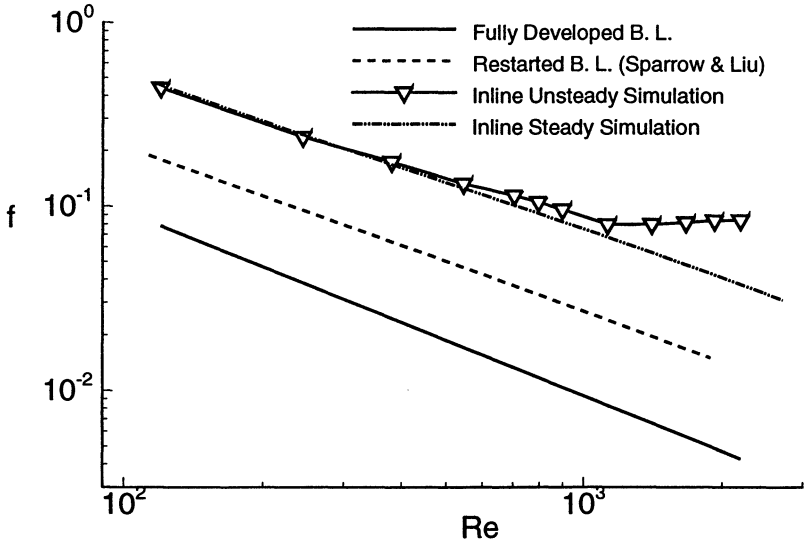

(b)

Figure 4.13 A comparison of individual heat transfer enhancement mechanisms and their effect on frictional losses in the inline arrangement: (a) *j* factor, (b) friction factor.

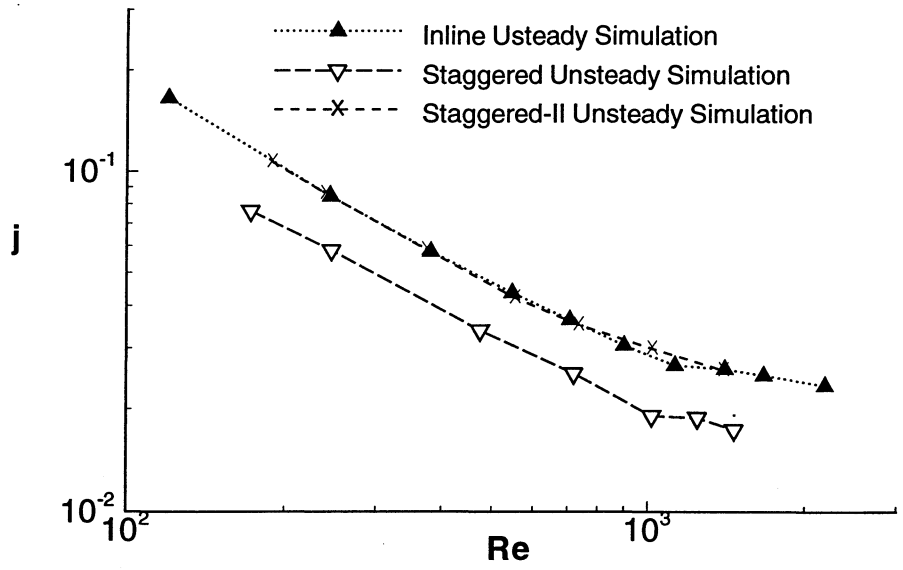

(a)

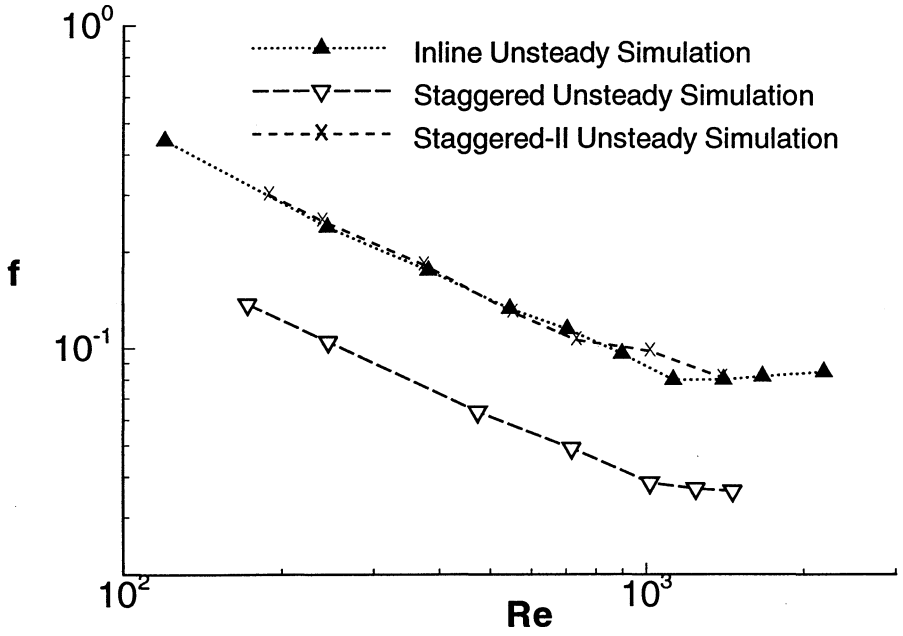

(b)

Figure 4.14 A comparison of overall performance due to different fin arrangements: (a) *j* factor, (b) friction factor.

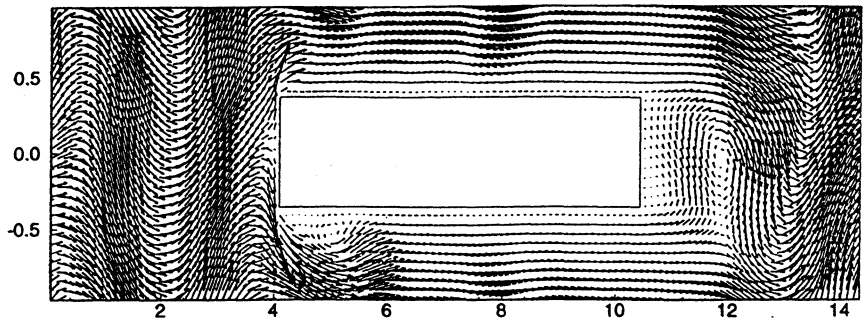

(a)

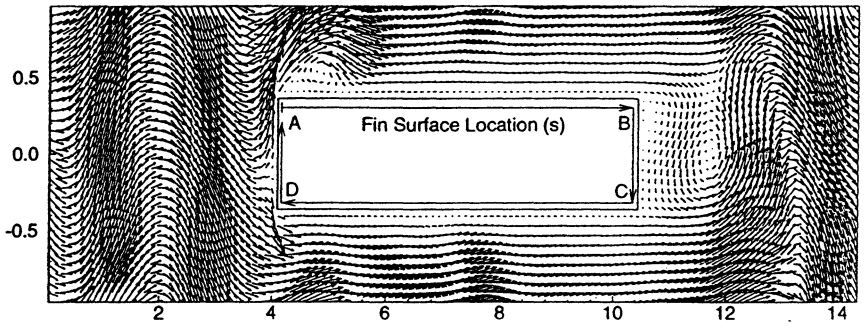

(b)

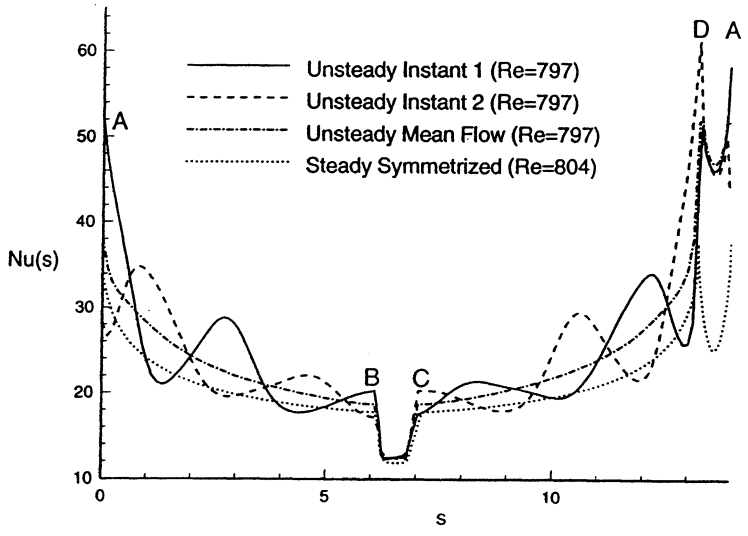

(c)

Figure 4.15 Vector plot of instantaneous velocity fields for the inline arrangement at *Re = 797* and local Nusselt number distribution: (a) instance 1; (b) instance 2, approximately *0.5* nondimensional time units after instance 1; (c) local Nusselt number distribution.

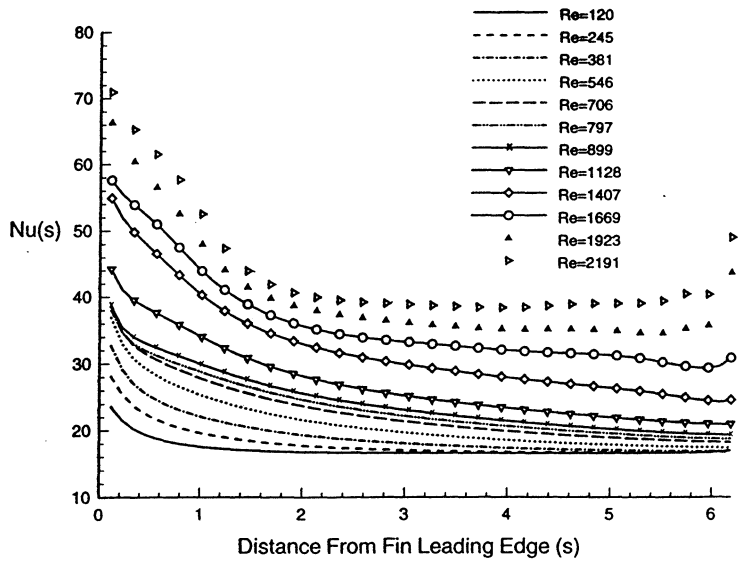

(a)

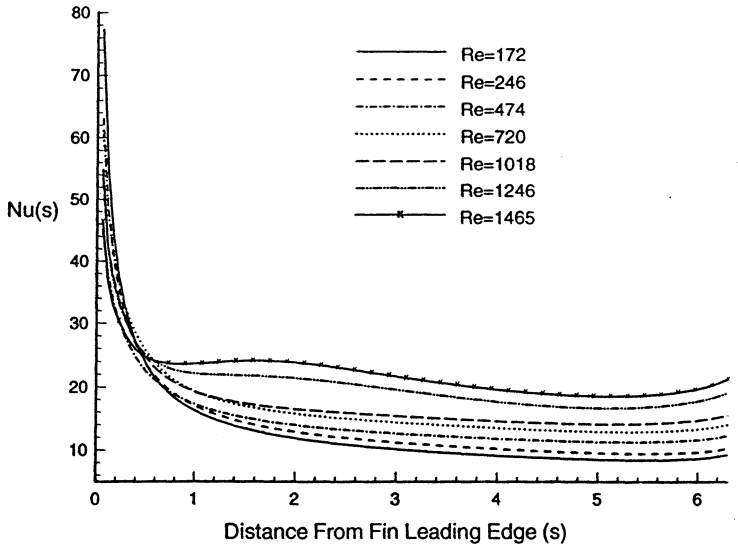

(b)

Figure 4.16 Time-averaged Nusselt number distribution on top fin surface: (a) in inline arrangement; (b) in staggered arrangement.

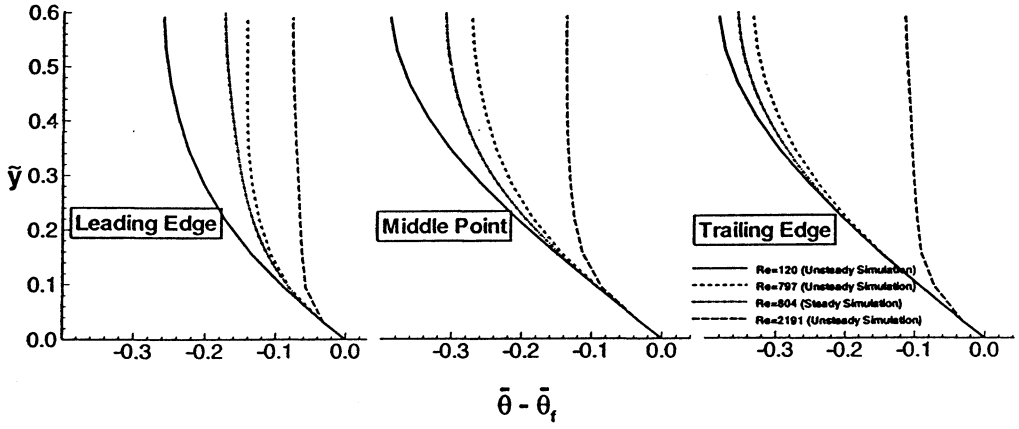

(a)

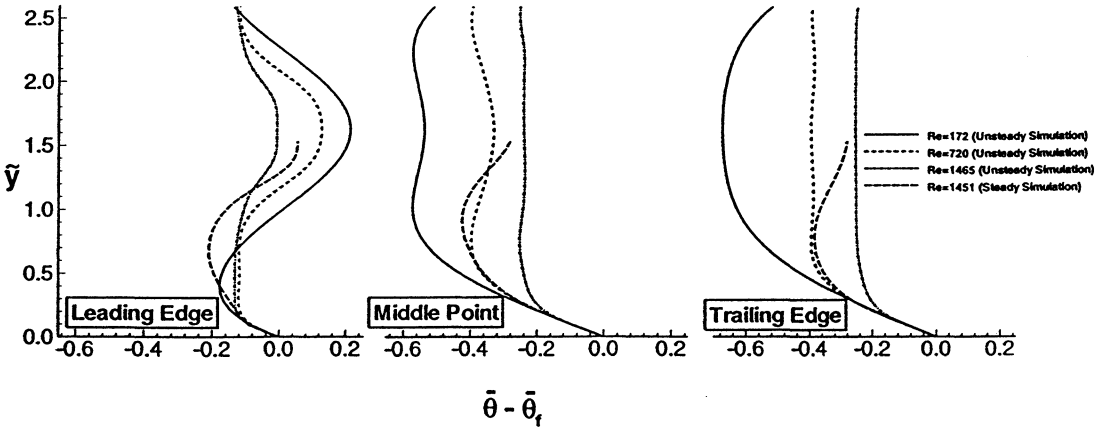

(b)

Figure 4.17 Time-averaged temperature difference as a function of distance away from the fin surface at three different streamwise locations: (a) in inline arrangement; (b) in staggered arrangement.

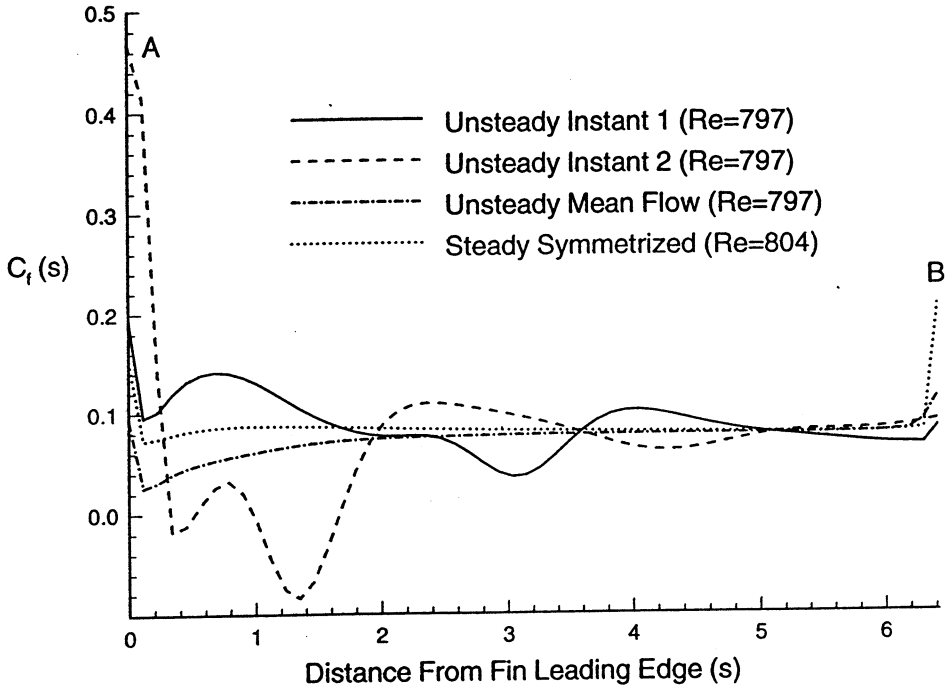

Figure 4.18 Local skin friction factor distribution along top fin surface in the inline arrangement corresponding to the flow fields shown in Figure 4.15.

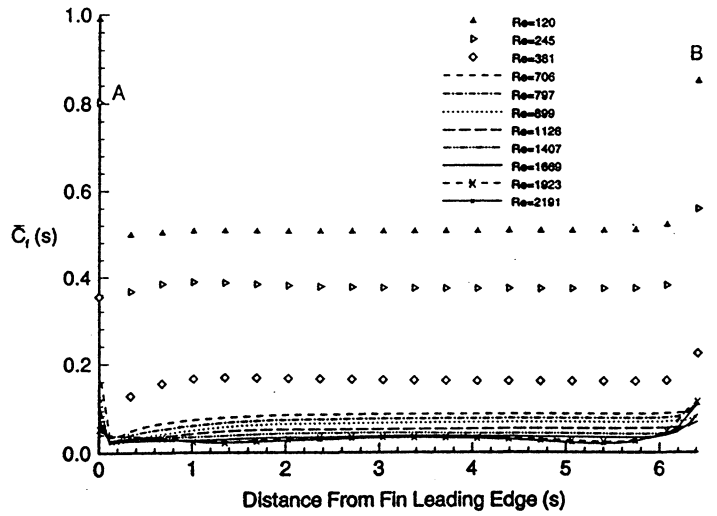

(a)

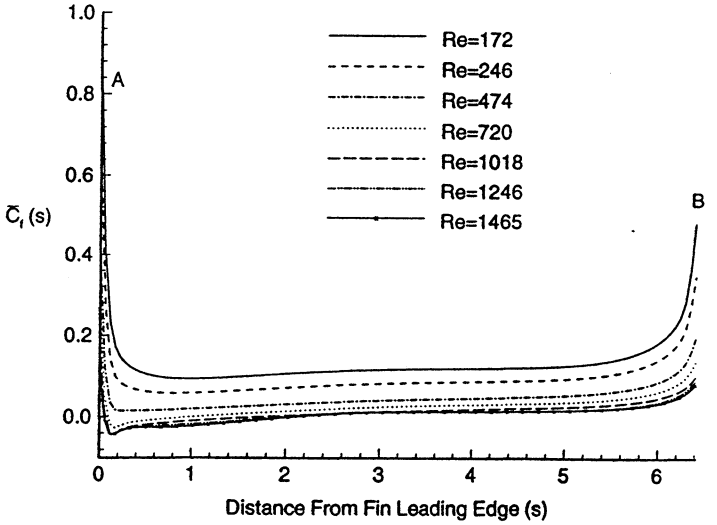

(b)

Figure 4.19 Time-averaged mean local skin friction factor distribution along top fin surface for both arrangements: (a) inline arrangement; (c) staggered arrangement.

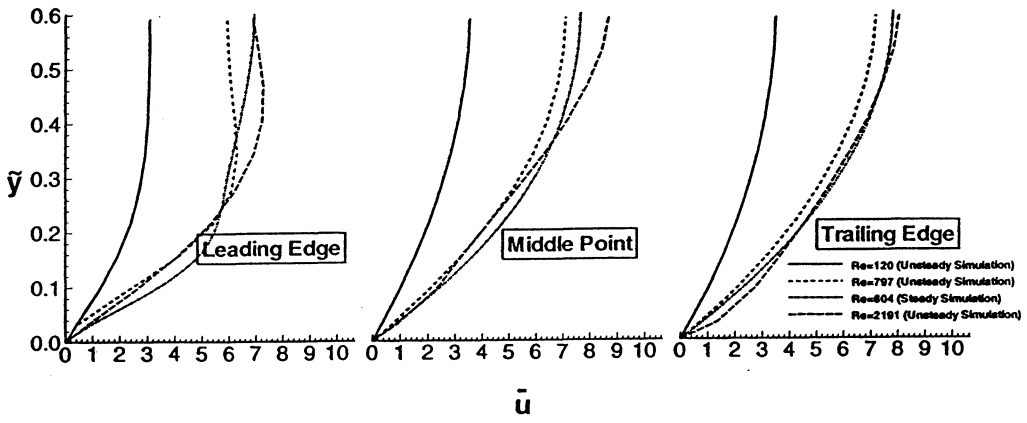

(a)

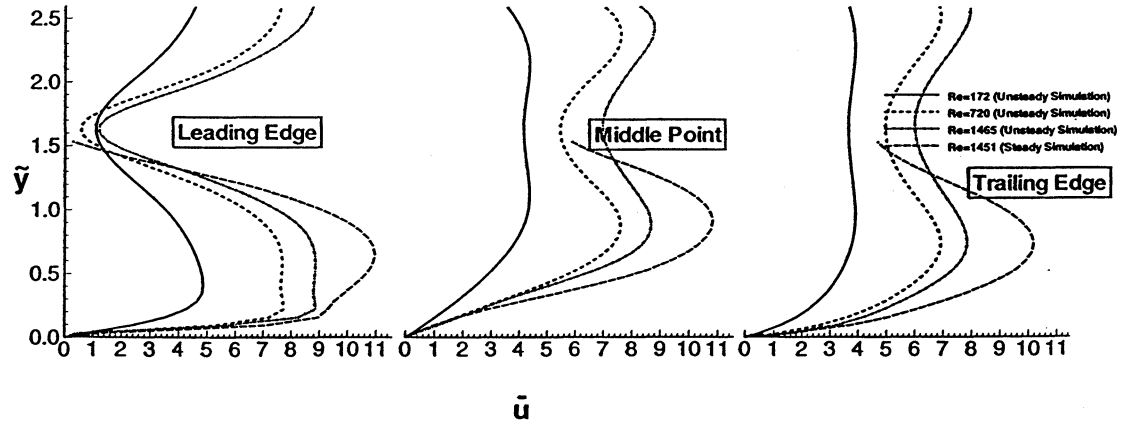

(b)

Figure 4.20 Time-averaged streamwise velocity profiles as a function of distance away from the top fin surface at three different streamwise locations: (a) in inline arrangement; (b) in staggered arrangement.

CHAPTER 5. EFFECT OF INTRINSIC THREE-DIMENSIONALITY ON HEAT TRANSFER AND FRICTIONAL LOSS

5.1 Motivation

In comparing current simulated results to the experimental data of Mullisen and Loehrke (1986) in Chapter 3, it was observed that the difference between the present simulation results and those of Mullisen and Loehrke (1986) increases for $Re > 1300$ as shown in Figure 3.3. It was conjectured that the effect of three-dimensionality at these high Reynolds numbers causes these deviations. Now the three-dimensional mechanisms affecting heat transfer and frictional losses will be explored in detail in this chapter.

From a more fundamental fluid dynamics aspect, flows in these periodically interrupted surfaces are manifestations of flows over bluff bodies. There is mounting evidence that the onset of three-dimensionality in wakes behind bluff bodies quickly follows the onset of periodic shedding. Here three-dimensionality refers to intrinsic three-dimensionality resulting from fluid dynamical instabilities at sufficiently high Reynolds number even in the case of two-dimensional geometries and must be separated from extrinsic three-dimensionality resulting from three-dimensional geometries. The most investigated problem in bluff body wakes is flow over circular cylinder owing to its simplicity and the existence of an analytical solution at low Reynolds numbers. It is well known that the flow goes through transition from steady laminar to two-dimensional unsteady at $Re_D \sim 45 - 50$, and then three-dimensionality sets in at $Re_D \sim 150 - 210$ [Roshko (1993)], where Re_D is the Reynolds number based on cylinder diameter. Recent work by Williamson (1989) and Zhang et al. (1994) has observed a series of three-dimensional instabilities as the Reynolds number increases until the flow finally becomes fully turbulent at $Re_D \sim 10^5$. These different instabilities have direct influence on the overall hydrodynamic quantities [Roshko (1993)]. For example, extensive evidence in the literature has shown that two-dimensional models of actual three-dimensional flows overpredict the drag [Williamson (1989), Roshko (1993), Mittal and Balachandar (1995)]. Mittal and Balachandar (1995) attributed this to higher in-plane Reynolds stresses in the wake of two-dimensional simulations

which substantially lower the mean base pressure, giving a much higher form drag than that in corresponding three-dimensional calculations.

Flows over more complex bluff body geometries such as rectangular cylinders are still unknown in many aspects. Overall the flow goes through similar transitional stages as Reynolds number increases. Davis and Moore (1982) numerically studied vortex shedding from rectangular cylinders over a range of Reynolds numbers, based on cylinder height, from *100* to *2800*. Their two-dimensional simulations described the evolution of the vortices both during and after the shedding and they have found that the properties of these vortices strongly depend on Reynolds number based on cylinder height. Their computed Strouhal numbers compared well with those obtained from wind-tunnel tests for Reynolds numbers below *1000*. Beyond this value they suggested that fully three-dimensional simulations need to be performed in order to achieve better comparisons with the experimental data. Tamura (1990) performed two- and three-dimensional time-dependent computations of the flow around a square cylinder at a Reynolds number based on cylinder height of 10^4. His computations showed that the flow patterns obtained by two-dimensional simulations are significantly different from those of three-dimensional simulations even though the geometry itself is two-dimensional with no variation in cross-section along the axis of the square cylinder. He observed that the three-dimensional structures decrease the average drag and lift coefficients in the case of nonzero angle of attack. In addition, he pointed out that these aerodynamic quantities from three-dimensional simulations are closer to the corresponding experimental data.

In the currently simulated geometries, the fin length is much larger than fin thickness. Skin friction contributes significantly to the overall friction factor, depending on the Reynolds number, as shown in Tables 4.1 and 4.2. However, the effect of three-dimensionality on skin friction is still unknown, although such information is vital to the explanation of the effect of three-dimensionality on the overall frictional loss in the currently simulated geometries. Furthermore, it seems natural that intrinsic three-dimensionality could also influence calculations of heat transfer quantities. However, all these questions remain unanswered.

The purpose of the current chapter is to study the effect of three-dimensional flow structures on the individual components of the heat transfer and frictional loss. Time-dependent three-dimension-

al simulations were performed for the inline arrangement (Case IL1) at $Re_\tau = 100$ ($Re \approx 2450$) and $Re_\tau = 140$ ($Re \approx 3500$). The former calculation was performed at a resolution of 256x64x64 in order to compare with the corresponding two-dimensional calculation performed with a resolution of 256x64, and the latter three-dimensional calculation used a resolution of 128x32x64 to compare with the corresponding two-dimensional simulation with a resolution of 128x32 (see Table 3.6). The three-dimensional calculations are initiated by applying a spanwise perturbation to the corresponding two-dimensional flow field at one time instant. The solutions are then integrated for about 85 and 120 nondimensional time units, respectively, well past the time when the flow has become fully three-dimensional and reached a stationary state.

Before presenting the calculated results, some useful quantities will be defined first. The overall drag coefficient, C_D, as a measure of total form drag, is defined as

$$C_D = \frac{D^*}{\frac{1}{2}\rho V^{*2} A^*_{front}} \tag{5.1}$$

where D^* is the dimensional total drag force, and $A_{front}{}^* = b^* L_z{}^*$ is the dimensional front (or back) fin surface area. The overall skin friction coefficient, C_F, as a measure of overall skin friction is defined as

$$C_F = \frac{F^*}{\frac{1}{2}\rho V^{*2} A^*_{front}} \tag{5.2}$$

where F^* is the dimensional total skin friction force.

5.2 Results and Discussion

The computed j factor and friction factor results from these three-dimensional simulations are plotted in Figure 3.3 along with the experimental data of Mullisen and Loehrke (1986). It is observed that the results from the three-dimensional simulations are in better agreement with experimental data. It is also observed that the amplitudes of rms fluctuations of the calculated j factor and friction factor from the two-dimensional simulations are significantly different from those obtained from the corresponding three-dimensional simulations. Figure 5.1 shows the time trace of j and f for the two–dimensional and corresponding three-dimensional simulations for the lower Reynolds

number case. It can be seen that the fluctuations in j and f are much higher in the two–dimensional simulation than in the three-dimensional simulation. The computed two-dimensional approximation overpredicts the rms j and f fluctuations by as much as *35%* and *56%,* respectively. This difference in the level of fluctuation increases as Reynolds number is increased. Figure 5.2 shows similar plots for the higher Reynolds number case, and it is observed that the computed two-dimensional approximation overpredicts the rms j and f fluctuations by as much as *87%* and *356%*. Tafti and Vanka (1991a) have found in two-dimensional simulations of flow over a blunt plate at Reynolds number based on plate thickness of *1000,* that the maximum rms value of pressure fluctuations calculated on the surface of the blunt plate is a factor of 4 higher than those observed in corresponding three-dimensional calculations [Tafti and Vanka (1991b)]. This was attributed to the strong coherence of vorticity, imposed by the two-dimensionality of the calculation. To gain a better understanding of the role of three-dimensionality, in the following sections, the strength and evolution of spanwise and streamwise vortices and their effect on heat transfer and frictional loss in two-dimensional and three-dimensional simulations will be considered.

5.2.1 Effect on Global and Mean Quantities

The effect of three-dimensionality on the time-averaged mean heat transfer for simulations at $Re_\tau = 100$ ($Re \approx 2450$) is shown in Table 5.1 and the effect on time-averaged mean frictional loss is shown in Table 5.2. Similar results are shown in Table 5.3 and Table 5.4 for simulations at $Re_\tau = 140$ ($Re \approx 3500$). In these tables, percentages of overprediction (+) and underprediction (–) of the two-dimensional simulation over the corresponding three-dimensional simulation, have also been listed. For the same pressure drop given by a fixed Re_τ, in the two-dimensional simulation, the flow velocity slightly changes and thus results in a small variation in the Reynolds number based on hydraulic diameter. The two-dimensional simulation overpredicts the j factor by *16.8%* and underpredicts the friction factor f by *0.5%* for the lower Reynolds number case, while it overpredicts the j factor by as much as *25.2%* and the friction factor f by *3.6%* for the higher Reynolds number case. In both cases, the small change in friction factor comes from the near cancellation of substantial changes in the two components of the friction factor: form drag and skin friction. At the lower

Reynolds number, the two-dimensional simulation overpredicts the form drag coefficient by as much as *13.2%*, however it underpredicts the overall skin friction coefficient by as much as *26.3%*. At this Reynolds number, the three-dimensional form drag is nearly twice as large as skin friction, therefore the overprediction in form drag is counter-balanced by the underprediction in skin friction, resulting in a negligible change in the friction factor f. At the higher Reynolds number, the overprediction in the form drag coefficient increases to *37.4%*, the underprediction also in skin friction increases to *42.6%*, but the contribution to the overall frictional loss from form drag has increased slightly, resulting in the prediction of a slightly higher friction factor.

Figure 5.3 shows the time-averaged mean flow streamlines and corresponding temperature contours for the two-dimensional simulation at $Re_\tau = 100$ ($Re \approx 2450$) and plots from corresponding three-dimensional simulation are shown in Figure 5.4. It is evident that with the introduction of three-dimensionality, the mean wake bubble increases in size by nearly *200%* and thus reduces the base suction pressure and therefore resulting in a lower form drag in the three-dimensional simulation. Recirculation zones can be observed near the leading edge in the three-dimensional simulation. This has significant effect on local heat transfer and skin friction prediction which will be discussed in a later section.

Figure 5.5 shows the time-averaged mean spanwise vorticity, $\overline{\omega}_z$, for the two-dimensional simulation along with the time- and spanwise-averaged mean spanwise vorticity for the corresponding three-dimensional simulation. This comparison clearly shows that on the top and bottom fin surfaces, vorticity is closer to the fin surfaces in the three-dimensional simulation than that in the two-dimensional simulation, whereas the vorticity distribution in the two-dimensional wake is drawn closer to the base of the fin than in the three-dimensional case, consistent with the streamlines shown in Figures 5.3 and 5.4.

Time-averaged mean velocity $\overline{u}$ and temperature difference, $\overline{\theta}$–$\overline{\theta}_f$, profiles for both two- and three-dimensional simulations at $Re_\tau = 100$ ($Re \approx 2450$) as a function of distance away from the top fin surface, $\tilde{y}$, are plotted at three different locations: at the leading edge as shown in Figure 5.6, at the middle of top surface as shown in Figure 5.7 and at the trailing edge of the top fin surface as shown in Figure 5.8. Here $\overline{\theta}_f$ is the time-averaged mean fin surface temperature. At the leading edge,

the negative value of $\bar{u}$ indicates the presence of recirculation zones in the three-dimensional simulation. The effect of these recirculation zones is to induce local negative skin friction near the leading edge, thus decreasing the overall skin friction contribution to friction factor in the three-dimensional simulation. But the velocity profile quickly recovers and rapidly approaches a turbulent flow-like profile. In contrast, in the two-dimensional simulation, the downstream development of the velocity profile is slow which is characteristic of a laminar boundary layer. However, the mean temperature difference profiles develop at the same rate near the fin surface due to the constant heat flux boundary condition imposed which fixed the gradient on the fin surface. But the enhanced mixing in the two-dimensional simulation results in higher freestream temperature as observed in the smaller temperature difference and thus higher heat transfer coefficient.

Figure 5.9 shows the pressure distribution on the front and back fin surfaces. On the front fin surface, though both simulations have similar parabolic profiles, the pressure predicted by the two-dimensional simulation is lower than that by the three-dimensional simulation by as much as *31%*. However on the back fin surface, the two-dimensional simulation predicts a much higher suction pressure while the three-dimensional simulation predicts a lower and nearly constant suction pressure, and this overprediction is as much as *45%*. Thus this results in an overprediction of form drag.

Figure 5.10 shows the time-averaged mean local skin friction distribution on the top fin surface. The drop in local skin friction near the leading edge in the three-dimensional simulation corresponds to the recirculation zone near the leading edge which is absent in the corresponding two-dimensional simulation. The skin friction in the three-dimensional simulation soon becomes nearly constant after the leading edge. The coherent spanwise vortices observed in the two-dimensional simulations bring freestream fluid to the fin surface on the downstream side and push away the fluid on the upstream side as discussed in Chapter 4. During this process, these strong spanwise vortices also introduce negative flow velocity near the fin surface and thus, results in a smaller time-averaged mean velocities near the top and bottom fin surfaces in the two-dimensional simulations as observed in the velocity profiles shown in Figures 5.6, 5.7 and 5.8. This results in smaller skin friction in the two-dimensional simulations.

Figure 5.11 shows the time-averaged mean local Nusselt number distribution on the top fin surface. Again the drop in local Nusselt number near the leading edge in the three-dimensional simulation corresponds to the recirculation zone in the mean flow. The Nusselt number in the two-dimensional simulation is generally higher than that in three-dimensional simulation. At the lower Reynolds number, the two-dimensional simulation overpredicts the front fin, top/bottom and back fin surfaces by *8.0%*, *14.2%* and *28.0%*, respectively, resulting in an overall overprediction of *16.8%* in the *j* factor. Similar overprediction has been observed at the higher Reynolds number.

5.2.2 Effect of Vortex Dynamics on Heat Transfer and Frictional Loss

In this section the flow characteristics, especially the vortex dynamics, will be analyzed to help gain a better understanding of the above differences in the global/mean quantities between the two-dimensional and three-dimensional simulations. Here vortices are identified by analyzing the magnitude of the imaginary part of the eigenvalue, λ_i, of the velocity gradient tensor to identify the vortical structures of the flow. This approach has been used in studying flow over circular cylinders by Mittal and Balachandar (1995), and it has been suggested and used before by Soria and Cantwell (1993) in studying free turbulent shear flows and by Zhou, Adrian and Balachandar (1996) in studying turbulent channel flows. This method is frame invariant and identifies vortical structures as regions of large vorticity where rotation dominates over strain thus correctly eliminating shear layers from consideration. The presence of closed streamlines in regions where the velocity gradient tensor exhibits complex eigenvalues can be clearly demonstrated in the case of a two-dimensional incompressible flow. Here this methodology will be separately applied in the *x-y* and *y-z* planes in order to identify spanwise and streamwise vortices, respectively. Considering an incompressible flow, the velocity gradient tensor on a two-dimensional plane is given by

$$\nabla \boldsymbol{u} = \begin{bmatrix} a & b \\ c & d \end{bmatrix} \tag{5.3}$$

Here $a = \partial u/\partial x$, $b = \partial u/\partial y$, $c = \partial v/\partial x$ and $d = \partial v/\partial y$ for flows in the *x-y* plane, while $a = \partial v/\partial y$, $b = \partial v/\partial z$, $c = \partial w/\partial y$ and $d = \partial w/\partial z$ for flows in the *y-z* plane. This velocity gradient tensor can be decomposed into a shear tensor, **E**, and rotation tensor, **R**, as

$$\nabla \boldsymbol{u} = \boldsymbol{E} + \boldsymbol{R} \tag{5.4}$$

where

$$\boldsymbol{E} = \begin{bmatrix} a & \frac{b+c}{2} \\ \frac{b+c}{2} & -a \end{bmatrix} \quad \text{and} \quad \boldsymbol{R} = \begin{bmatrix} 0 & \frac{b-c}{2} \\ -\frac{b-c}{2} & 0 \end{bmatrix} \tag{5.5}$$

The eigenvalues of the velocity gradient, shear and rotation tensors are given by

$$\lambda_{\nabla u} = \pm \, (a^2 + bc)^{\frac{1}{2}} \tag{5.6}$$

$$\lambda_E = \pm \left[a^2 + (\frac{b+c}{2})^2 \right]^{\frac{1}{2}} \tag{5.7}$$

$$\lambda_R = \pm \, i\frac{b-c}{2} \tag{5.8}$$

respectively. The three eigenvalues can be related to each other by

$$\lambda_{\nabla u}^2 = \lambda_E^2 + \lambda_R^2 \tag{5.9}$$

If $|\lambda_E| < |\lambda_R|$, then $\lambda_{\nabla u}$ is imaginary and this implies that the strength of rotation exceeds the strength of shear. Thus, imaginary eigenvalues, λ_i, are a necessary and sufficient condition for the existence of closed local streamlines and by definition, for the existence of vortical structures in two-dimensional planes of incompressible flows.

Figure 5.12 compares the instantaneous velocity vectors from the two-dimensional simulation with the instantaneous spanwise-averaged velocity vectors from the corresponding three-dimensional simulation at $Re_\tau = 100$ ($Re \approx 2450$). Note that in both simulations at this instance, a strong vortex has just formed near the leading edge of the bottom fin. However the vortex in the two-dimensional simulation is much stronger as can be observed in the corresponding λ_i contours shown in Figure 5.13. Furthermore, the vortices formed near the leading edge in the two-dimensional simulation are able to maintain their strength and convect downstream until almost the trailing edge of the fin. However this is not the case in the three-dimensional simulation: the relatively weaker vortices formed near the leading edge die out very quickly before even they reach the middle of the fin surface. Figure 5.14(a) shows the contours of the time-averaged λ_i in the x-y plane for the two-dimensional simulation at this Reynolds number and Figure 5.14(b) shows the contours of the time- and spanwise-averaged λ_i in the x–y plane for the corresponding three-dimensional simulation. It is

evident that the strength of the spanwise vortices in the two-dimensional simulation is much larger than that in the three-dimensional simulation. These strong coherent vortices in the two-dimensional simulation create a well-mixed flow and thus increase the heat transfer, resulting in the overprediction of the j factor.

The streamwise vorticity in the three-dimensional simulation, which is absent in the two-dimensional simulation, also plays a very important role in determining the overall heat transfer and friction loss and contributes significantly to the difference in the results between the two simulations. Figure 5.15 shows the velocity vectors in one y-z plane ($x = 5.4$) and the corresponding λ_i contours from the three-dimensional simulation at one instance and Figure 5.16 shows similar plots at a later instance. The two instances are *0.1* nondimensional time units apart. It is evident that the streamwise vortices are present and that they evolve in time and bring freestream fluid towards the top and bottom fin surfaces, contributing to the turbulent-like velocity profiles in the three-dimensional simulation. At the same time these streamwise vortices seem to weaken the spanwise vortices, compared with the strong coherent vortices in the corresponding two-dimensional simulation. Figure 5.17 shows the time- and spanwise- averaged and also averaged along the fin length imaginary eigenvalues, $<\lambda_i>_{t,z,f}$, profiles along the transverse axis. This shows that most strong streamwise vortices are concentrated near the fin top and bottom surfaces.

Table 5.1: Effect of three-dimensionality on mean heat transfer at $Re_\tau = 100$ ($Re \approx 2450$)

	Re	*j*	*Nu* (Front)	*Nu* (Top, Bottom)	*Nu* (Back)
2–D[1]	*2455*	*0.0188*	*73.8358*	*39.7529*	*26.9906*
3–D[2]	*2449*	*0.0161*	*68.3812*	*34.8134*	*21.0806*
Difference %	*+0.2%*	*+16.8%*	*+8.0%*	*+14.2%*	*+28.0%*

[1]Grid size *256x64*, [2]Grid size *256x64x64*

Table 5.2: Effect of three-dimensionality on mean frictional loss at $Re_\tau = 100$ ($Re \approx 2450$)

	f	C_D	C_f	**Skin Friction Contribution**	**Form Drag Contribution**
2–D[1]	*0.0587*	*1.4971*	*0.5234*	*25.9%*	*74.1%*
3–D[2]	*0.0590*	*1.3221*	*0.7098*	*34.9%*	*65.1%*
Difference %	*–0.5%*	*+13.2%*	*–26.3%*	*–25.8%*	*+13.8%*

[1]Grid size *256x64*, [2]Grid size *256x64x64*

Table 5.3: Effect of three-dimensionality on mean heat transfer at $Re_\tau = 140$ ($Re \approx 3500$)

	Re	*j*	*Nu* (Front)	*Nu* (Top, Bottom)	*Nu* (Back)
2–D[1]	*3474*	*0.0179*	*51.1999*	*55.9954*	*34.7988*
3–D[2]	*3535*	*0.0143*	*50.3808*	*46.9867*	*26.9390*
Difference %	*–1.7%*	*+25.2%*	*+1.6%*	*+19.2%*	*+29.2%*

[1]Grid size *128x32*, [2]Grid size *128x32x64*

Table 5.4: Effect of three-dimensionality on mean frictional loss at $Re_\tau = 140$ ($Re \approx 3500$)

	f	C_D	C_f	**Skin Friction Contribution**	**Form Drag Contribution**
2–D[1]	*0.0575*	*1.7363*	*0.3707*	*17.6%*	*82.4%*
3–D[2]	*0.0555*	*1.2636*	*0.6459*	*33.8%*	*66.2%*
Difference %	*+3.6%*	*+37.4%*	*–42.6%*	*–47.9%*	*+24.5%*

[1]Grid size *128x32*, [2]Grid size *128x32x64*

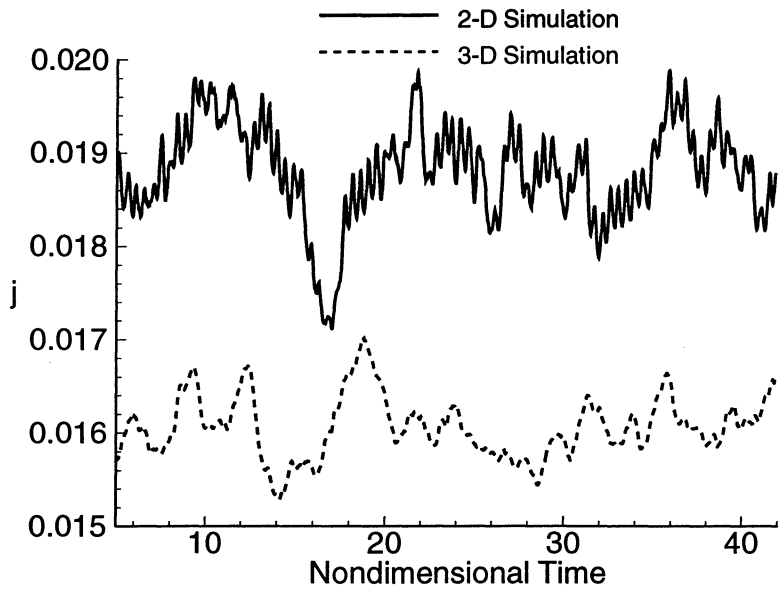

(a)

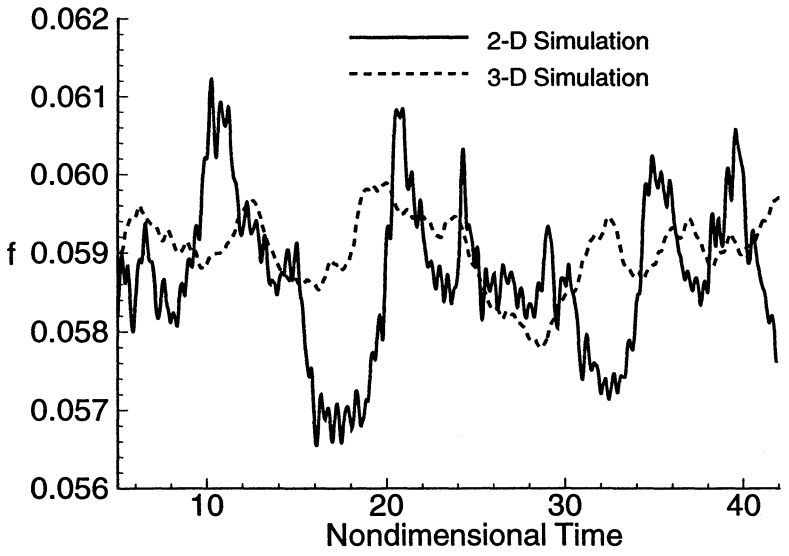

(b)

Figure 5.1 Comparison of time history of overall heat transfer and frictional loss from two- and three-dimensional simulations for the lower Reynolds number case of $Re_\tau = 100$ ($Re \approx 2450$): (a) j factor; (b) friction factor f.

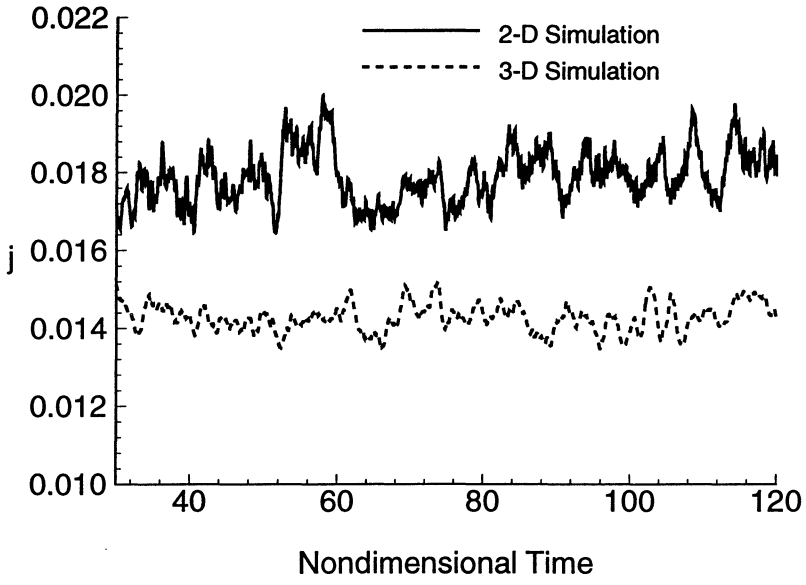

(a)

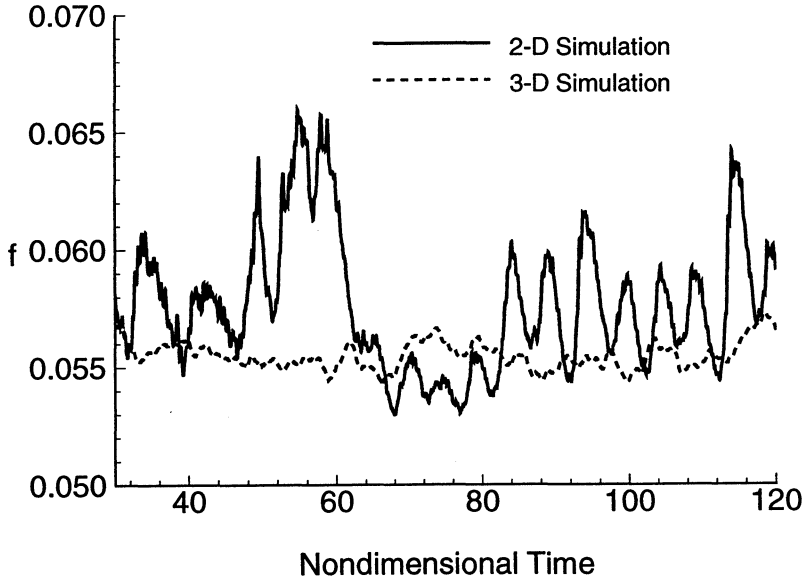

(b)

Figure 5.2 Comparison of time history of overall heat transfer and frictional loss from two- and three-dimensional simulations for the higher Reynolds number case of $Re_\tau = 140$ ($Re \approx 3500$): (a) j factor; (b) friction factor f.

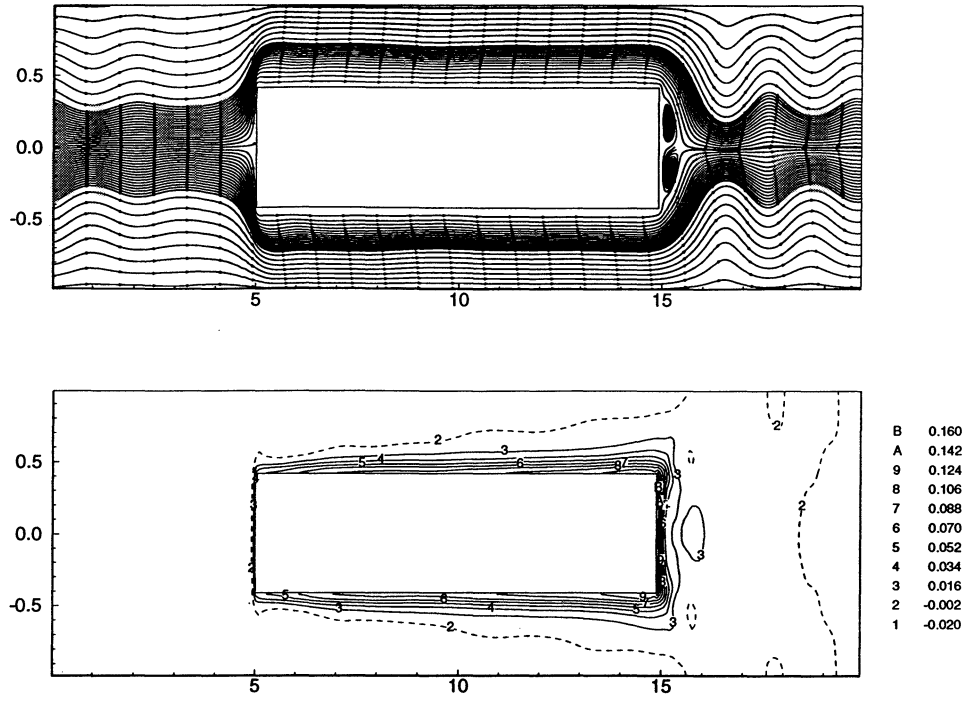

Figure 5.3 Time-averaged mean flow streamlines and temperature contours from the two-dimensional simulation.

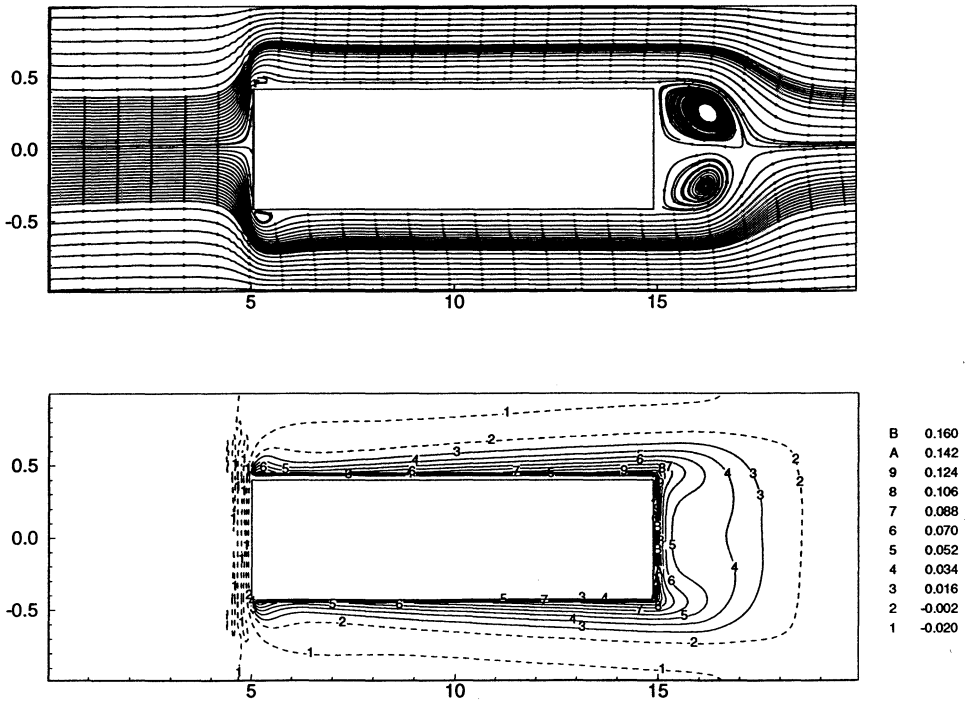

Figure 5.4 Time-averaged mean flow streamlines and temperature contours from the corresponding three-dimensional simulation.

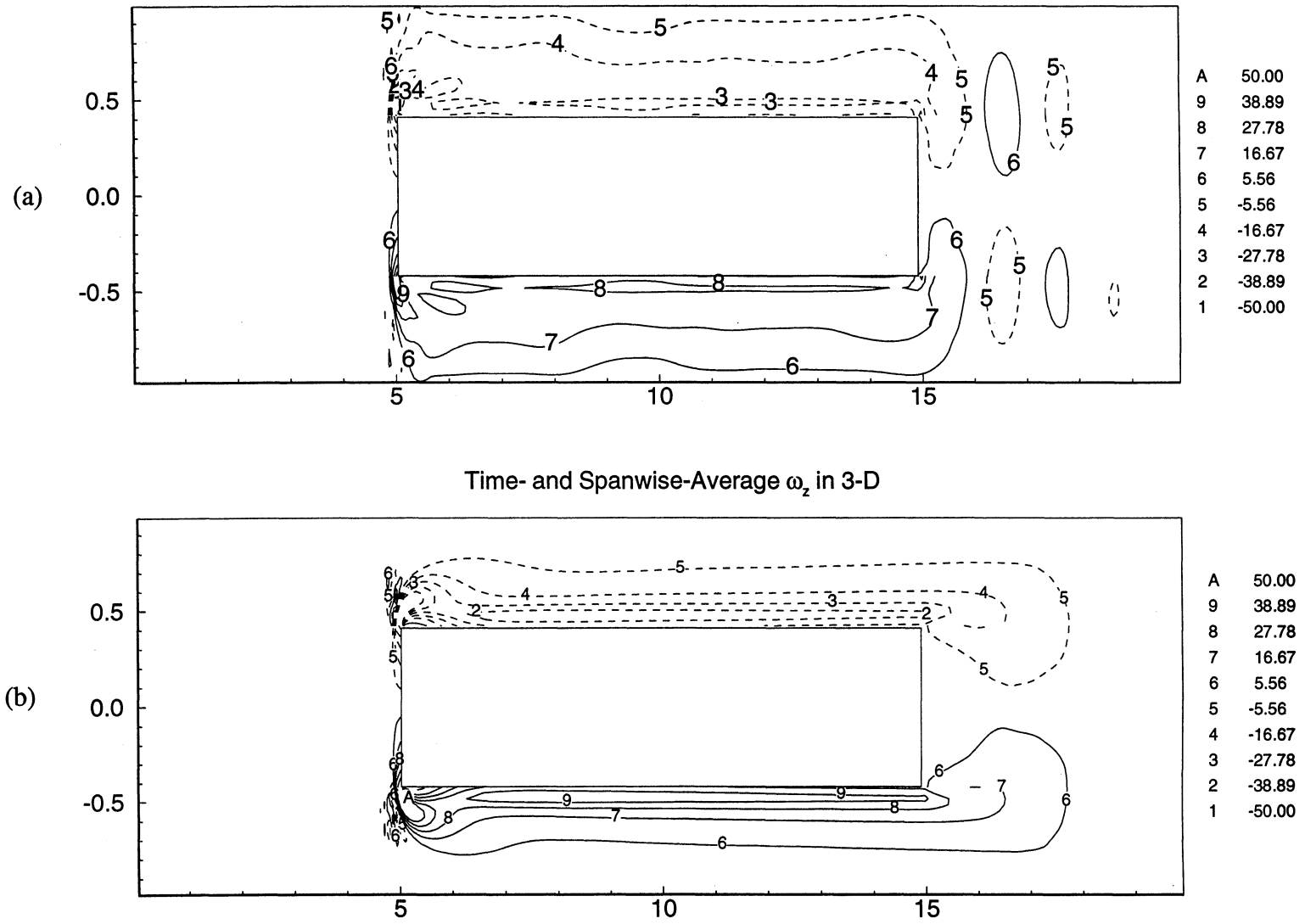

Figure 5.5 Time-averaged mean spanwise vorticity, $\overline{\omega}_z$, from: (a) two-dimensional simulation; (b) three-dimensional simulation.

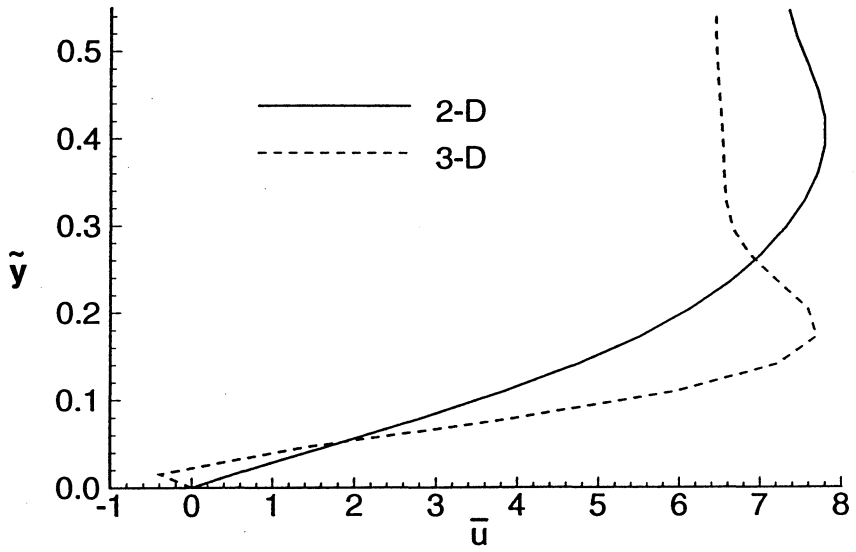

(a)

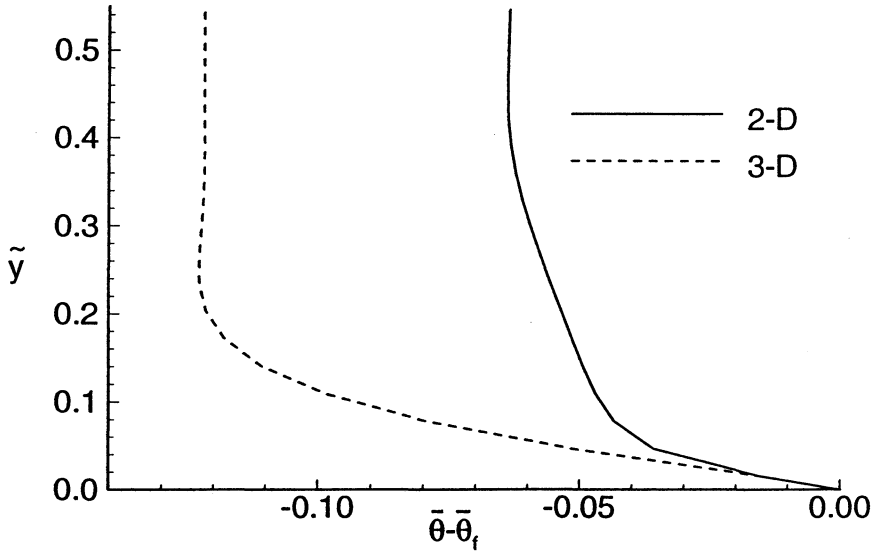

(b)

Figure 5.6 Comparison of time-averaged mean flow velocity and temperature difference profiles from two- and three-dimensional simulations at the leading edge of the fin top surface: (a) stream-wise velocity, $\bar{u}$; (b) mean temperature difference, $\bar{\theta} - \bar{\theta}_f$.

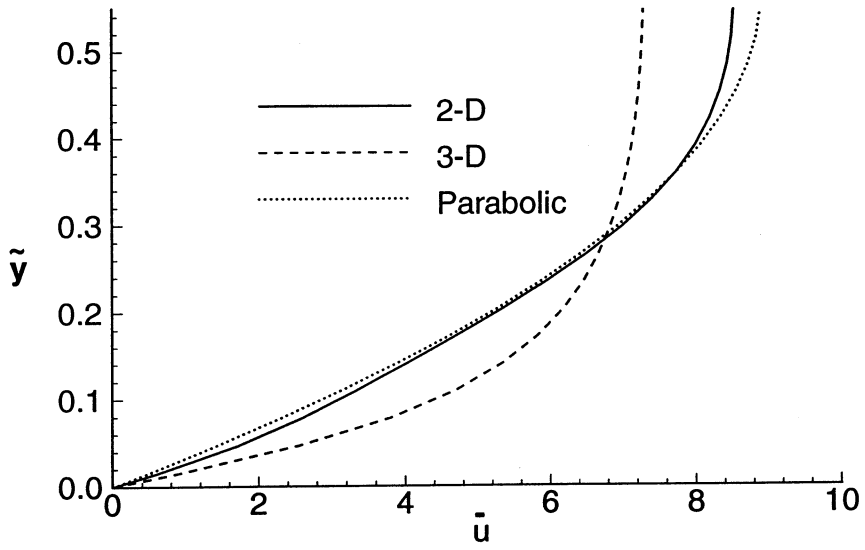

(a)

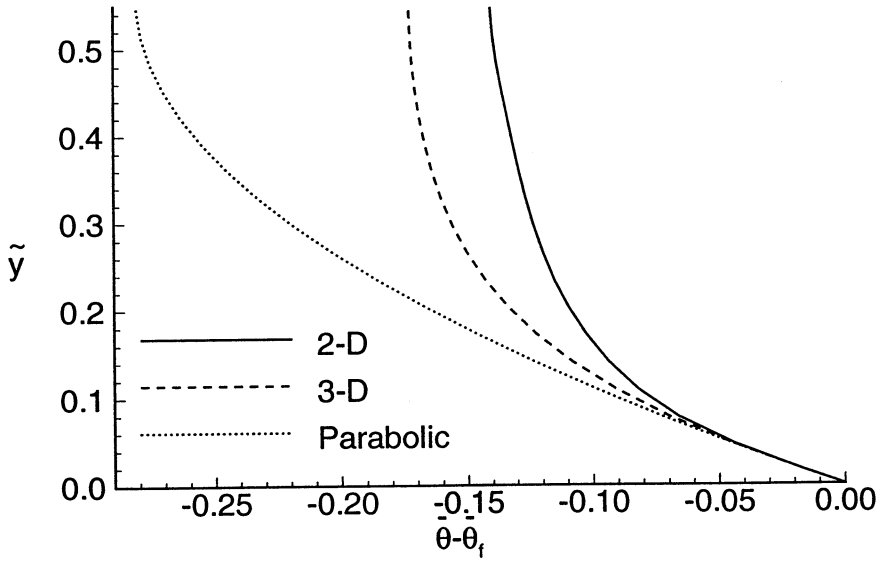

(b)

Figure 5.7 Comparison of time-averaged mean flow velocity and temperature difference profiles from two- and three-dimensional simulations at the middle point of the fin top surface to the fully developed channel flow: (a) streamwise velocity, $\bar{u}$; (b) mean temperature difference, $\bar{\theta} - \bar{\theta}_f$.

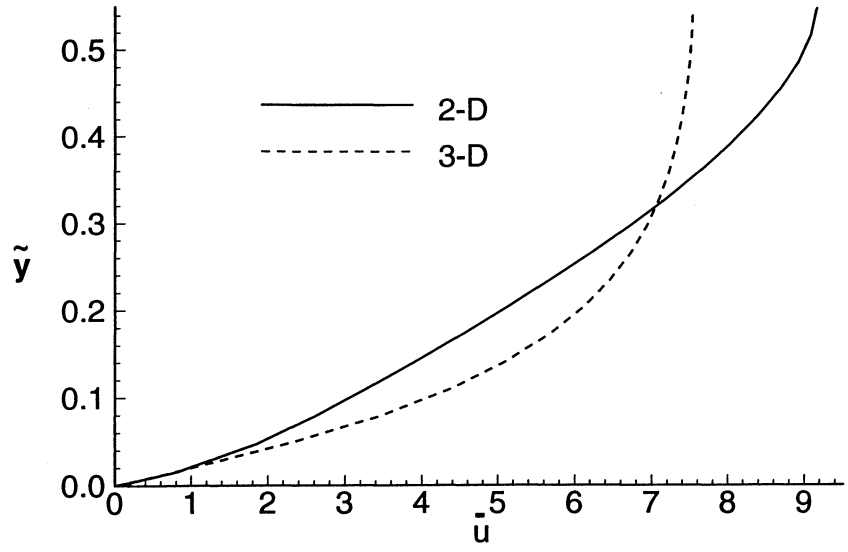

(a)

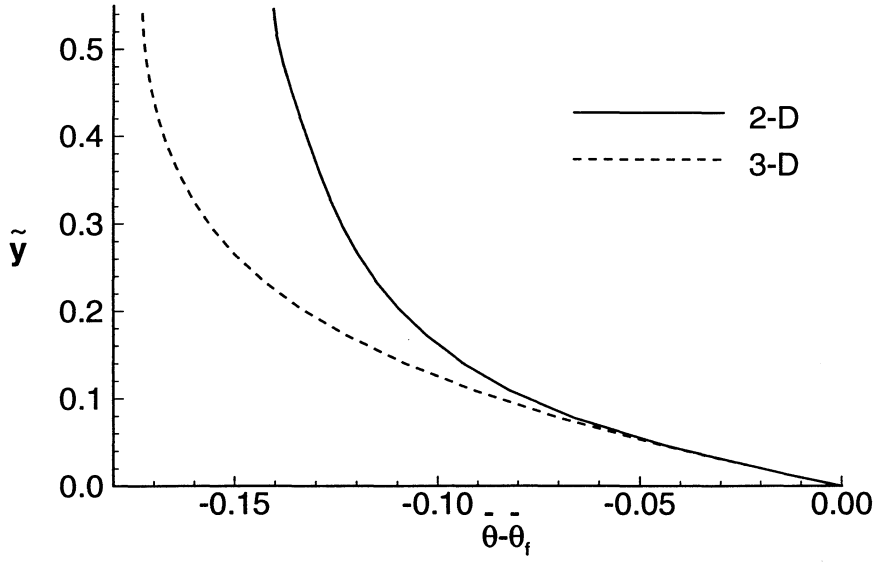

(b)

Figure 5.8 Comparison of time-averaged mean flow velocity and temperature difference profiles from two- and three-dimensional simulations at trailing edge of the fin top surface: (a) streamwise velocity, $\overline{u}$; (b) mean temperature difference, $\overline{\theta} - \overline{\theta}_f$.

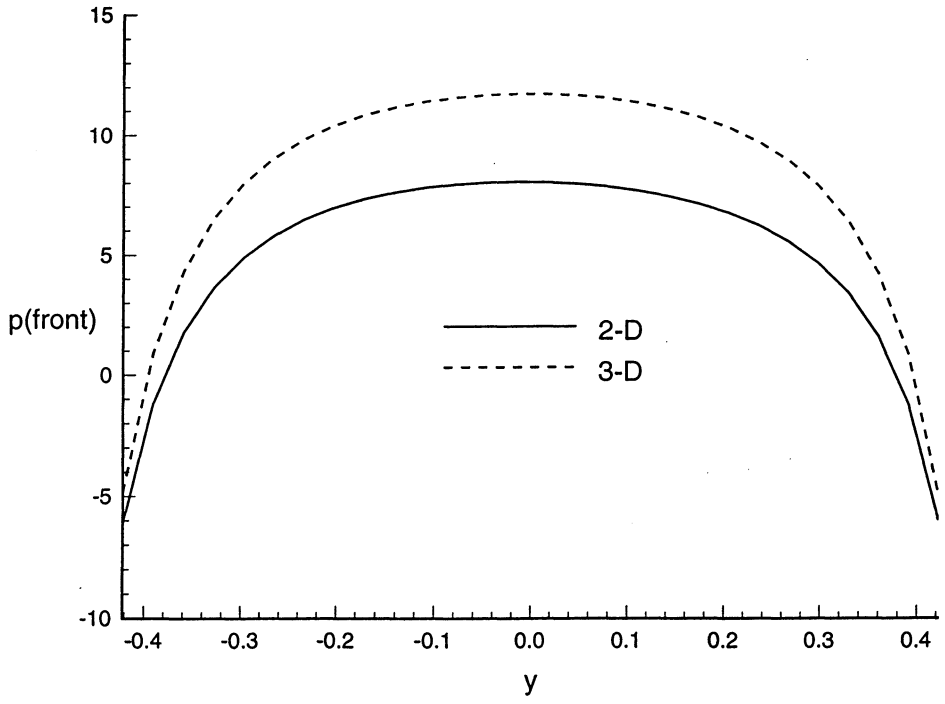

(a)

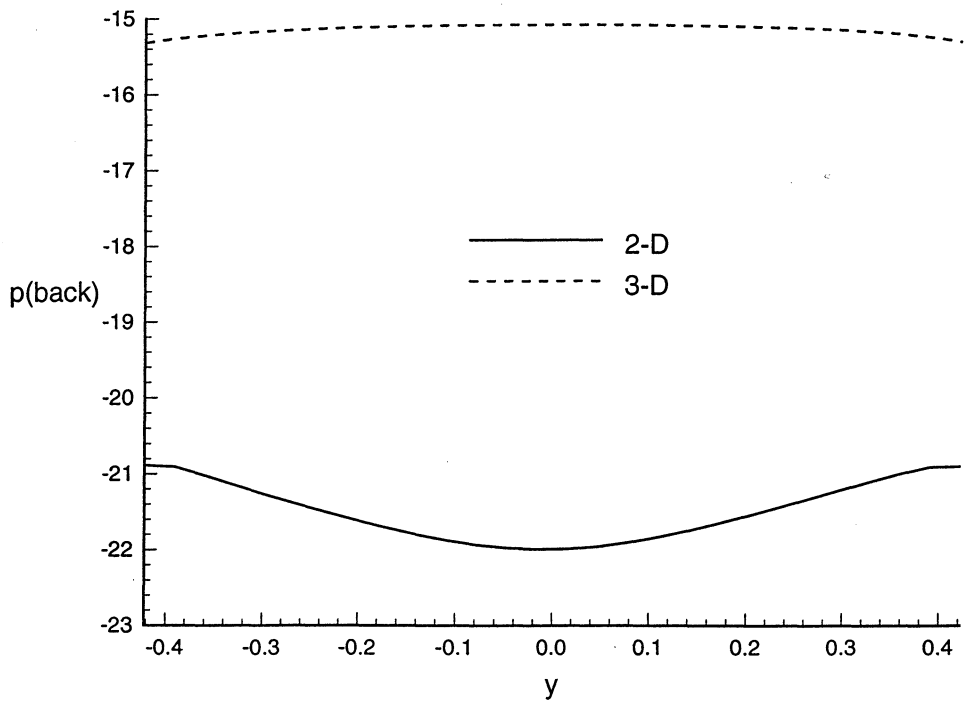

(b)

Figure 5.9 Comparison of time-averaged mean pressure distribution from two- and three-dimensional simulations at: (a) front fin surface; (b) back fin surface.

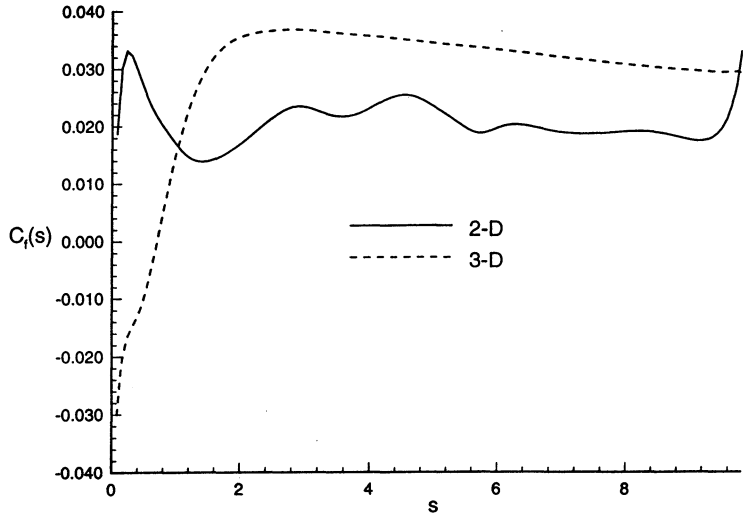

Figure 5.10 Comparison of time-averaged local skin friction factor distribution on top fin surface from two- and three-dimensional simulations.

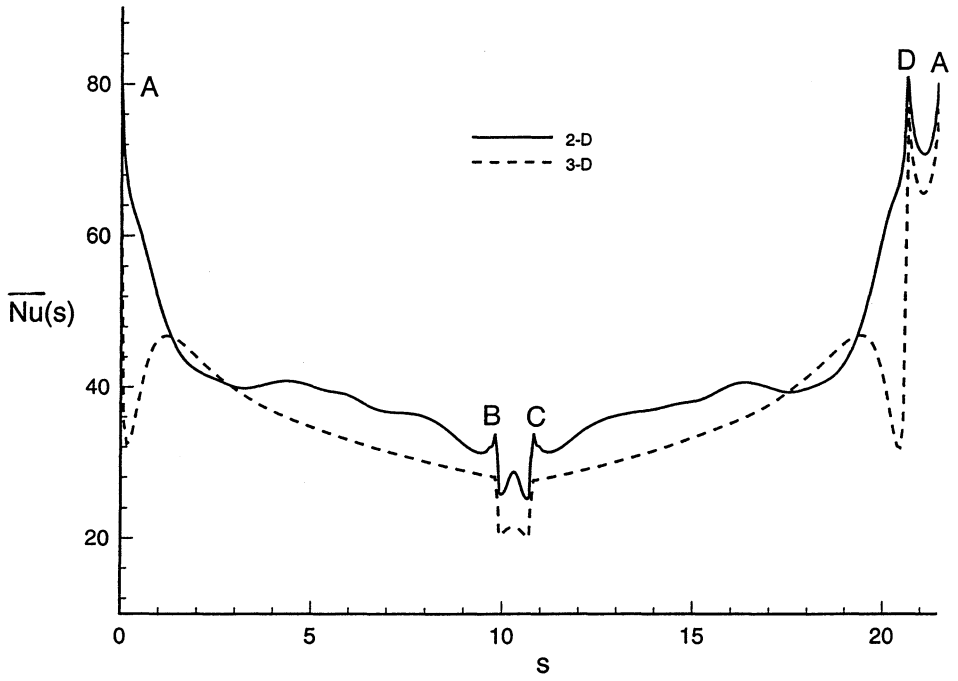

Figure 5.11 Comparison of time-averaged local Nusselt number distribution on top fin surface from two- and three-dimensional simulations.

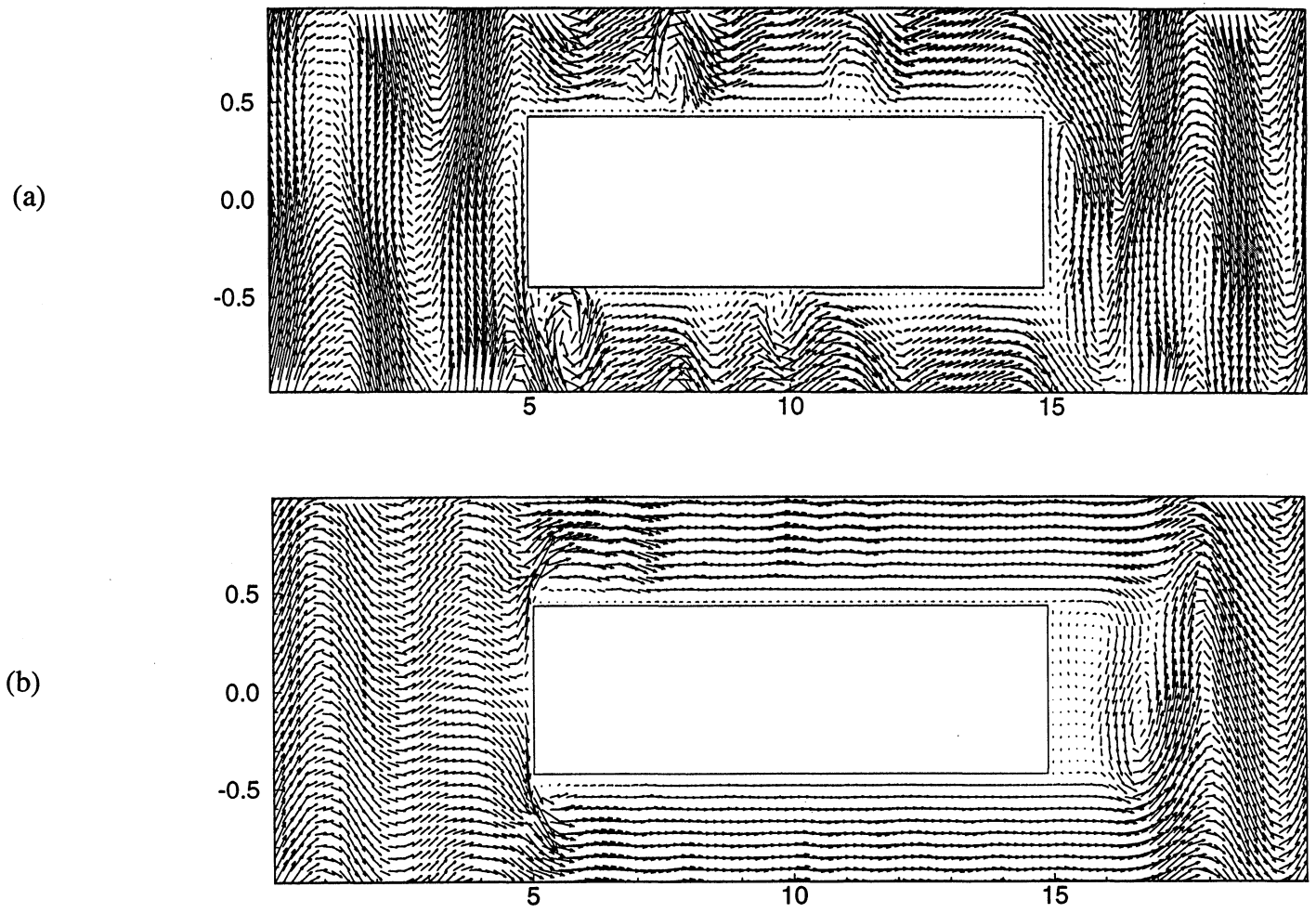

Figure 5.12 Instantaneous velocity vectors in *x*-*y* plane from: (a) two-dimensional simulation; (b) three-dimensional simulation, also averaged in spanwise, *z*, direction.

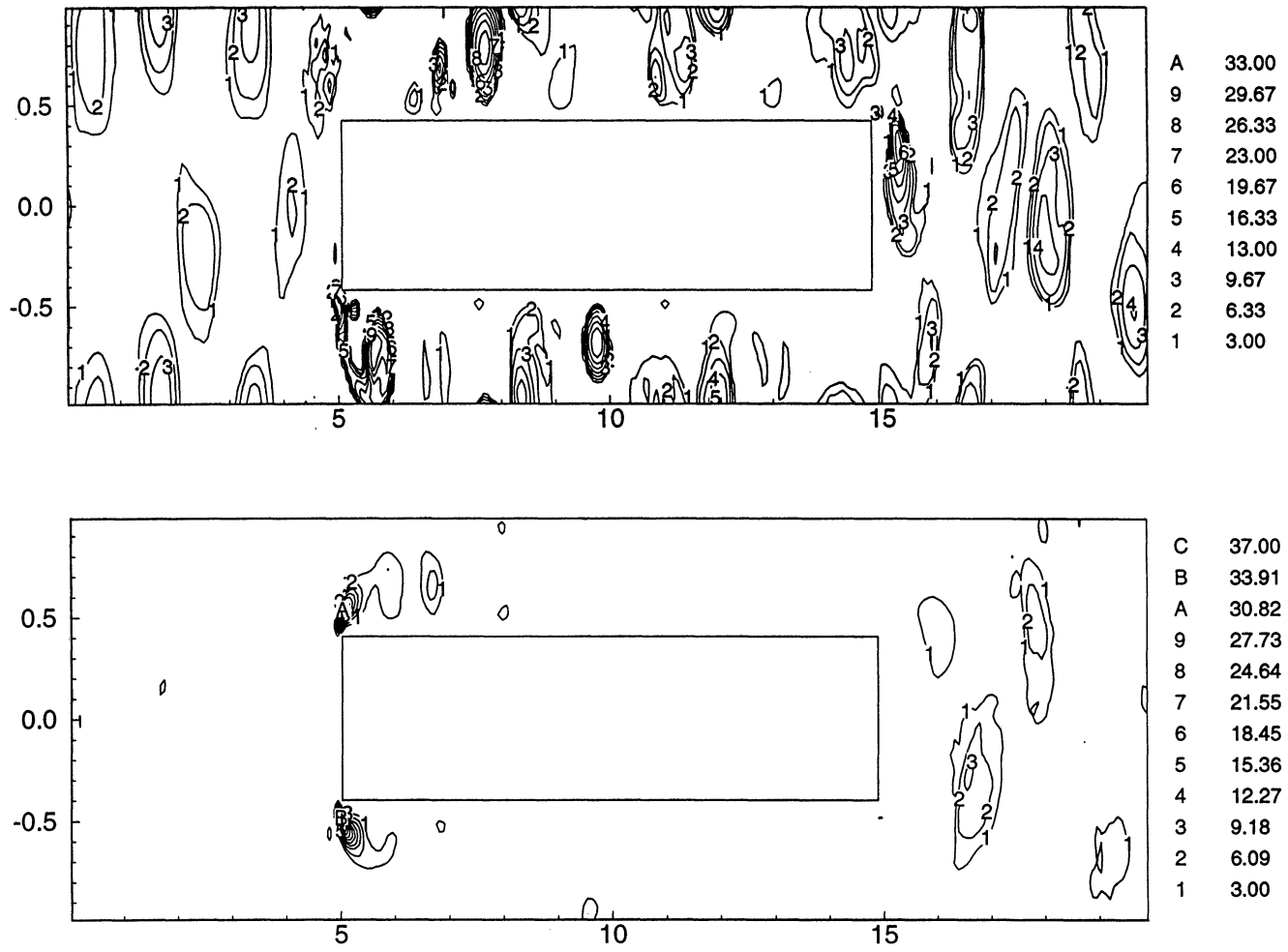

Figure 5.13 Contours of the imaginary part of eigenvalues of the velocity gradient tensor in x-y plane, λ_i, corresponding to the instantaneous velocity vectors shown in Figure 5.12: (a) two-dimensional simulation; (b) three-dimensional simulation, also averaged in spanwise, z, direction.

(a)

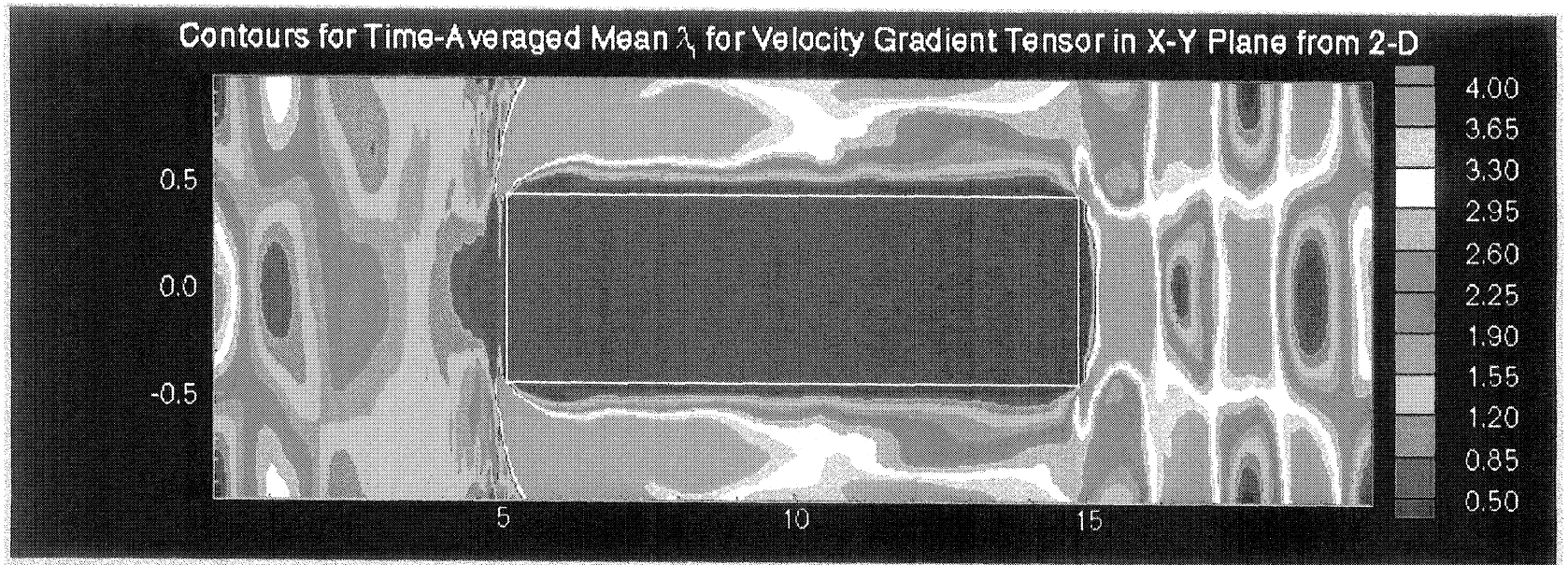

(b)

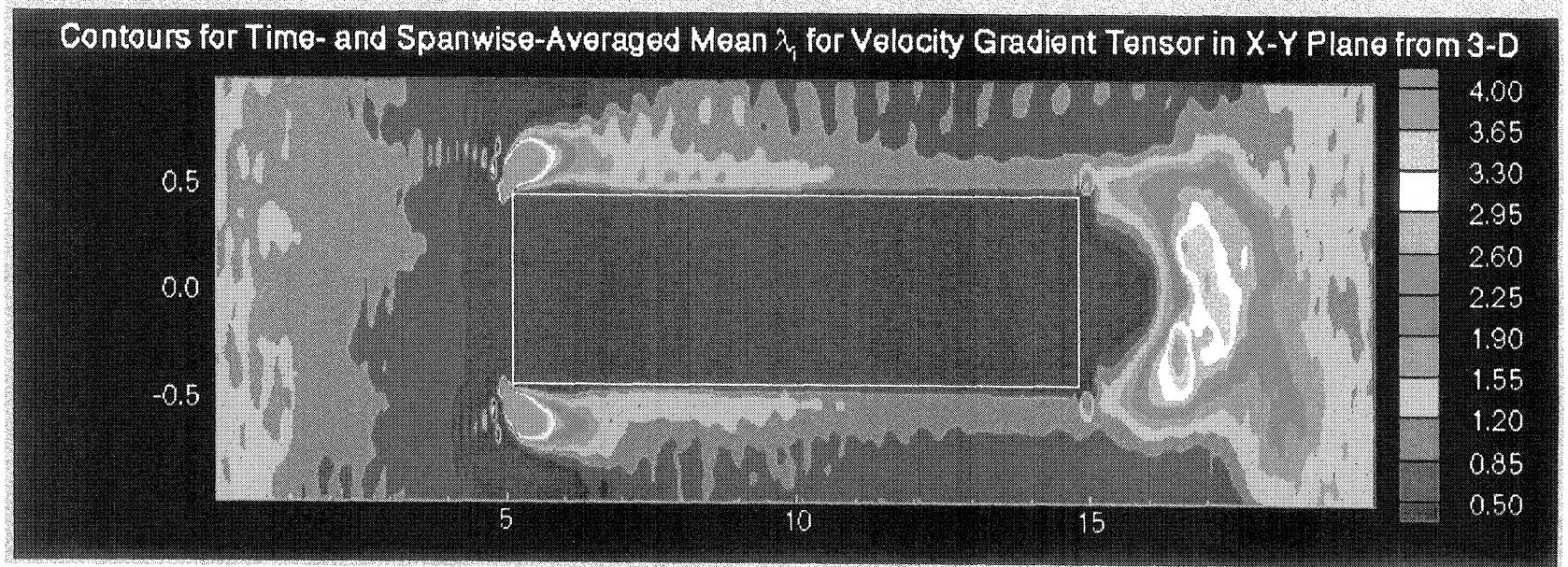

Figure 5.14 Contours of the time-averaged mean imaginary part of eigenvalues, λ_i, of the velocity gradient tensor in x-y plane.

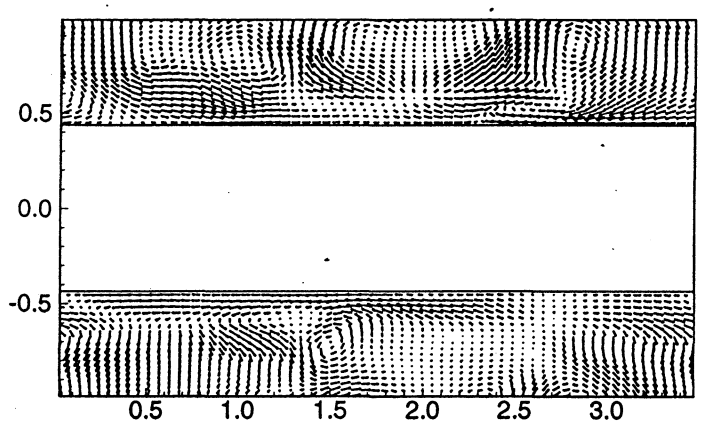

(a)

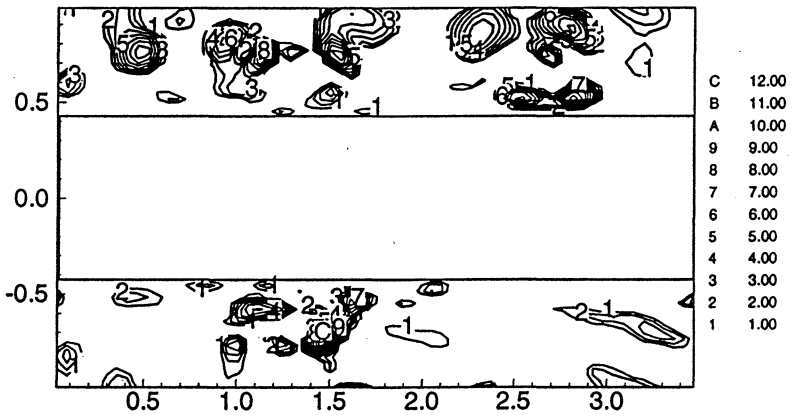

(b)

Figure 5.15 Instantaneous flow in *y*-*z* plane from the three-dimensional simulation at an earlier instance: (a) velocity vectors; (b) imaginary part of the eigenvalues, λ_i, of the velocity gradient tensor in *y*-*z* plane.

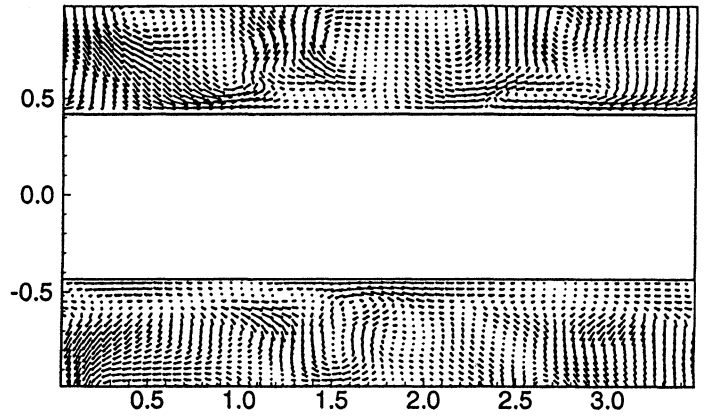

(a)

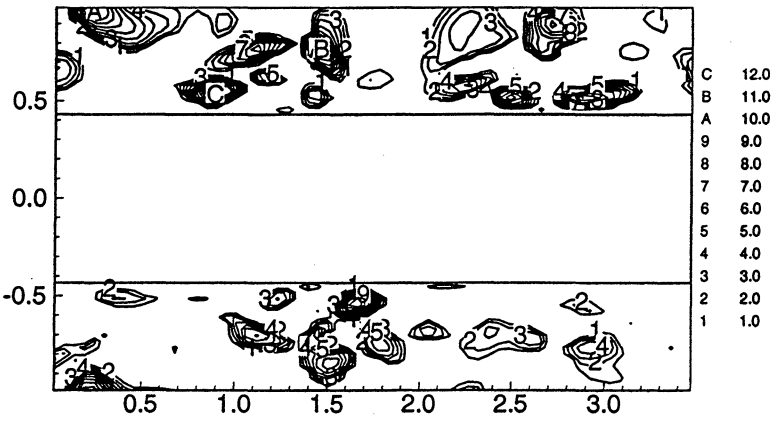

(b)

Figure 5.16 Instantaneous flow in *y-z* plane from the three-dimensional simulation at a later instance: (a) velocity vectors; (b) imaginary part of the eigenvalues, λ_i, of the velocity gradient tensor in *y-z* plane.

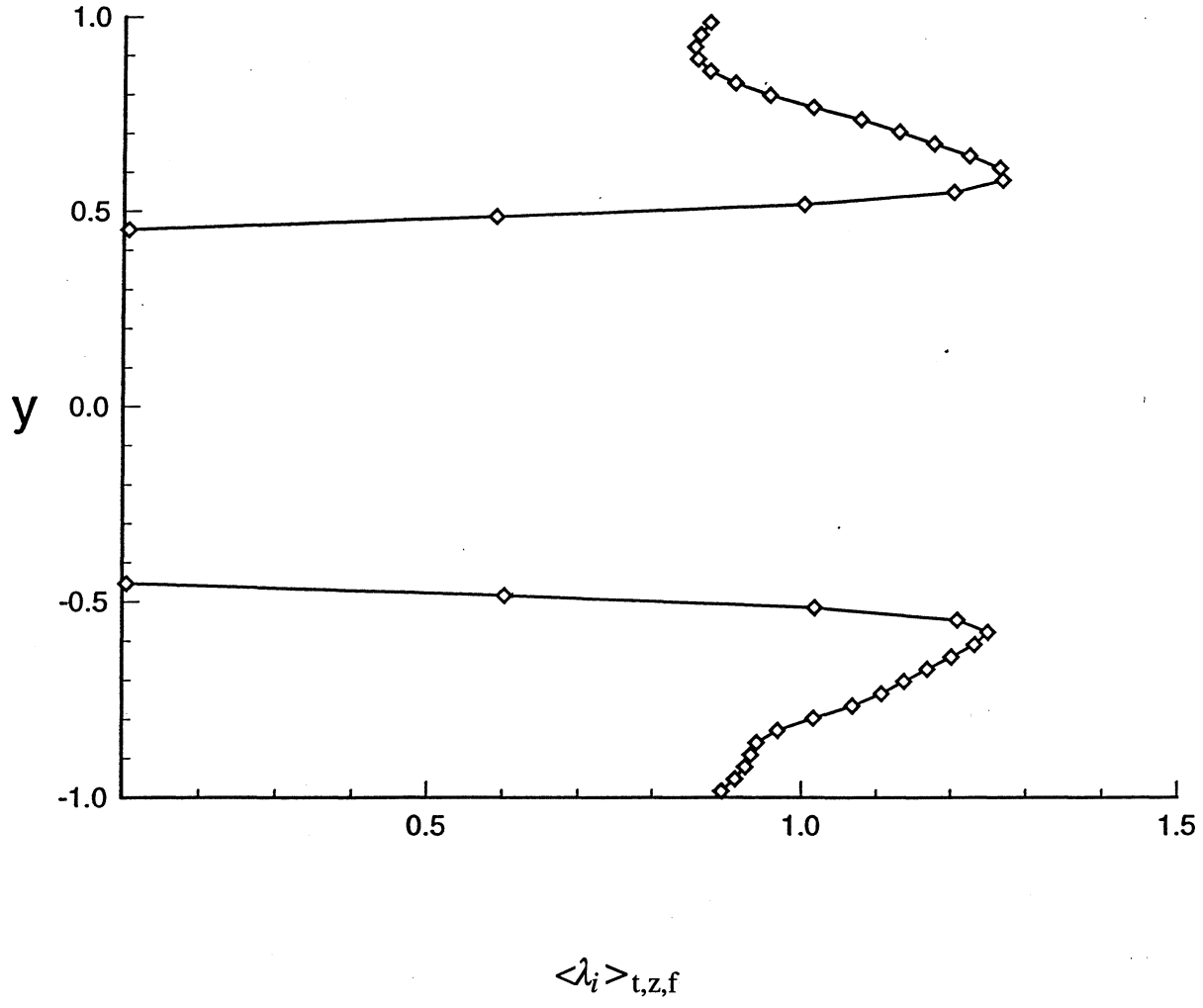

Figure 5.17 Profiles for time-, spanwise-averaged and also averaged over the fin length in stream-wise direction of the imaginary part of the eigenvalues, λ_i, of the velocity gradient tensor in y-z plane.

CHAPTER 6. FLOW AND HEAT TRANSFER IN LOUVERED FINS

Similar to parallel-plate fin heat exchanger design, louvered fin heat exchanger design has also been based on experimental data. However, due to the large number of geometrical parameters involved and the complexity of the geometries, researchers have been looking into analytical and numerical approaches, mainly because these approaches can provide detailed information about the heat transfer enhancement mechanisms as shown in simulations of flow and heat transfer in parallel-plate fin heat exchangers in the previous chapters. Unfortunately, most existing numerical studies [e.g. Achaichia and Cowell (1988b), Suga et al. (1989), Hiramatsu et al. (1990)] of flow over louvered fins have assumed steady laminar flow and thus are incapable of predicting unsteady flow separation, resulting in misleading predictions of the flow and the associated heat transfer enhancement mechanisms.

In the present study, numerical solution of the unsteady Navier-Stokes and energy equations will be used in studying flow and heat transfer over louvered fins. Thus, the unsteady flow physics will be captured and the associated heat transfer enhancement can be explored. In the following sections, preliminaries to the current simulation methodology will be discussed and then the calculated flow and heat transfer results will be presented.

Table 6.1 lists the Colburn j factor and friction factor for all the calculations performed. For the first two low Reynolds number cases, a semi-implicit time advancement scheme was used, in which the viscous terms were advanced in time using an implicit Crank-Nicolson method. This allowed much larger time steps than the other explicit time advancement scheme. The nominal grid size used in these simulations is *128x128*. In order to facilitate comparison with other results such as the Blasius solution over a flat plate, the Nusselt number, j factor and friction factor have been redefined based on the fin length, L^*. Here the Reynolds number, $Re_L = V^*L^*/\nu$, has also been defined based on fin length. In addition, the modified nondimensional reference temperature θ_{ref} has been defined differently based on the domain-averaged nondimensional modified temperature as

$$\theta_{ref} = \frac{\iint_D \theta dA}{\iint_D dA} \tag{6.1}$$

where D is the area of the computational domain excluding the fin area. Furthermore, in presenting the results in this chapter, it is useful to introduce a schematic of the geometry detailing the lines along which some of the results will be presented. This is shown in Figure 6.1.

The general flow features observed in the simulations will be discussed first. The flow was observed to be steady up to $Re_L = 782$. From $Re_L = 0.7$ to 43, no flow separation was observed on the fin surface. At $Re_L = 162$, the flow was found to separate at the trailing edge of the fin, resulting in a steady recirculating wake. As the Reynolds number was increased further beyond $Re_L = 782$, the flow became unsteady with vortex shedding from the leading edge on the back side. Figure 6.2 shows the steady flow streamlines for Reynolds numbers of $Re_L = 0.7, 43, 455$ and the time-averaged mean flow streamlines at $Re_L = 1103$, and Figure 6.3 shows the corresponding temperature contours. At the Reynolds number of 0.7 and 43, the streamlines are predominantly parallel to the streamwise direction away from the fin surface. This trend is observed to change as the Reynolds number increases to $Re_L = 455$ and 1103 when the streamlines are nearly aligned to the louver direction. Figure 6.4 plots the flow angle, $\alpha = tan^{-1}(v/u)$, at three streamwise locations (lines a, b and c in Figure 6.1) for $Re_L = 0.7$ and 455. At $Re_L = 0.7$, it is observed that the flow entering the louver space at line a is predominantly aligned to the streamwise direction in the unobstructed space (between lines ii and iii in Figure 6.1) between the louvers. As the flow travels further downstream between the louvers to line b, it is nearly aligned to the louver direction. By the time the flow approaches line c, the flow is again predominantly aligned with the streamwise direction in the unobstructed space between the louvers. At $Re_L = 455$, it is observed that the flow is predominantly aligned along the louver direction, except for some local perturbation caused by the flow over the leading edge of the louver at line a. The predominant flow directions at low and high Reynolds numbers are also reflected in the temperatures contours shown in Figure 6.3. At $Re_L = 0.7$ and 43, the temperature contours away from the fin surface are nearly parallel to the streamwise direction with very thick thermal boundary layers. As the Reynolds number increases further, the thermal boundary layers are much

thinner and are aligned to the louver direction. In addition at $Re_L = 0.7$, the wake behind the trailing edge of the previous row can be seen to completely block the boundary layer restarting at the forward side leading edge of the following row of fins. Thus, the thermal boundary layer on the forward side appears to be thicker than that on the back side of the fin. As the Reynolds number is increased, the wake behind the previous row appears to be moved away from the boundary layer on the forward side of the fin. Now the boundary layer restart and growth on the forward side appear normal but still remains thicker than that on the back side.

The difference in flow direction at low and high Reynolds numbers has been observed in flow visualization studies by previous researchers [Achaichia and Cowell (1988) and Webb and Trauger (1991)] in louvered fin geometries with additional deflections fins. It has been hypothesized that at high Reynolds numbers the flow is predominantly parallel to the louvers and the effective heat transfer has the characteristics of flow over a flat plate. But this effective heat transfer configuration changes from "flat plate" to "duct flow" as the Reynolds number decreases. Figure 6.5(a) shows the cross-section through a louver array indicating these possible flow directions [Achaichai and Cowell (1988)]. Based on flow visualization results, the above hypothesis has been made regarding the flow direction in louvered fin arrays: the flow is considered fin directed at low Reynolds numbers and louver directed at high Reynolds number. The fin directed flow is considered to be "duct flow" and the Stanton number curve is plotted in Figure 6.5(b) for the "duct flow" with duct spacing of the fin pitch (L_y* in Figure 2.2). However, this effective heat transfer over "duct flow" at the low Reynolds numbers assumes the louvered fins contribute to heat transfer by forming imaginary bounding surfaces (shown by the dotted lines in Figure 6.1) of the "duct". In large fin arrays, this assumption may seem to be a reasonable estimate from a macroscopic point of view. However, the fact that the louvered fins provide the heat transfer surface area, would make it imperative that even at low Reynolds numbers the flow between louvers is what determines the heat transfer. Hence, in order to investigate this apparent contradictory nature of the "duct flow" analogy, flow between louvers will be investigated.

Profiles for the projected velocity, $u_p = u\cos(-25°) + v\sin(-25°)$, in the louver direction have been plotted along line 1, line 2 and line 3 as shown in Figure 6.6, as a function of distance away

from the back side of fin III, $\tilde{y}$, at three different Reynolds numbers: $Re_L = 0.7, 455$ and 1103. At the lowest Reynolds number of 0.7, it is discovered that these velocity profiles are similar to the duct flow profiles with a duct spacing of $6.25H^*$ along line 1 and line 2, and with a duct spacing of $9.2H^*$ along line 3, but somewhat skewed as shown in Figure 6.6(a). As the Reynolds number increases, the mean flow becomes nearly parallel to the louvers. The profiles for the projected velocity at $Re_L = 455$ as shown in Figure 6.6(b) have the characteristic of flow over a flat plate, with additional effect of boundary layer restart. In the unsteady flow regime, the time averaged mean flow is also nearly parallel to the louvers. The velocity profiles become fully developed quickly as shown in Figure 6.6(c) at $Re_L = 1103$. The corresponding temperature difference profiles, $\theta - \theta_f$, along the three lines have also been plotted in Figure 6.7 for $Re_L = 0.7, 455$ and 1103. Here θ_f is the fin surface temperature on the back side of fin III (Figure 6.1). At the lowest Reynolds number of $Re_L = 0.7$, the small temperature difference near $\tilde{y} = 0$ indicates a higher heat transfer coefficient on the back side than the forward side along line 1. The temperature differences become about the same along line 2 and line 3, which shows that the flow becomes fully developed similar to the channel flow with a channel height of $6.25H^*$. The distortion of the profiles from the parabolic profiles can be attributed to the effect of plug flow along the axial direction. At the higher Reynolds numbers, the difference in the temperature difference between the back and forward sides are not seen to be significant.

The normalized velocity profiles and temperature difference at the Reynolds number of 0.7 have been plotted with those for the fully developed channel flow with a channel height of $6.25H^*$ shown in Figure 6.8. The similarity between the velocity profiles of fully developed channel flow and that of the current simulation at the low Reynolds number 0.7 can be clearly seen. Figure 6.9 shows the calculated Nusselt number in comparison with the theoretical results of channel flow and flow over a flat plate. Here solutions for duct flows in the imaginary duct between lines i, ii, iii and iv with a duct spacing of $L_y - L\sin\theta - b\cos\theta = 4.61H^*$ and the physical duct between louvers with duct spacing of $6.25H^*$ are plotted. The calculated Nusselt number from the present study lie between the two duct flow solutions up to the Reynolds number of approximately 40. At the very low Reynolds number, the good agreement between the calculated Nusselt number and that of the physical duct flow between louvers indicates that at very low Reynolds numbers the heat transfer configuration can be

better approximated by the flow over the physical duct between louvers than the flow over the imaginary duct. The deviation of the current calculated Nusselt number curve from the channel flow solutions as the Reynolds number increases indicates that the mean flow direction is changing from the axial direction to the louver passage direction. The apparent agreement between the current calculated Nusselt number with that of the flow over a flat plate over the Reynolds number range of *300* to *850* also verifies that the flat plate is the effective heat transfer configuration. As the Reynolds number increases further, the current calculated Nusselt number deviates from that of the flat plate solution which is due to the presence of flow unsteadiness.

The local Nusselt number distributions along the fin surface have been plotted in Figure 6.10 for different Reynolds numbers: Re_L = *43, 455* and *1103,* and the overall Nusselt number on the forward and back sides of the fin for all the Reynolds numbers have been determined separately and are plotted in Figure 6.11. At the low Reynolds number of *43*, the Nusselt number of the back side (marked **A** to **B** in Figure 6.1) of the fin is higher than that on the forward side (marked **C** to **D** in Figure 6.1). The peaks near the leading edges are due to the effect of boundary layer restart. The increase in local Nusselt number near the trailing edges is due to the acceleration of the flow around the trailing edge. As the Reynolds number increases to approximately *100*, the Nusselt number of the forward side exceeds that of the back side as shown in Figure 6.11. This continues to be true in the unsteady flow regime. The Nusselt numbers on the forward and back sides of the fin, shown in Figure 6.11, are similar to those in the experiments of Lee (1986) of louvered fins in the range of Reynolds number, based on hydraulic diameter, between *350* and *5000.* This Reynolds number range is equivalent to a Reynolds number range based on louver length of *142* and *2035*. In the experiments of Lee (1986), the Nusselt number of the forward side was higher than that of the back side for all Reynolds numbers he tested. This agrees well with our results shown in Figure 6.11.

In the unsteady flow regime, vortex shedding is observed to start from the leading edge on the back side and a recirculation zone in the time-averaged mean flow is observed on the back side of the fin. Figure 6.12 shows the instantaneous streamlines and corresponding temperature contours at a Reynolds number of *1103*: on the back side of the fin, sharp temperature gradients are observed at x = *3* and *6* which correspond to the downstream sides of two vortices. The corresponding instan-

taneous local Nusselt number distribution along the fin surface has been plotted in Figure 6.13 along with the time-averaged local Nusselt number distribution. A sudden change in the slope of the curves in the time-averaged mean Nusselt number distribution along both the back side and forward side have been noticed and it is attributed to the time-averaged effect of the unsteady vortex shedding. The instantaneous local Nusselt number distribution is closely related to the unsteady flow characteristics. It is observed that the local enhancement in heat transfer at $s = 2$ and 5.3 correspond to the downstream side of two strong vortices rolling on the back side at $x = 2.4$ and 5.4, as shown in Figure 6.12. Another local enhancement in heat transfer at s = 9 corresponds to the downstream side of the vortex rolling on the forward side at $x = 4.6$. The local heat transfer enhancement at the downstream side of a vortex is due to the effect of the vortex bringing fresh fluid from the freestream towards the fin surface, and a drop in local Nusselt number upstream of a vortex is due to the effect of fluid being ejected away from the fin. The effect of these vortices is to increase the overall heat transfer as observed in the flattening of the time-averaged local Nusselt number distribution.

Table 6.1: Summary of calculations performed for louvered fins (grid size *128x128*).

Re_τ	Re_L	Re	j	f
0.2	*0.7*	*2*	*8.6352*	*11.6114*
0.5	*4.1*	*9.4*	*1.4197*	*1.9418*
2	*43*	*97*	*0.2284*	*0.2907*
5	*162*	*368*	*0.0920*	*0.1256*
10	*455*	*1033*	*0.0427*	*0.0638*
15	*782*	*1778*	*0.0310*	*0.0485*
17	*927*	*2108*	*0.0262*	*0.0443*
20	*1103*	*2507*	*0.0249*	*0.0434*

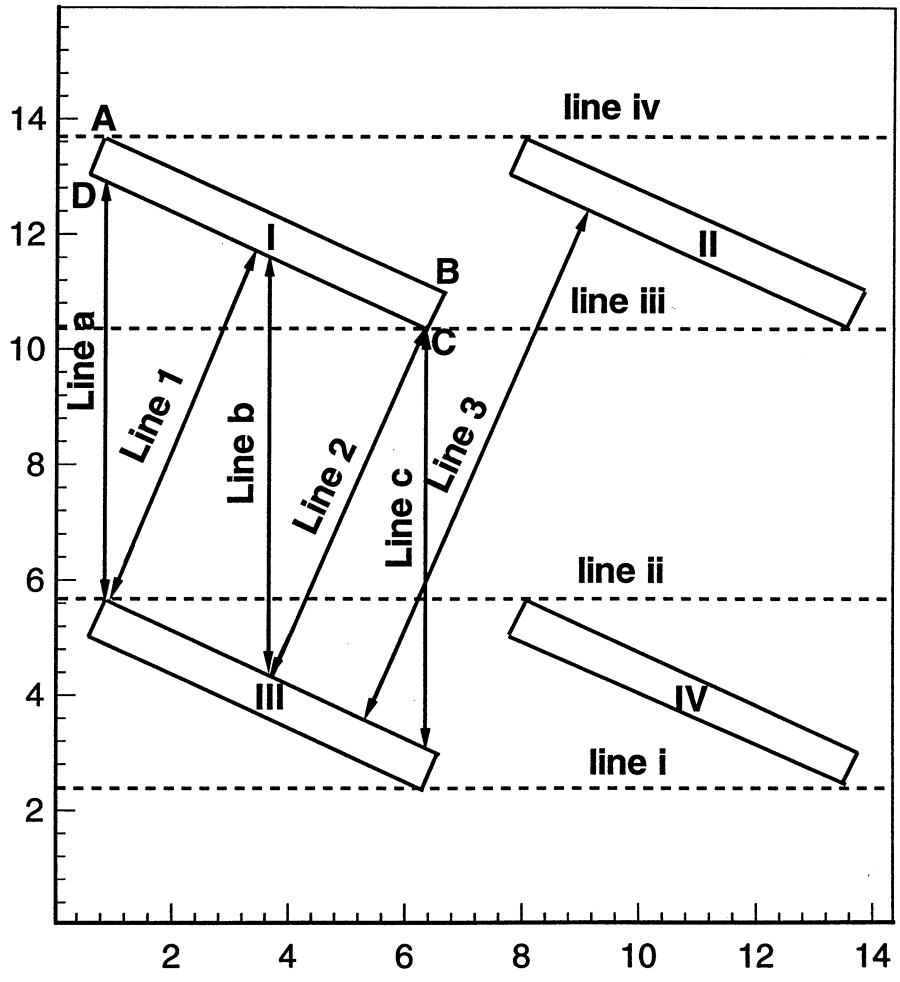

Figure 6.1 Schematic of the louvered fin geometry detailing lines along which some results will be shown.

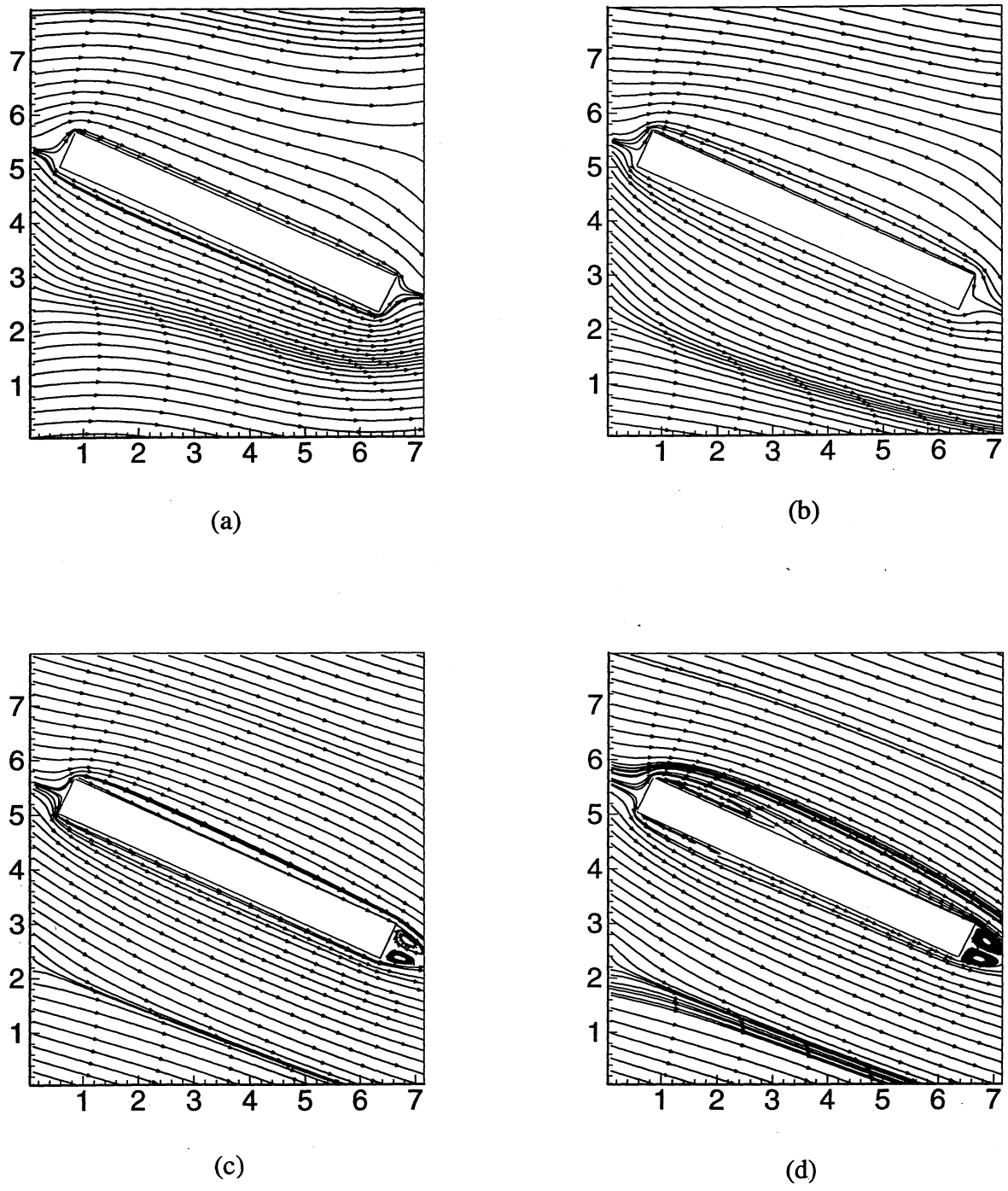

Figure 6.2 Streamlines for: (a) steady flow at $Re_L = 0.7$; (b) steady flow at $Re_L = 43$; (c) steady flow at $Re_L = 455$; (d) time-averaged mean flow at $Re_L = 1103$.

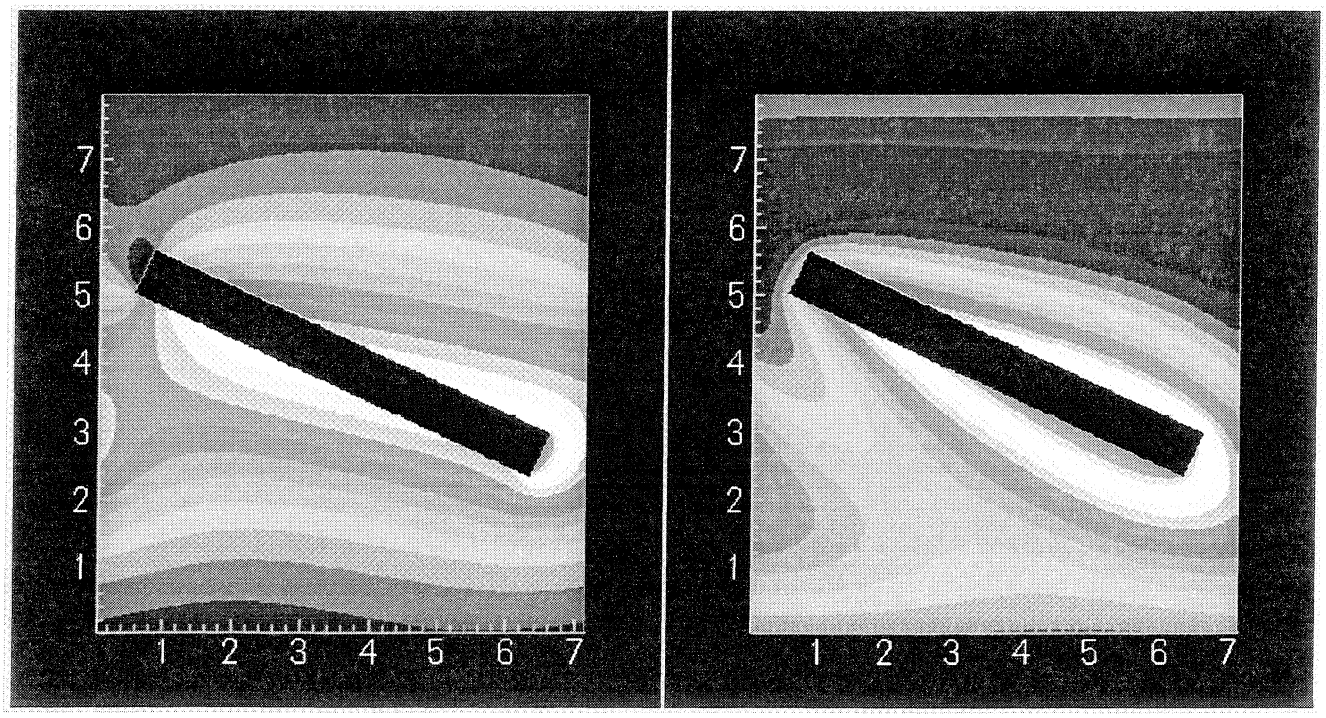

(a) (b)

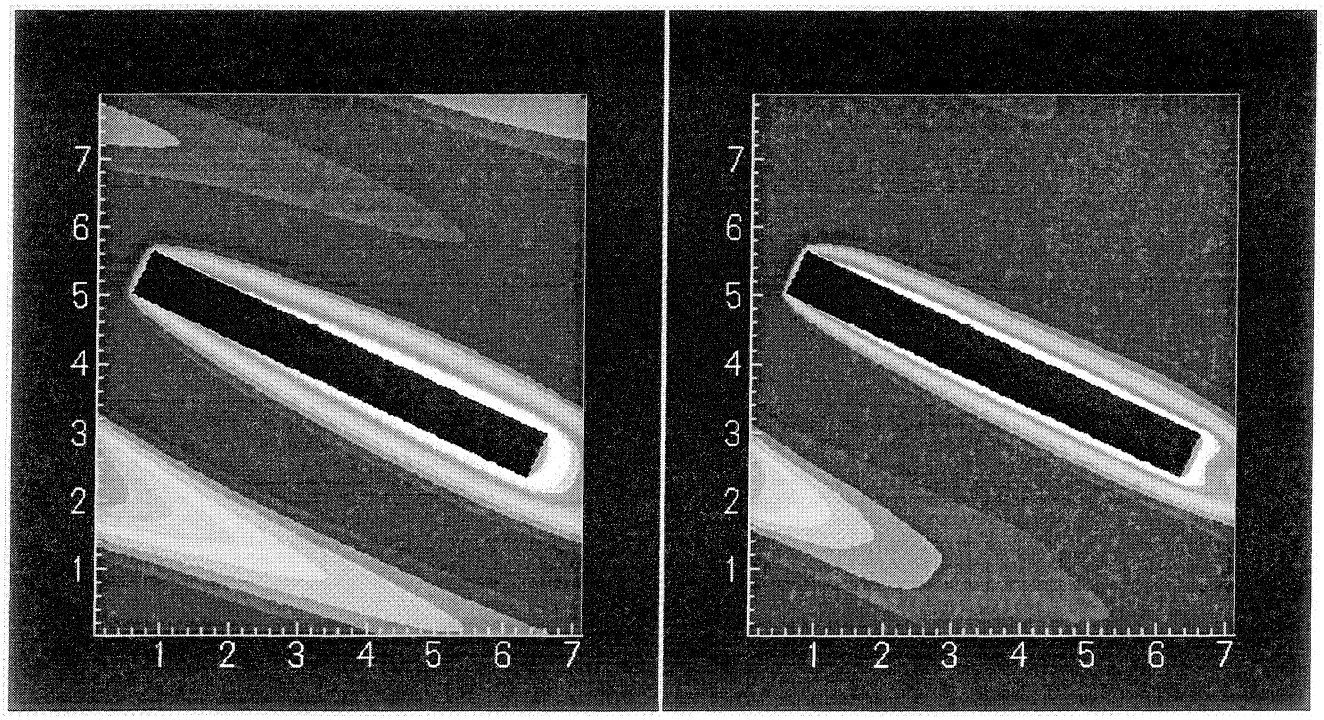

(c) (d)

Figure 6.3 Temperature contours corresponding to streamlines shown in Figure 6.2 for: (a) steady flow at $Re_L = 0.7$; (b) steady flow at $Re_L = 43$; (c) steady flow at $Re_L = 455$; (d) time-averaged mean flow at $Re_L = 1103$.

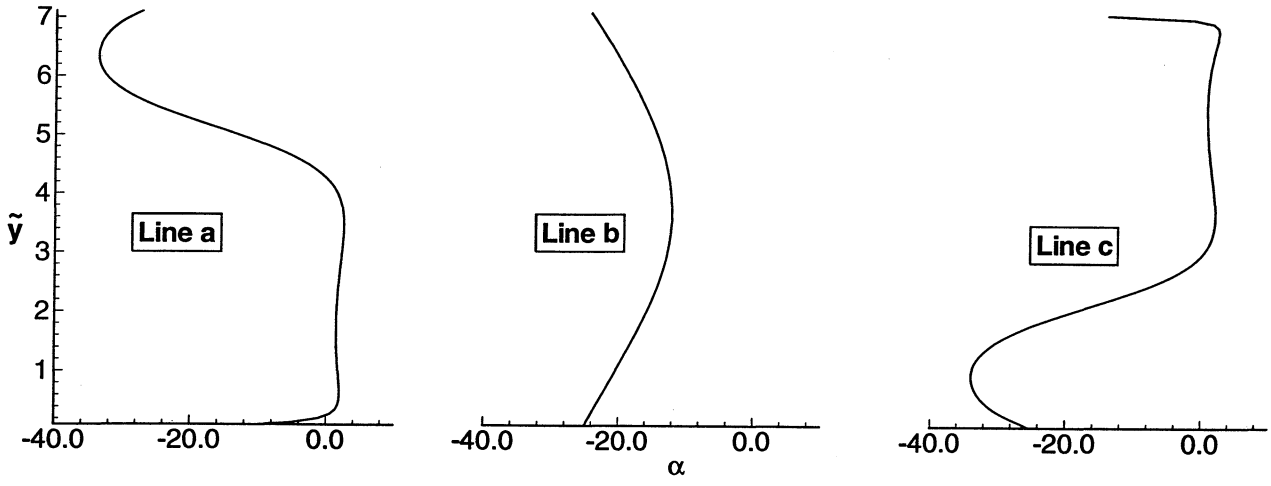

(a)

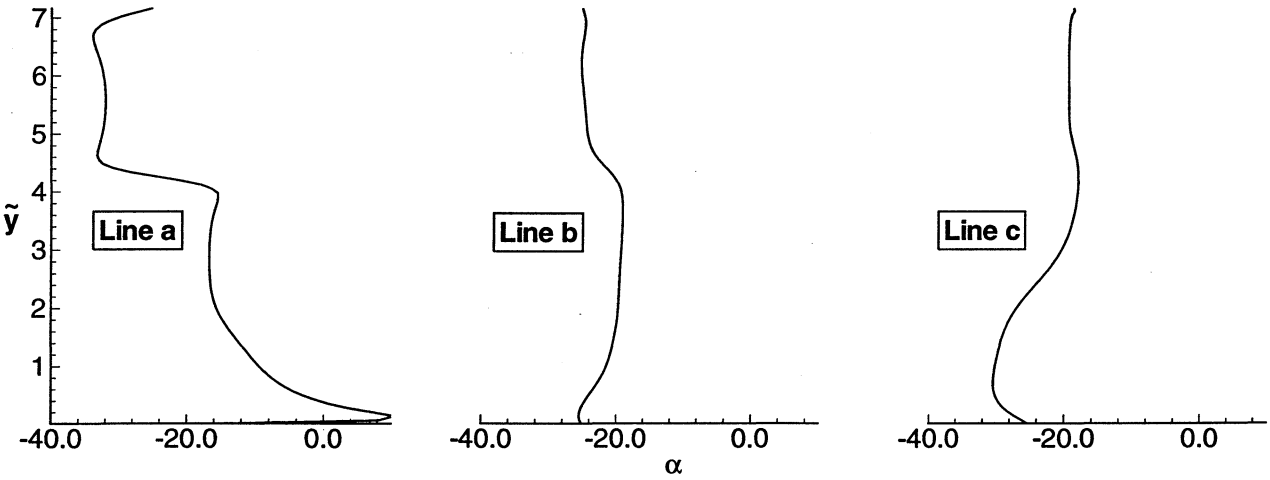

(b)

Figure 6.4 Profiles of flow angle, α, along lines a, b and c shown in Figure 6.1 at two different Reynolds numbers: (a) $Re_L = 0.7$; (b) $Re_L = 455$.

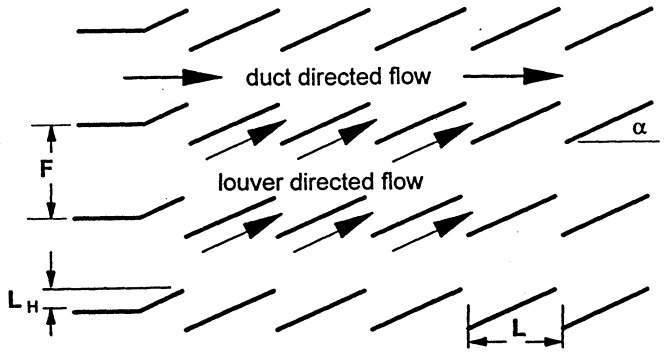

(a)

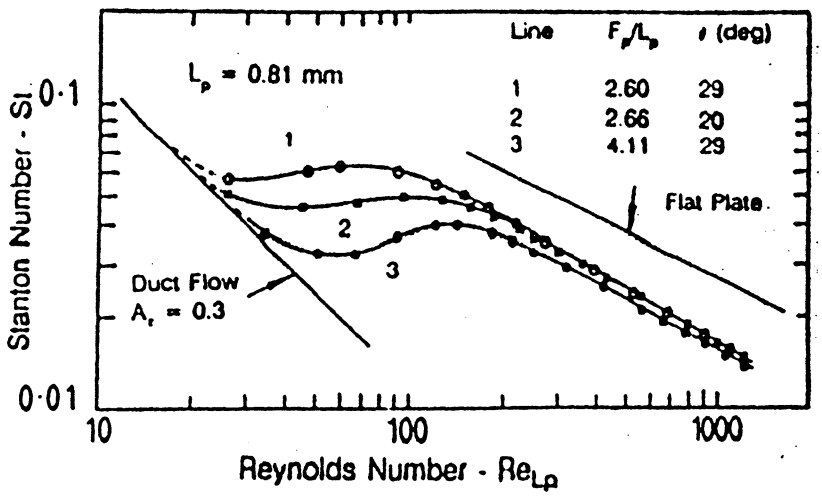

(b)

Figure 6.5 Duct flow hypothesis: (a) section through louver array indicating possible flow directions; (b) Stanton number curves indicating the possibility of duct flow at low Reynolds numbers, Achaichia and Cowell (1988).

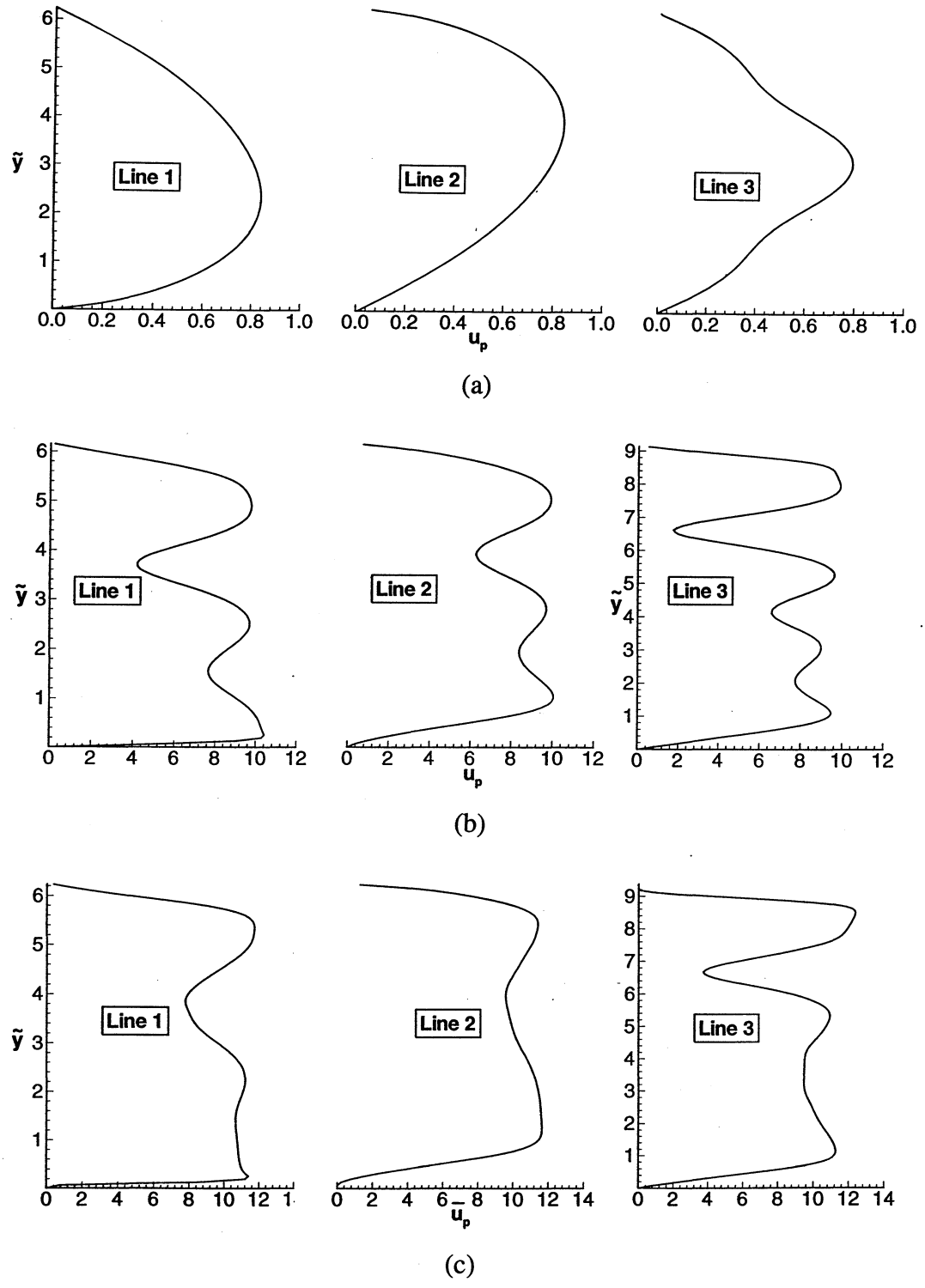

Figure 6.6 Profiles of projected velocity, u_p, along lines 1, 2 and 3 shown in Figure 6.1 for flows in different flow regimes: (a) steady flow at $Re_L = 0.7$; (b) steady flow at $Re_L = 455$; (c) time-averaged mean flow at $Re_L = 1103$.

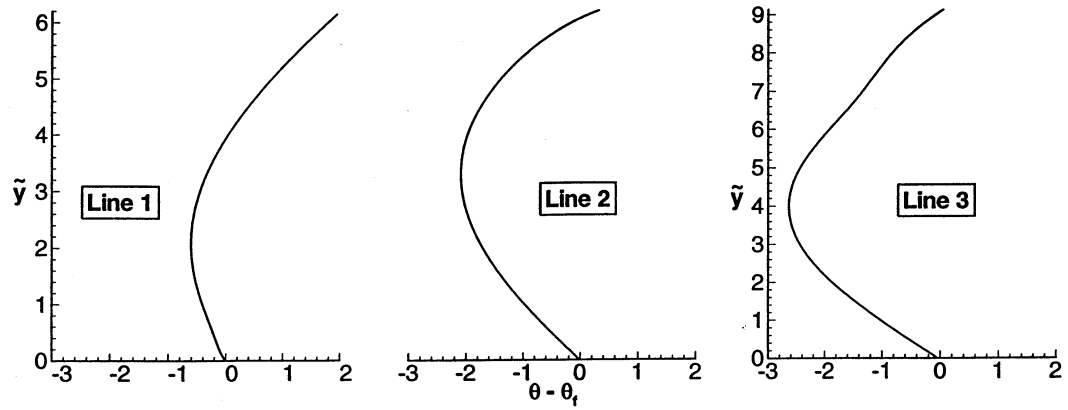

(a)

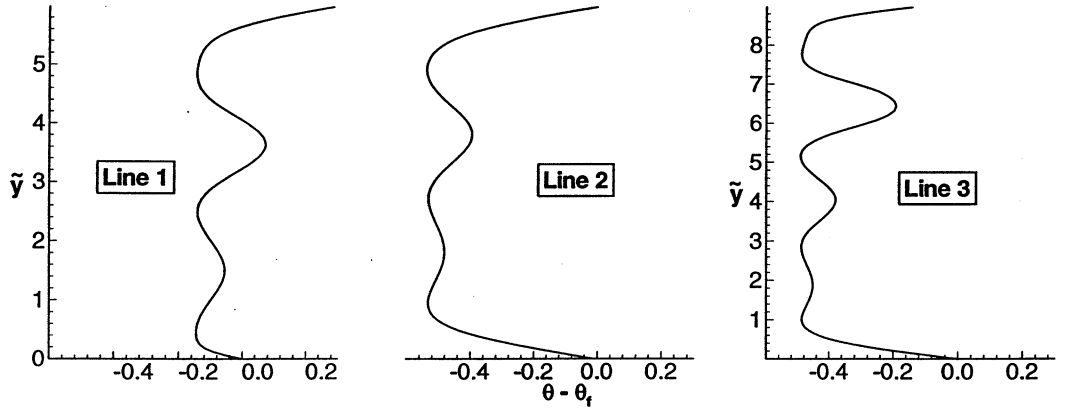

(b)

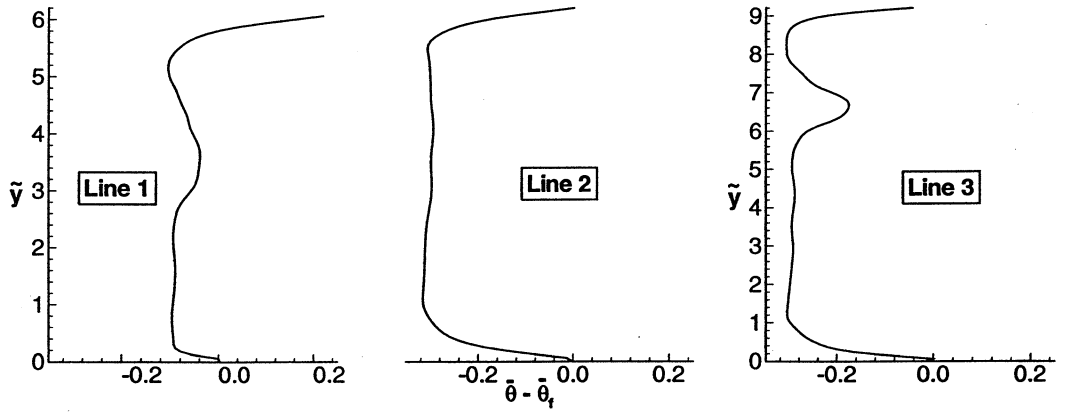

(c)

Figure 6.7 Profiles of temperature difference, $\theta - \theta_f$, along lines 1, 2 and 3 shown in Figure 6.1 for flows in different flow regimes: (a) steady flow at $Re_L = 0.7$; (b) steady flow at $Re_L = 455$; (c) time-averaged mean flow at $Re_L = 1103$.

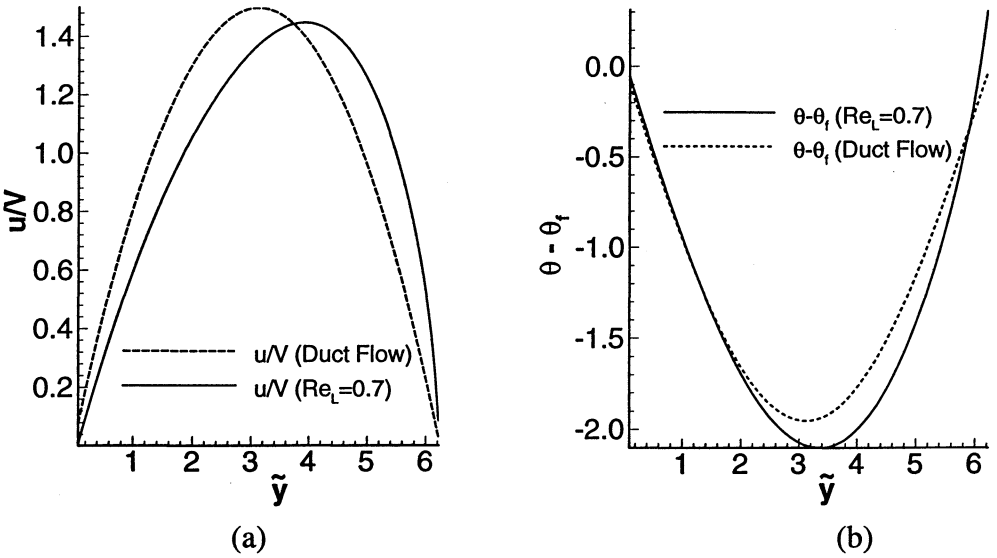

Figure 6.8 Comparison of velocity and temperature difference profiles between flow at $Re_L = 0.7$ and the fully developed duct flow with a duct spacing of $6.25H^*$; (a) normalized velocity, u/V, profiles; (b) temperature difference, $\theta - \theta_f$, profiles.

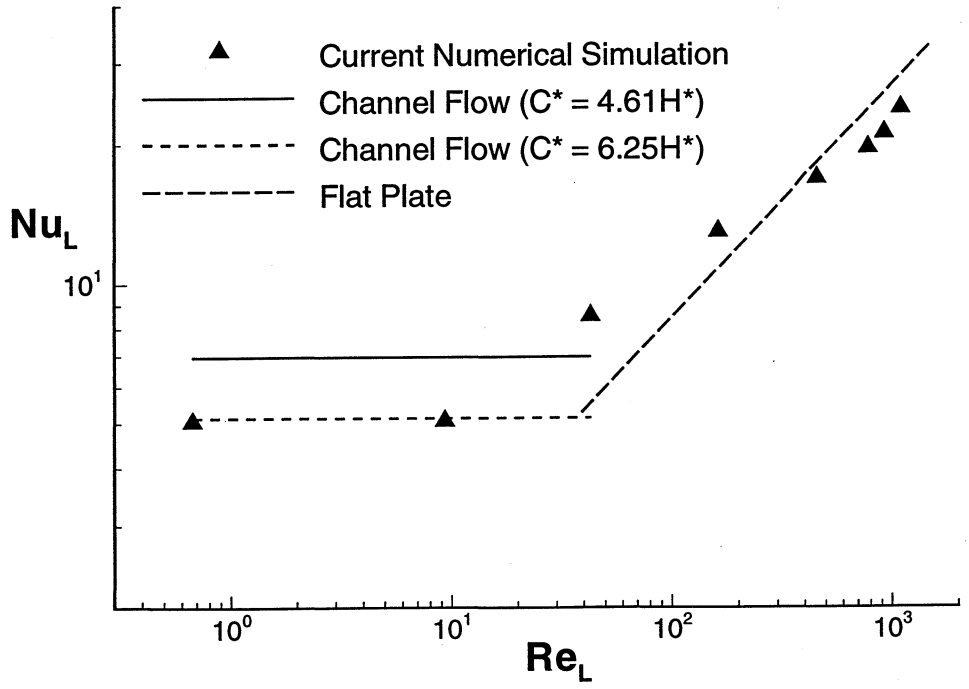

Figure 6.9 Comparison of currently calculated Nusselt numbers with solutions of duct flows and flow over a flat plate.

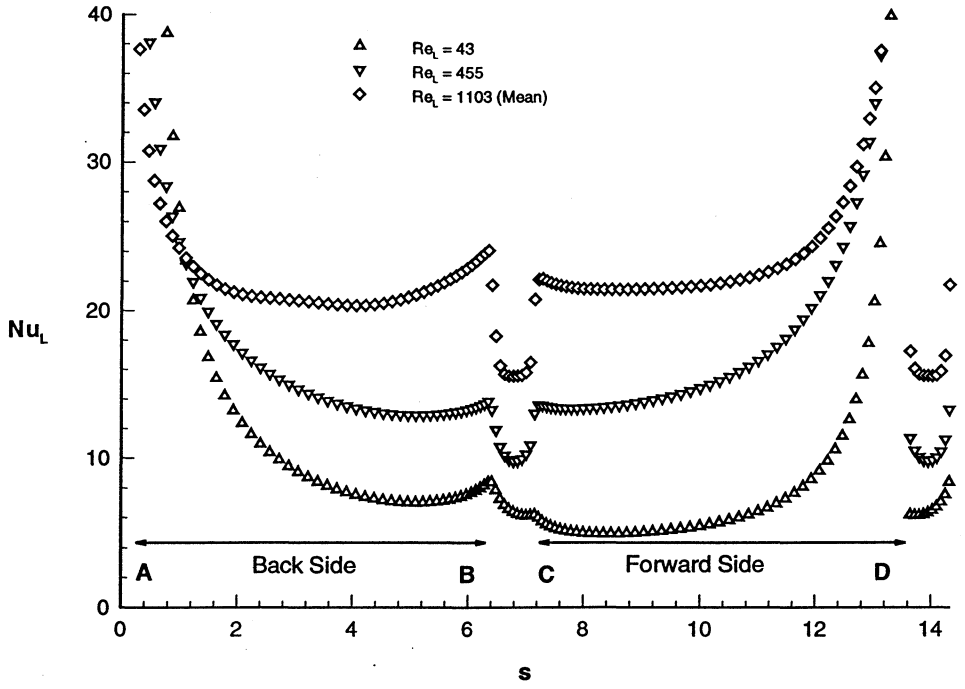

Figure 6.10 Local Nusselt number distribution along fin surface at different Reynolds numbers.

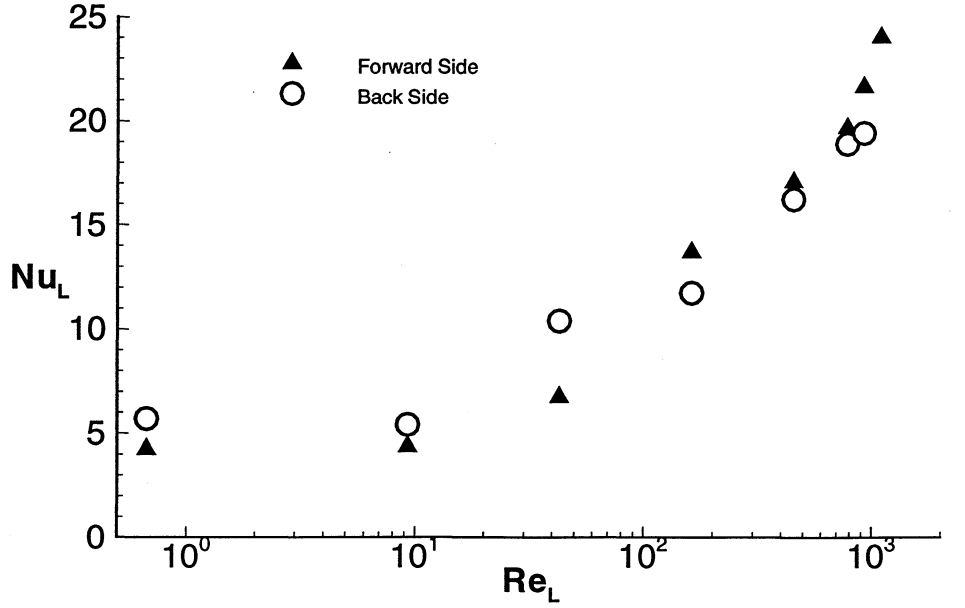

Figure 6.11 Comparison of Nusselt numbers at the forward and back sides of the fin.

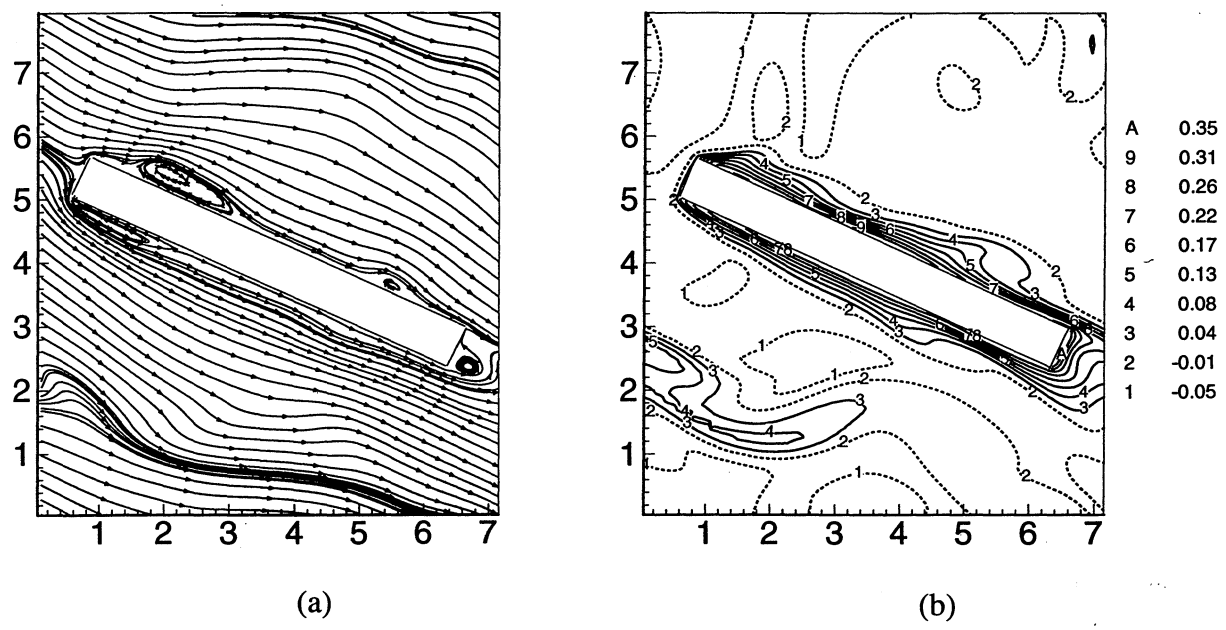

Figure 6.12 Instantaneous unsteady flow at Re_L = *1103*: (a) streamlines; (b) temperature contours.

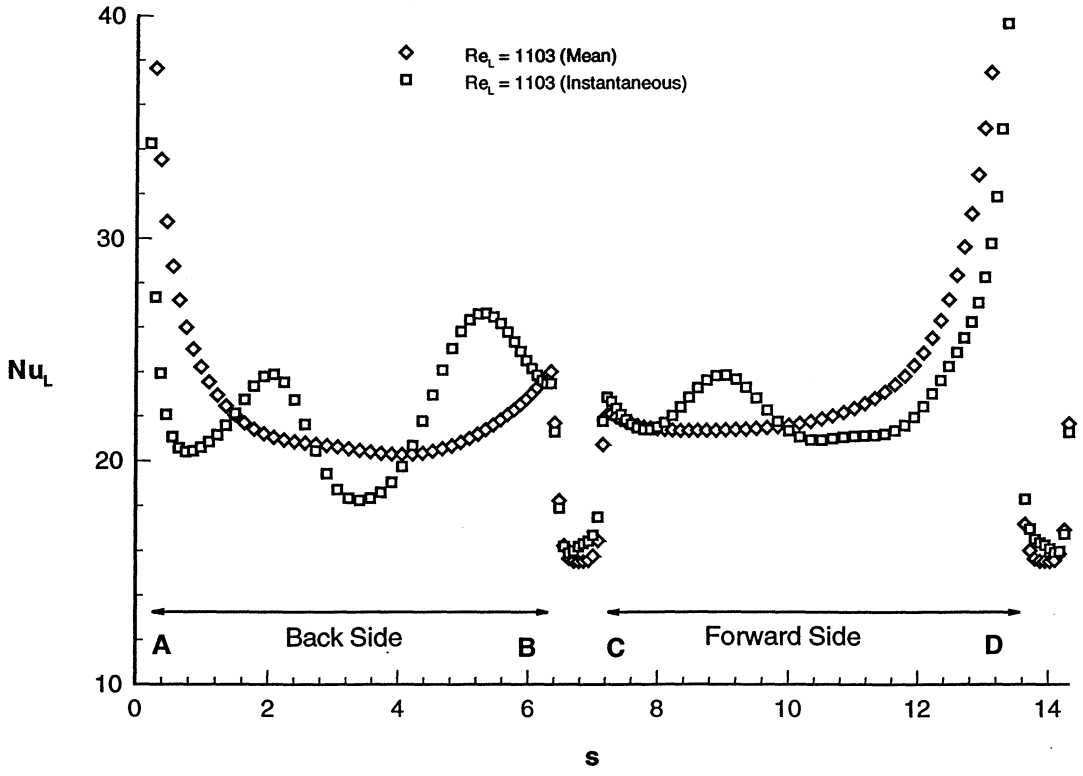

Figure 6.13 Effect of flow unsteadiness on local heat transfer in louvered fin simulation.

7. CONCLUSIONS AND RECOMMENDATIONS

Here direct simulations have been employed to explore the fluid flow and heat transfer in parallel-plate and louvered fin heat exchangers in the time-dependent flow regime and this approach has proven to be a very powerful tool in understanding the associated rich physics. The effects of vortex shedding and flow unsteadiness have been captured by solving the unsteady Navier-Stokes and energy equations. The flow field is assumed to be periodic along the streamwise and transverse directions in order to simulate flow over a large array of identical fin elements. The constant heat flux boundary condition employed in the present simulation allows for the definition of a modified temperature field which admits periodic boundary conditions.

Both the inline and staggered arrangements of parallel plate fins are considered and results obtained from these simulations are compared to those obtained from continuous parallel plates and the steady simulations of Sparrow and Liu (1979) on fins of infinitesimal thickness. The inline and staggered arrangements are seen to increase heat transfer and friction factor over the corresponding continuous parallel plate geometry, which maintains the same heat transfer surface area. The boundary layer restart and the geometry effects act in significantly different ways in the inline and staggered arrangements. In the case of the inline arrangement the transverse gap between adjacent fins available for through flow is more than halved. Thereby the velocity and temperature gradients are increased resulting in significant increase in the j factor and friction factor. But the velocity and temperature profiles approaching any fin element are not too far disturbed from the fully developed parabolic profile. In the case of the staggered arrangement, the transverse gap between adjacent fin elements decreases only slightly due to the finite thickness of the fin. On the other hand, owing to the staggered arrangement the velocity and temperature profiles approaching any fin element are significantly distorted away from the fully developed profile. The resulting increased velocity and thermal gradients at the fin surface contribute to increased j factor and friction factor. At higher Reynolds numbers, in both these arrangements the time-dependent flow modulation due to vortex shedding further significantly enhances heat transfer with an associated pumping power increase.

Irrespective of the fin arrangement, the flow is observed to follow a sequence of transitions. At very low Reynolds numbers the flow is steady and above a critical Reynolds number the flow becomes unsteady with a single dominant frequency. At even higher Reynolds numbers an additional lower frequency is generated and with subsequent increase in *Re* the flow becomes chaotic. In the inline arrangement these transitions are observed at a higher Reynolds number than in the staggered arrangement. In both arrangements the unsteady regime is marked by vortices that are generated at the leading edges of the fin element, which travel down on the top and bottom surfaces of the fin element. These vortices play a key role in significantly enhancing the local heat transfer by bringing cold fluid toward the fin surface. On the other hand, the reverse flow generated by the vortices near the fin surface is responsible for an overall reduction in skin friction on the fin surface.

The overall friction factor receives a contribution from the form drag due to the wake behind the trailing end of the fin element. It is observed that the flow unsteadiness manifests itself in the wake as waviness induced by vortex shedding and this significantly increases the form drag contribution. Since the increase in form drag is greater than the decrease in skin friction, the overall drag also increases due to the time-dependent flow motion. This raises an interesting possibility that if vortices that roll on the fin can be enhanced but the waviness in the wake can be suppressed, enhanced heat transfer may be achieved without pumping power penalty. It must be pointed out that the vortex shedding at the front leading edges and flow waviness in the wake are intimately related, with each influencing the other. This is a line of thought that is worth pursuing in order to improve the overall performance of the heat exchanger.

At higher Reynolds numbers, corresponding three-dimensional simulations at two different Reynolds numbers have been performed in the inline arrangement to investigate the effect of intrinsic three-dimensionality on heat transfer and frictional loss. It was discovered that the fluctuations in the *j* factor and friction factor are much higher in two-dimensional simulations than in corresponding three-dimensional simulations. It was observed that the amplitude of fluctuations of the friction factor in two-dimensional simulations could be as much as *5* times that in corresponding three-dimensional simulations, while the amplitude of fluctuations of the *j* factor in two-dimensional simulations could be as much as twice that in corresponding three-dimensional simulations. The difference in

amplitudes of fluctuations between two- and three-dimensional simulations increases as Reynolds number is increased. Since a lot of devices are designed according to maximum loads, overestimation of the maximum loads introduces additional material cost and also reduces efficiency, while underestimation of the maximum loads poses danger of the device failing. Therefore, accurate prediction of the level of fluctuations at high Reynolds numbers becomes important in heat exchanger design. Furthermore, it was observed that the two-dimensional simulations consistently overpredict not only the rms fluctuation but also the mean j factor. The flow characteristics in two-dimensional simulations are significantly different from those in the corresponding three-dimensional simulations and result in significant overprediction of the form drag. But simultaneous underprediction of skin friction in two-dimensional simulations results in negligible difference in overall friction factor due to the counter-balance between the these two components. This trend seems to be contradictory to the Reynolds analogy; however, a closer examination of the flow shows that the spanwise vortices are coherent in two-dimensional simulations and the presence of streamwise vortices in the corresponding three-dimensional simulations has disturbed the coherence of the spanwise vortices and contributed to the difference. This implies that the coherent spanwise vortices present in the two-dimensional simulations have the merit of enhancing overall heat transfer significantly while maintaining the associated frictional loss penalty nearly the same. Such data can be of great value in optimizing heat exchanger design. For example, transition to three-dimensionality can be delayed to higher Reynolds numbers in order to maintain the two-dimensionality of the flow.

In louvered fin simulations, different flow regimes have been observed in the current simulations and the results are in general agreement with the flow visualizations. The simulations clearly exhibit the various transitions undergone by the flow as Reynolds number is increased. The associated local heat transfer has been identified with the corresponding flow characteristics. The effect of flow unsteadiness at high Reynolds numbers has been captured in the current simulations, which is to increase the overall heat transfer.

The present simulations suffer from some limitations as well. Most importantly in the present simulations it has been assumed that the flow is periodic in the streamwise and transverse directions over a basic unit. This assumption precludes any possibility of streamwise and transverse subhar-

monic instabilities resulting in flow fields with periodicity over domains larger than a single basic unit. A preliminary study where the computational domain has been extended to twice the basic unit along the streamwise and transverse directions has shown that although small differences exist in the flow field, the effect on overall heat transfer and frictional loss is minimal. It is recommended that as part of a future study a systematic investigation on the effect of domain size be conducted.

Furthermore, the heat transfer enhancement mechanisms should be explored quantitatively in the louvered fin geometry, similar to the approach taken in the study of parallel-plate fins. Such an approach could isolate the individual mechanisms and make suggestions to improve louvered fin design. Finally, although the purpose of this study is not to obtain data correlation, future extension of the present work with a systematic variation of the parameters can provide the j factor and friction factor correlations.

REFERENCES

Achaichai, A. and Cowell, T. A., 1988, "Heat Transfer and Pressure Drop Characteristics of Flat Tube and Louvered Plate Fin Surfaces," *Experimental Thermal and Fluid Science*, Vol. 1, pp. 147-157.

Achaichia, A. and Cowell, T. A., 1988, "A Finite Difference Analysis of Fully Developed Periodic Laminar Flow in Inclined Louvered Arrays," *Proceedings of 2nd UK National Heat Transfer Conference*, Glasgow, Vol.2, pp. 883-888.

Amon, C. H. and Mikic, B. B., 1991, "Spectral Element Simulations of Unsteady Forced Convective Heat Transfer: Application to Compact Heat Exchanger Geometries," *Numerical Heat Transfer, Part A*, Vol. 19, pp. 1-19.

Aoki, H., Shinagawa, T. and Suga, K., 1989, "An Experimental Study of the Local Heat Transfer Characteristics in Automotive Louvered Fins," *Experimental Thermal and Fluid Science*, Vol. 2, pp. 293-300.

Beauvais, F. N., 1965, "An Aerodynamic Look at Automobile Radiators," *SAE Paper No.* 650470.

Chorin, A. J., 1968, "Numerical Solution of the Navier-Stokes Equations," *Mathematics of Computation*, Vol. 22, pp. 745-762.

Cowell, T. A., Heikal, M. R. and Achaichai, A., 1995, "Flow and Heat Transfer in Compact Louvered Fin Surfaces," *Experimental Thermal and Fluid Science*, Vol. 10, pp. 192-199.

Cur, N. and Sparrow, E. M., 1978, "Experiments on Heat Transfer and Pressure Drop for a Pair of Colinear, Interrupted Plates Aligned with the Flow," *International Journal of Heat and Mass Transfer*, Vol. 21, pp. 1069-1080.

Davis, R. W. and Moore, E. F., 1982, "A Numerical Study of Vortex Shedding from Rectangles," *Journal of Fluid Mechanics*, Vol. 116, pp. 475-506.

DeJong, N. C., 1996, "An Experimental Study of Flow and Heat Transfer in Offset Strip and Louvered-Fin Heat Exchangers," *M.S. Thesis*, University of Illinois at Urbana-Champaign, Urbana, Illinois.

DeJong, N. C. and Jacobi, A. M., 1996, "An Experimental Study of Flow and Heat Transfer in Parallel-Plate Arrays: Local, Row-by-Row, and Surface Average Behavior," *International Journal of Heat and Mass Transfer*, (in press).

Ghaddar, N. K., Karniadakis, G. E. and Patera, A. T., 1986, "A Conservative Isoparametric Spectral Element Method for Forced Convection; Application to Fully Developed Flow in Periodic Geometries," *Numerical Heat Transfer*, Vol. 9, pp. 277-300.

Gresho, P. M. and Sani, R. L., 1987, "On Pressure Boundary Conditions for the Incompressible Navier-Stokes Equations," *International Journal for Numerical Methods in Fluids*, Vol. 7, pp. 1111-1145.

Harlow, F. H. and Welch, J. E., 1965, "Numerical Calculation of Time-Dependent Viscous Incompressible Flow of Fluid with Free Surface," *Physics of Fluids*, Vol. 8(12), pp. 2181-2189.

Henderson, R. D., 1994, "Unstructured Spectral Element Methods: Parallel Algorithms and Simulations," *Ph.D. Thesis*, Princeton University, Princeton, New Jersey.

Hestenes, M. and Stiefel, E., 1952, "Methods of Conjugate Gradients for Solving Linear Systems," *Journal of Research of the National Bureau of Standards*, Vol. 49, pp. 409-436.

Hiramatsu, M. Ishimaru, T. and Matsuzaki, K., 1990, "Research on Fins for Air Conditioning Heat Exchangers," *JSME International Journal*, Vol. 33, pp. 749-756.

Howard, P., 1987, "An Analytical Model for Heat Transfer and Friction Characteristics of a Multi-Louvered Fin Heat Exchanger," *Masters Paper*, The Pennsylvania State University.

Huang, H. and Tao, W., 1993, "An Experimental Study on Heat/Mass Transfer and Pressure Drop Characteristics for Arrays of Nonuniform Plate Length Positioned Obliquely to the Flow Direction," *Journal of Heat Transfer*, Vol. 115, pp. 568-575.

Jacobi, A. M. and Shah, R. K., 1995, "Heat Transfer Surface Enhancement Through the Use of Longitudinal Vortices: A Review of Recent Progress," *Experimental Thermal and Fluid Science*, Vol. 11, pp. 295-309.

Joshi, H. M. and Webb, R. L., 1987, "Heat Transfer and Friction in the Offset Strip-Fin Heat Exchanger," *International Journal of Heat and Mass Transfer*, Vol. 30, pp. 69-83.

Kays, W. M., and London, A. L., 1984, *Compact Heat Exchangers*, McGraw-Hill, New York.

Kim, J. and Moin, P., 1985, "Application of a Fractional–Step Method to Incompressible Navier–Stokes Equations," *Journal of Computational Physics*, Vol. 59, pp. 308-323.

Lee, Y. N., 1986, "Heat Transfer and Pressure Drop Characteristics of an Array of Plates Aligned at Angles to the Flow in a Rectangular Duct," *International Journal of Heat and Mass Transfer*, Vol. 29, pp. 1553-1562.

London, A. L. and Shah, R. K., 1968, "Offset Rectangular Plate-Fin Surfaces - Heat Transfer and Flow Friction Characteristics," *Journal of Engineering for Gas Turbines and Power*, Vol. 90, pp. 218-228.

Manglik, R. M. and Bergles, A. E., 1990, "The Thermal-Hydraulic Design of the Rectangular Offset-Strip-Fin Compact Heat Exchanger," *Compact Heat Exchangers*, ed. Shah, R. K., Kraus, A. D., and Metzger, D., Hemisphere Publishing Corporation, pp. 123-149.

Mansy, H., Yang, P.-M. and Williams, D. R., 1994, "Quantitative Measurements of Three-Dimensional Structures in the Wake a Circular Cylinder," *Journal of Fluid Mechanics*, Vol. 270, pp. 277-296.

Mittal, R. and Balachandar, S., 1995, "Effect of Three-Dimensionality on the Lift and Drag of Circular and Elliptic Cylinders", *Physics of Fluids*, Vol. 7, pp. 1841-1865.

Mullisen, R. S. and Loehrke, R. I., 1986, "A Study of the Flow Mechanisms Responsible for Heat Transfer Enhancement in Interrupted-Plate Heat Exchangers," *Journal of Heat Transfer*, Vol. 108, pp. 377-385.

Pang, K, Tao, W. Q. and Zhang, H. H., 1990, "Numerical Analysis of Fully Developed Fluid Flow and Heat Transfer for Arrays in Interrupted Plates Positioned Convergently-Divergently Along the Flow Direction," *Numerical Heat Transfer, Part A*, Vol. 18, pp. 309-324.

Patankar, S. V., Liu, C. H. and Sparrow, E. M., 1977, "Fully Developed Flow and Heat Transfer in Ducts Having Streamwise-Periodic Variations of Cross-Sectional Area," *Journal of Heat Transfer*, Vol. 99, pp. 180-186.

Patankar, S. V. and Prakash, C., 1981, "An Analysis of the Effect of Plate Thickness on Laminar Flow and Heat Transfer in Interrupted-Plate Passages," *International Journal of Heat and Mass Transfer*, Vol., 24, pp. 51-58.

Roshko, A., 1993, "Perspectives on Bluff Body Aerodynamics," *Journal of Wind Engineering and Industrial Aerodynamics*, Vol. 49, pp. 79-100.

Sekulic, D. P., 1989, "Flow Through Communicating Channels Compact Heat Transfer Geometry," *International Communications in Heat and Mass Transfer*, Vol. 16, pp. 667-679.

Soria, J. and Cantwell, B. J., 1993, "Identification and Classification of Topological Structures in Free Shear Flows," *Eddy Structure Identification in Free Turbulent Shear Flows*, ed. Bonnet, J. P. and Clauser, M. N., pp. 379-390, Kluwer Academic Publishers, Netherlands.

Sparrow, E. M., Baliga, B. R. and Patankar, S. V., 1977, "Heat Transfer and Fluid Flow Analysis of interrupted-Wall Channels, with Applications to Heat Exchangers," *Journal of Heat Transfer*, Vol. 99, pp. 4-11.

Sparrow, E. M. and Hajiloo, A., 1980, "Measurements of Heat Transfer and Pressure Drop for an Array of Staggered Plates Aligned Parallel to an Air Flow," *Journal of Heat Transfer*, Vol. 102, pp. 426-432.

Sparrow, E. M. and Liu, C. H., 1979, "Heat Transfer, Pressure-Drop and Performance Relationships for Inline, Staggered, and Continuous Plate Heat Exchangers," *International Journal of Heat and Mass Transfer*, Vol. 22, pp. 1613-1624.

Suga, K. and Aoki, H., 1991, "Numerical Study on Heat Transfer and Pressure Drop in Multilouvered Fins," *ASME/JSME Thermal Engineering Proceedings*, Vol. 4, pp. 361-368.

Suga, K., Aoki, H. and Shinagawa, T., 1989, "Numerical Analysis on Two-Dimensional Flow and Heat Transfer of Louvered Fins Using Overlaid Grids," *JSME International Journal*, Vol. 33, pp. 122-127.

Suzuki, H., Suzuki, K. and Sato, T., 1988, "Dissimilarity Between Heat and Momentum Transfer in a Turbulent Boundary Layer Disturbed by a Cylinder," *International Journal of Heat and Mass Transfer*, Vol. 31, pp. 259-265.

Tafti, D. K. and Vanka, S. P., 1991, "A Numerical Study of Flow Separation and Reattachment on a Blunt Plate," *Physics of Fluids A*, Vol. 3(7), pp. 1749-1759.

Tafti, D. K. and Vanka, S. P., 1991, "A Three-Dimensional Numerical Study of Flow Separation and Reattachment on a Blunt Plate," *Physics of Fluids A*, Vol. 3(12), pp. 2887-2909.

Tafti, D. K., 1993, "A Study of High-Order Spatial Finite Difference Formulation for the Incompressible Navier-Stokes Equations," *NCSA Preprint*, **031**.

Tafti, D. K., 1993, "Vorticity Dynamics and Scalar Transport in Separated and Reattached Flow on a Blunt Plate," *Physics of Fluids A*, Vol. 5(7), pp. 1661-1673.

Tafti, D. K., 1994, "Features and Implementation Issues for a High-Order Finite Difference Algorithm for Direct and Large Eddy Simulations of Incompressible Turbulence on the CM-5," *NCSA Technical Report*, **047**.

Tafti, D. K., 1995, "High-Order Finite Difference Formulation for the Incompressible Navier-Stokes Equations on the CM-5," *Proceedings of the Seventh SIAM Conference on Parallel Processing for Scientific Computing,* ed. Bailey et al., pp. 155-160.

Tafti, D. K., 1995, "A Study of Krylov Methods for the Solution of the Pressure Poisson Equation on the CM-5," *Numerical Developments in CFD,* ed. Dhaubhadel, M. N. et al., FED-Vol. 215, pp. 1-8, ASME, New York.

Tafti, D. K., 1996, "Comparison of Some Upwind Biased High-Order Formulations with a Second-Order Central Difference Scheme for the Time Integration of the Incompressible Navier-Stokes Equations," *Computers and Fluids,* (accepted).

Tafti, D. K., 1996, personal communication.

Tamura, T., 1990, "Numerical Study of Aerodynamic Behavior of a Square Cylinder," *Journal of Wind Engineering and Industrial Aerodynamics*, Vol. 33, pp. 161-170.

Valencia, A., Fiebig, M. and Mitra, N. K., 1996, "Heat Transfer Enhancement by Longitudinal Vortices in a Fin-Tube Heat Exchanger Element with Flat Tubes," *Journal of Heat Transfer*, Vol. 118, pp. 209-211.

Webb, R. L. and Trauger, P., 1991, "Flow Structure in the Louvered Fin Heat Exchanger Geometry," *Experimental Thermal and Fluid Science*, Vol. 4, pp. 205-217.

Wieting, A. R., 1975, "Empirical Correlations for Heat Transfer and Flow Friction Characteristics of Rectangular Offset-Plate-Fin Heat Exchangers," *Journal of Heat Transfer*, Vol. 97, pp. 488-490.

Williams, P. T. and Baker, A. J., 1996, "Incompressible Computational Fluid Dynamics and the Continuity Constraint Method for the Three-Dimensional Navier-Stokes Equations," *Numerical Heat Transfer, Part B*, Vol. 29(2), pp. 137-273.

Williamson, C. H. K., 1988, "The Existence of Two Stages in the Transition to Three-Dimensionality of a Cylinder Wake," *Physics of Fluids*, Vol. 31, pp. 3165-3168.

Williamson, C. H. K., 1989, "Oblique and Parallel Modes of Vortex Shedding in the Wake of a Circular Cylinder at Low Reynolds Numbers," *Journal of Fluid Mechanics*, Vol. 206, pp. 579-627.

Wu, J., Sheridan, J., Soria, J. and Welsh, M. C., 1994, "An Experimental Investigation of the Streamwise Vortices in the Wake of a Bluff Body," *Journal of Fluids Structures*, Vol. 8, pp. 621-635.

Xi, G., Futagami, S., Hagiwara, Y. and Suzuki, K., 1991, "Flow and Heat Transfer Characteristics of Offset-Fin Array in the Middle Reynolds Number Range," *ASME/JSME Thermal Engineering Proceedings*, Vol. 3, pp. 151-156.

Zhang, H. and Lang, X., 1989, "The Experimental Investigation of Oblique Angles and Interrupted Plate Lengths for Louvered Fins in Compact Heat Exchangers," *Experimental Thermal and Fluid Science*, Vol. 2, pp. 100-106.

Zhang, H.-Q., Fey, U., Noack, B. R., Honig, M. and Eckelmann, H., 1994, "On the Transition of the Cylinder Wake," *Physics of Fluids*, Vol. 7(4), pp. 779-794.

Zhang, L. W., Balachandar, S., Najjar, F. M. and Tafti, D. K., 1995, "A Numerical Study of Heat Transfer Enhancement Mechanisms in Parallel-Plate Fin Heat Exchangers," *Proceedings of International Conference on Advances in Mechanical Engineering* (*ICAME*), pp. 1605-1617.

Zhang, L. W., Tafti, D. K., Najjar, F. M. and Balachandar, S., 1996, "Computations of Flow and Heat Transfer in Parallel-Plate Fin Heat Exchangers on the CM-5; Effects of Flow Unsteadiness and Three-Dimensionality," *International Journal of Heat Mass Transfer,* (in press).

Zhang, L. W., Balachandar, S., Tafti, D. K. and Najjar, F. M., 1996, "Heat Transfer Enhancement Mechanisms in Inline and Staggered Parallel-Plate Fin Heat Exchangers," *International Journal of Heat Mass Transfer,* (in review).

Zhou, J., Adrian, R. J. and Balachandar, S., 1996, "Autogeneration of Near-Wall Vortical Structures in Channel Flow," *Physics of Fluids*, Vol. 8(1), pp. 288-290.